STUDY ON EQUAL CHANNEL ANGULAR EXTRUSION OF CIRCULAR CROSS SECTION COMPONENTS AND ITS APPLICATION FOR JOINING DISSIMILAR METALS

DAVOUD MASHHADI JAFARLOU

FACULTY OF ENGINEERING
UNIVERSITY OF MALAYA
KUALA LUMPUR

2016

STUDY ON EQUAL CHANNEL ANGULAR EXTRUSION OF CIRCULAR CROSS SECTION COMPONENTS AND ITS APPLICATION FOR JOINING DISSIMILAR METALS

DAVOUD MASHHADI JAFARLOU

THESIS SUBMITTED IN FULFILMENTOF THE REQUIREMENTS FOR THE DEGREE OF DOCTOR OF PHILOSOPHY

FACULTY OF ENGINEERING
UNIVERSITY OF MALAYA
KUALA LUMPUR

2016

UNIVERSITY OF MALAYA

ORIGINAL LITERARY WORK DECLARATION

Name of Candidate: **Davoud Mashhadi Jafarlou**

Matric No: **KHA130066**

Name of Degree: **Doctor of Philosophy (PhD)**

Title of Thesis: **Study on equal channel angular extrusion of circular cross section components and its application for joining dissimilar metals**

Field of Study: **Engineering Design**

I do solemnly and sincerely declare that:

(1) I am the sole author/writer of this Work;
(2) This Work is original;
(3) Any use of any work in which copyright exists was done by way of fair dealing and for permitted purposes and any excerpt or extract from, or reference to or reproduction of any copyright work has been disclosed expressly and sufficiently and the title of the Work and its authorship have been acknowledged in this Work;
(4) I do not have any actual knowledge nor do I ought reasonably to know that the making of this work constitutes an infringement of any copyright work;
(5) I hereby assign all and every rights in the copyright to this Work to the University of Malaya ("UM"), who henceforth shall be owner of the copyright in this Work and that any reproduction or use in any form or by any means whatsoever is prohibited without the written consent of UM having been first had and obtained;
(6) I am fully aware that if in the course of making this Work I have infringed any copyright whether intentionally or otherwise, I may be subject to legal action or any other action as may be determined by UM.

Candidate's Signature Date:

Subscribed and solemnly declared before,

Witness's Signature Date:

Name:

Designation:

ABSTRACT

In the last two decades, significant focus has been directed toward severe plastic deformation (SPD) as a direct method to produce bulk metals with superior mechanical properties. Numerous researches have been conducted in order to develop SPD methods for grain refinement of metallic structure with various geometrical shapes and chemical compositions. Among these methods, equal channel angular extrusion (ECAE) is the most developed SPD technique due to its capability of processing structural components. The mechanical properties of wide range of pure metals and alloys have been investigated in different research works; however there is a lack of study on mechanical properties of AA 6063 processed by ECAE. Moreover the ECAE technique is used mostly for grain refinement of components with circular (rod) or rectangular (beam) cross sections and there is no robust study on developing this technique for the processing of tubular components. Therefore, the current study focused on developing ECAE for processing tubular components. Additionally, in this research a developed method for solid state joining of dissimilar metals was proposed.

In the first phase of this study, the mechanical properties of ECAE treated AA 6063 were investigated. Following the ECAE process, samples were subjected to heat treatment (HT), hard anodizing (HA), and a combination of HT and HA. From the experimental fatigue and fretting fatigue tests, it was apparent that the ECAE treatment improves fatigue and fretting fatigue lives of the samples at low and high-cyclic loads and post ECAE heat treatment (ECAE+HT) more effectively improves the fatigue endurance. HA of AA6063 increased the fatigue and fretting fatigue lives of ECAE + HT-processed samples at low cycle; however, at high cycle, HA had reverse effects, whereby the fatigue and fretting fatigue lives of ECAE + HT-processed samples reduced.

In the second part of this research ECAE was utilized to produce metal tubes with ultrafine grain (UFG) structures. To mitigate plastic instability effects such as tube buckling and fracture during processing, hydraulic oil was used to fill the tube cavity. Finite element analysis (FEA) was carried out to examine the feasibility of the proposed method and deformation mechanism during ECAE. Experimental test results indicated that the resultant 60% reduction in grain size led to significant mechanical properties improvements including yield shear strength, ultimate shear strength, and microhardness.

In the third phase ECAE was applied for the solid state joining of tubular AA 6061 components and SAE 1018 steel rods. The influence of using a 0.1 mm thick 60Ag-30Cu-10Sn interlayer in addition to annealing at 220, 320, 420 and 520 °C for 60 min was investigated as well. FEA was performed in order to evaluate the deformation behavior of the workpieces during the ECAE joining process. The FEA outcome showed remarkable accumulation of equivalent plastic strain with relatively low strain inhomogeneity. Experimental results revealed that by increasing annealing temperature and using interlayer, the joint strength was improved. According to the results, shear strength of up to 32 MPa is feasible by having an interlayer and with subsequent annealing at 520 °C.

ABSTRAK

Dalam tempoh dua dekad yang lalu, tumpuan ketara telah diarahkan ke arah ubah bentuk plastik yang teruk (SPD) sebagai kaedah langsung untuk menghasilkan logam pukal dengan sifat-sifat mekanik yang unggul. Banyak kajian telah dijalankan untuk membangunkan kaedah SPD untuk penghalusan bijian struktur logam dengan pelbagai bentuk geometri dan komposisi kimia. Di antara kaedah-kaedah ini, penyemperitan sudut saluran yang sama (ECAE) adalah teknik SPD yang paling maju disebabkan oleh keupayaan pemprosesan komponen struktur. Sifat-sifat mekanik Pelbagai logam tulen dan aloi telah disiasat kerja penyelidikan yang berbeza; namun ada kekurangan kajian mengenai sifat-sifat mekanik AA 6063 diproses oleh ECAE. Lebih-lebih lagi teknik ECAE digunakan kebanyakannya untuk penghalusan bijian komponen dengan bulat (rod) atau segi empat tepat (rasuk) keratan rentas dan tidak ada kajian yang kukuh kepada pembangunan teknik ini untuk memproses komponen tiub. Oleh itu, kajian semasa memberi tumpuan kepada membangunkan ECAE untuk memproses komponen tiub. Selain itu dalam kajian ini satu kaedah yang dibangunkan untuk keadaan pepejal penyambungan logam yang berbeza telah dicadangkan.

Dalam fasa pertama kajian ini, sifat-sifat mekanik ECAE dirawat AA 6063 telah disiasat. Berikutan proses ECAE, sampel juga telah tertakluk kepada rawatan haba (HT), fosforik keras (HA), dan gabungan HT dan HA. Keletihan eksperimen dan ujian keletihan retak, ia adalah jelas bahawa rawatan ECAE bertambah baik keletihan dan retak kehidupan keletihan sampel pada beban rendah dan tinggi berkitar dan rawatan haba selepas ECAE (ECAE + HT) lebih berkesan meningkatkan ketahanan lesu. HA daripada AA6063 meningkat keletihan dan keletihan retak kehidupan sampel ECAE + HT-diproses pada kitaran yang rendah; Walau bagaimanapun, pada kitaran yang tinggi, HA mempunyai kesan terbalik, di mana keletihan dan retak kehidupan keletihan sampel ECAE + HT-diproses dikurangkan.

Dalam bahagian kedua kajian ini ECAE telah digunakan untuk menghasilkan tiub logam dengan ultrafine bijirin (UFG) struktur. Bagi mengurangkan kesan ketidakstabilan plastik seperti tiub lengkokan dan patah semasa pemprosesan, minyak hidraulik telah digunakan untuk mengisi rongga tiub. Analisis unsur terhingga (FEA) telah dijalankan untuk mengkaji kemungkinan mekanisme kaedah dan ubah bentuk yang dicadangkan semasa ECAE. Keputusan ujian eksperimen menunjukkan bahawa pengurangan 60% yang dihasilkan dalam saiz butiran membawa kepada peningkatan mekanikal harta ketara termasuk kekuatan alah ricih, kekuatan ricih muktamad, dan microhardness.

Dalam fasa ketiga ECAE dipohon keadaan pepejal penggabungan tiub AA 6061 komponen dan SAE 1018 rod keluli. Pengaruh menggunakan 0.1 mm tebal 60Ag-30Cu-10Sn interlayer di samping penyepuhlindapan pada 220, 320, 420 dan 520 °C selama 60 minit telah disiasat juga. FEA telah dilakukan untuk menilai tingkah laku ubah bentuk bahan kerja semasa proses menyertai ECAE. Hasil FEA menunjukkan pengumpulan luar biasa terikan plastik bersamaan dengan ketakhomogenan tekanan rendah. Keputusan eksperimen menunjukkan bahawa dengan meningkatkan suhu penyepuhlindapan dan menggunakan interlayer, kekuatan bersama telah bertambah baik. Menurut hasil, kekuatan ricih sehingga 32 MPa boleh dilaksanakan dengan mempunyai interlayer dan dengan penyepuhlindapan berikutnya pada 520 °C.

ACKNOWLEDGMENT

Though only my name appears on the cover of this dissertation, a great many people have contributed to its production. I owe my gratitude to all those people who have made this dissertation possible and because of whom my graduate experience has been one that I will cherish forever.

I would like to thank my supervisors Professor Mohsen Abdel Naeim Hassan Mohammad and Dr. Noor Azizi Bin Mardi for their invaluable assistance in planning and executing this work, and for their patient advice and support through all my research.

I wish to thank my parents, without whom I would never have been able to acquire this degree. Their support and inspiration during my educations provided the foundation for this work. Finally, my heartfelt thanks go to my brothers for their encouragement during the last few years.

TABLE OF CONTENTS

LIST OF FIGURES

LIST OF TABLES

LIST OF SYMBOLS AND ABBREVIATION

AA	Aluminum alloy
ARB	Accumulative Roll Bonding
C	Heat capacity
C2C2	Continuous Confined Strip Shearing
C_i	Inhomogeneity index
CRSS	critical resolved shear stress
d	Grain size
E	Young modulus
ECAD	Equal Channel Angular Drawing
ECAE	Equal Channel Angular Extrusion
ED	Extrusion Direction
EPS	Equivalent Plastic Strain
FE	Finite Element
FEA	Finite Element Analysis
HV	Vickers hardness
HA	Hard Anodizing
HCF	High Cycle Fatigue
HT	Heat Treatment
HPT	High-Pressure Torsion
HPTT	High-Pressure Torsion Tube Pressing
LCF	Low Cycle Fatigue
m	Friction factor
ND	Normal Direction
PEEQ	Equivalent plastic strain

SPD	Severe Plastic Deformation
T	Temperature
T_{ECAE}	Melting temperature
T_{melt}	ECAE temperature
TCEC	Tube Cyclic Extrusion Compression
TCP	Tube Channel Pressing
TD	Transverse Direction
TMT	Thermo-mechanical Treatment
Δt	Dwell time
t	Tangential vector
ΔT	Temperature rise
u	Velocity vector
UFG	Ultra Fine Grain
V	Volume
w	Ideal work
φ	Channel angle
ψ	Corner angle
ρ	Density
δ	Displacement
$\bar{\sigma}$	Equivalent stress
ε_f	Fracture strain
μ	Friction coefficient
f_F	Friction force
σ_F	Friction stress
f_N	Normal force
σ_N	Normal stress

σ_0	Peierls stress
υ	Poisson ration
σ_1	Principle stress in x direction
σ_2	Principle stress in y direction
σ_3	Principle stress in z direction
v_r	Relative velocity
γ	Shear strain
τ	Shear stress
η	Stress triaxiality
ε	True strain
σ_{UTS}	Ultimate strength
σ_y	Yield stress

CHAPTER ONE: INTRODUCTION

1.1. Background

Metal forming processes have played a central role as societies developed. The production of metallic components with high strength in the metal forming industry is gaining importance due to the trend to increase products reliability and life expectancy (Hause & Maltby, 1998). Over the years, the field of metal strengthening technology has been radically changed by a number of innovations which is summarized in Table 1.1.

Table 1.1: Various strengthening methods

Name	Characteristics	Ref.
Solid-solution hardening	Introduction of interstitial or substitutional atoms of different kind	(Suzuki et al., 2013)
Precipitation hardening	Distribution of fine precipitates	(Mott & Nabarro, 1940)
Dispersion hardening	Distribution of 2nd phase particles	(Smallman, 2013)
Work hardening	Increase in dislocation density by plastic deformation	(Banabic, 2000)
Grain size reduction	Reducing grain size	(Gleiter, 1989)
Composites	Mixing different materials	(Daniel et al., 1994)

All strengthening methods mentioned in Table 1.1 are based on the restricting of the dislocation movement except for the composite method which relays on the mixing of different materials. Grain size reduction is one of the most promising techniques for strengthening polycrystalline materials. In this regard several methods have been introduced which is categorized as powder processing methods and heavy plastic deformation methods (Mehrer, 2007).

The production of ultra-fine grain (UFG) materials using powder methods are carried out using techniques such as inert-gas condensation, high-energy milling and cryogenic ball-milling. These techniques allow for wide range of versatility for example nanostructure composite materials can be produced by these techniques. However these techniques require pre-generated small crystalline structure. Moreover residual porosity and impurity in compact powder can be potentially produced by powder techniques. There are, however, also procedures like severe plastic deformation (SPD), which do not require pre-generated clusters (Gleiter, 1989; Mehrer, 2007).

During the last two decades, significant focus has been directed toward SPD as direct methods to produce bulk metals with enhanced mechanical properties by producing ultrafine grain (UFG) structures. The principal SPD mechanism is to impose an ultra large plastic strain through the application of extremely high pressures at relatively low operating temperatures (Valiev et al., 2015). In this way, fractures originating from large shear plastic strain are avoided, since the shape of the bulk material remains unchanged after deformation and stress triaxiality does not exceed the effective plastic strain. The ultra-large plastic strain introduced to the bulk metal during SPD is able to refine coarse grains (CG) and constitute ultrafine microstructures with grain sizes in the range of 100 nm to 1μm (Valiev et al., 2006).

The ultrafine grain metals yielded by SPD cannot be reproduced via conventional thermo-mechanical treatment (TMT) methods. As a result, SPD-processed metals exhibit a suitable combination of mechanical properties compared to metals with refined grain structures produced through conventional TMT processes (Azushima et al., 2008).

Moreover, SPD processes are able to alleviate residual porosity and contamination defects in the final product which are frequently observed with powder based methods.

Additionally, SPD techniques have great potential to be implemented in the mass production of UFG metallic materials (Valiev, 2004).

Various SPD processes including equal channel angular extrusion (ECAE) also referred to as equal channel angular pressing (ECAP), accumulative roll bonding (ARB), high pressure torsion (HPT), multi axial forging and twist extrusion have been developed to fabricate UFG metals, which were reviewed in detail by (Estrin & Vinogradov, 2013). Among the various SPD techniques for bulk material processing, ECAE has attracted particular attention due to its exceptional scaling potential for various industrial applications, including its ability to apply the highest plastic strain (Segal, 1999).

1.2. Problem statement

The inevitable need to introduce new processing methods for enhancing current lightweight materials mechanical properties is essential due to the current climate change scenario (Hirsch & Al-Samman, 2013). High strength steels have been amongst the most promising materials for structural components. However, their relatively high density has urged industries to solve this issue by utilizing a variety of lightweight materials including titanium, magnesium, and aluminum alloys as substitutes for steels. Amongst them, aluminum alloys have attracted exceptional attention due to their high strength-to-weight ratio and excellent corrosion resistance and significantly lower price. However, the sole usage of aluminum alloys in mass production is not cost effective due to the relatively lower strength which should be modified via adding costly alloying elements to composition or applying energy consuming heat treatments (Taban et al., 2010).

In this regard, necessity for proposing new methods to enhance mechanical properties including yield stress, tensile strength and ductility besides fatigue endurance is indispensable. Non-age-hardenable aluminum alloys including AA 5xxx series are not

responsive to the SPD process in the term of fatigue life enhancement. On the other hand, grain refinement, tensile strength, ductility, and surface hardness enhancement, and also improvement of fatigue life for age-hardenable aluminum alloys such as AA 6xxx series are efficiently obtained by the SPD process. However, mechanical properties of ECAE-treated AA 6063 have not been vastly investigated. Specially, there is not robust study regarding fatigue and fretting fatigue life of this grade of aluminum alloy under rotating-bending cyclic loading.

Furthermore, tubular AA 6061 components are widely used in many branches of engineering such as aircraft, automotive, cooling towers, pressure vessels, pipelines and offshore platforms. Hence, production of tubular components with promising mechanical properties remains a primary driver in material science. With this regard, a variety of SPD processes, such as tubular channel angular pressing (TCAP) (Faraji et al., 2011), tube channel pressing (TCP) (Farshidi et al., 2014), high-pressure tube twisting (HPTT) (Tóth et al., 2009), tube cyclic extrusion compression (TCEC) (Babaei & Mashhadi, 2014), and stagger spinning (Xia et al., 2014) have been developed to produce UFG structures with tubular geometries. Tubular materials with UFG structures can be successfully produced via these methods; however, limitations such as low production rates, material inhomogeneity, short lengths of the final product, and SPD process complexity have restricted their widespread applicability for mass production.

Moreover, considering the need for components with high strength, low weight and reasonable price, combining steels and aluminum alloys through dissimilar material joining methods seems an ideal solution. Due to outstanding applicability, the dissimilar joining of steels and aluminum alloys has undergone extensive research in order to find which joining techniques offer desirable quality while decreasing the final cost and amount of labor. Depending on the operating temperature, applied pressure and state of materials during joining, steel-to-aluminum joining techniques fall into three categories:

fusion joining, solid-state joining and mechanical fastening. Amongst the solid-state methods, joining by plastic deformation is a promising technique of joining dissimilar materials with sufficient ductility, such as steel and aluminum alloy owing to minimal thermal effects as well as reduced residual stress (Mori et al., 2013). Despite the advantages furnished by plastic joining, joining through SPD provides the extra benefit of producing metallic components with superior mechanical properties, which has not been extensively studied.

1.3. Objectives

The primary aim of the research presented in this thesis was the fundamental investigations on processing component with circular cross section through ECAE with major focus on processing tubular components. Additionally, novel technique was developed for joining dissimilar cylindrical and bar-shaped components via ECAE. Hence, the objectives of this research are:

- To evaluate the influences of ECAE on the mechanical properties of AA 6063 as well as plain fatigue and fretting fatigue lives under cyclic rotating-bending load.
- To analyze the influence of T4 heat treatment and hard anodizing on mechanical properties as well as fatigue and fretting fatigue lives of ECAE-treated AA 6063.
- To analyze the effects of ECAE, with and without T6 heat treatment, for SPD of tubular components on its mechanical properties and microstructure evaluation.
- To develop a novel process for plastic joining of dissimilar metals including tubular AA 6061 and cylindrical mild steel SAE 1018 using ECAE.
- To determine the influence of a 60Ag-30Cu-10Sn interlayer in addition to a post-ECAE annealing process on joint quality of tubular AA 6061 and cylindrical mild steel SAE 1018 processed by ECAE.

1.4. Scope of the thesis

To date, the ECAE process is studied in order to analyze mechanical properties and microstructure evolution of different materials which generally are rod or beam shape; however, few researches has been conducted in order to evaluate fatigue and fretting fatigue endurance of AA 6063, additionally slight attention has been paid to study the capability of this process for processing tubular components using ECAE. Furthermore, the ability of this process for joining dissimilar materials has not been investigated. Therefore, the scope of this thesis defines as follow:

i. Evaluation of fatigue and fretting fatigue behavior of AA 6063.
ii. Development of ECAE for SPD treatment of tubular AA 6061.
iii. Development of ECAE for plastic joining of dissimilar materials including AA 6061 and mild steel SAE1018.

1.5. Thesis outline

The remainder of the thesis is organized into five chapters. Following this introductory chapter, chapter two gives a critical review of relevant literature, from overview of ECAE fundamental, major ECAE process parameters, FE-analysis of ECAE and mechanical properties of lightweight materials processed through ECAE.

Chapter three outlines the newly designed approaches regarding ECAE treatment of tubular components as well as joining dissimilar materials using ECAE. Furthermore, methods employed for the material characterization of ECAE treated components is explained in this chapter.

The FE-analyses are described in chapter four. The explicit dynamics approach provided by the commercial FE-code Abaqus 6.11 is used in this research. The 3D FE-models were generated according to mechanical and geometrical properties identical to those utilized during process design in order to precisely determine the deformation

behavior in the workpiece as well as to reduce the discrepancy between numerical and experimental results.

Chapter five presents the results obtained from FEA and experimental material characterization. In this chapter the feasibility of the proposed process for enhancing fatigue and fretting fatigue endurance of ECAE treated components, practicability of ECAE for treatment of tubular components as well as joinability between dissimilar materials using ECAE are provided. Finally, Chapter six describes and summarizes findings obtained in this research as well as suggestion for future works.

CHAPTER TWO: LITERATURE REVIEW

2.1. Introduction

The organization of this chapter is as follows. In section 2.2, metals strengthening mechanisms are discussed with emphasis on the influence of grain refinement on mechanical properties. The idea of severe plastic deformation (SPD) as the most effective grain refinement method is presented in section 2.3. Additionally, in this section the most promising SPD techniques are considered. In section 2.4, equal channel angular extrusion (ECAE), also referred to as equal channel angular pressing (ECAP), as the most successful SPD technique for processing bulk structural metallic materials is reviewed. Furthermore, newly developed extension of ECAE including ultrafine tube processing and importance of dissimilar metallic materials joining using plastic joining methods are introduced. In section 2.5, major ECAE parameters including die geometry, extrusion force, friction and strain rate is discussed in detail. Approaches which were introduced for numerical simulation of ECAE process is reviewed in section 2.5 and main emphasis is paid on finite element analysis (FEA) as the most efficient numerical method. In section 2.7, mechanical properties of ECAE-treated materials with focus on aluminum alloy including yield strength, ultimate strength, ductility and fatigue life are discussed. In the last section of this chapter research gap and aim of the present work are declared.

2.2. Metals strengthening mechanisms

The plastic deformation in metallic materials is addressed by the motion of large number of dislocations. Dislocations generally are categorized as the edge dislocation (extra half plane in lattice structure) and screw dislocation (sheared lattice). Also in many materials, line of dislocation neither parallel nor perpendicular to Burger vectors, which is introduced mixed dislocations. Furthermore it was found that in some crystals,

lattice vector can be larger than dislocation's Burger vector. Such a dislocation called partial dislocation (Suzuki et al., 2013).

There are two main mechanisms that lead to plastic deformation, namely glides of dislocation and mechanical twinning. Glide of dislocation is considered as the most important mechanism in which dislocations slip over each other along certain planes and direction of crystal lattice. Another plastic deformation mechanism is mechanical twinning, which take place by imposing sufficient shear stress to crystal lattice. As a result of this shear stress a part of the crystal lattice transformed to a twinned position (Banabic, 2000). Schematic of plastic deformation mechanisms are illustrated in Figure 2.1.

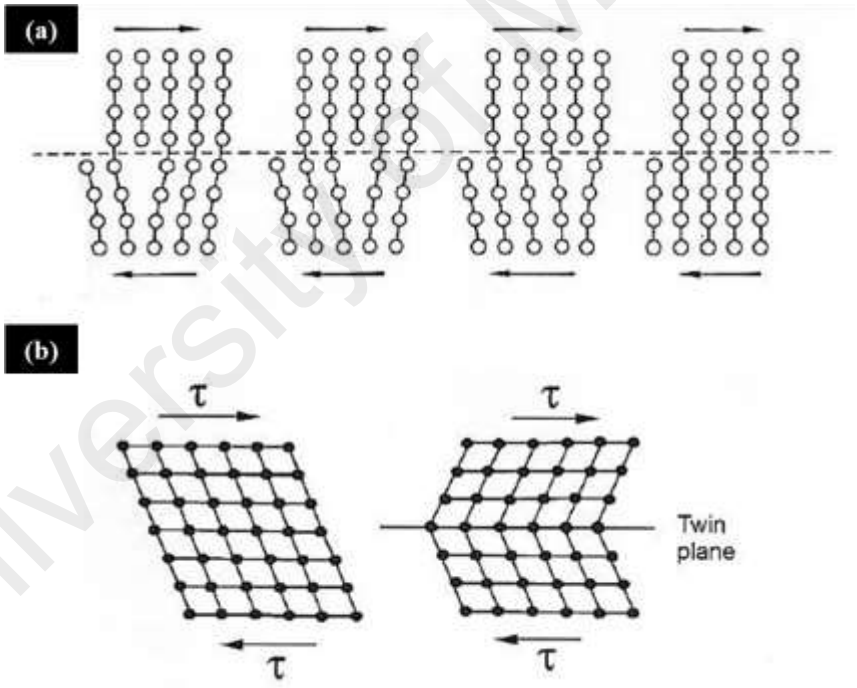

Figure 2.1: Schematic of plastic deformation by (a) slipping by movement of an edge dislocation and (b) mechanical twin formation (Banabic, 2000)

As a result of plastic deformation of crystal, a large number of dislocations are accumulated in crystal with non-uniform distribution. These dislocations localized in the form of a plane or a wall as a consequence of formation of multipoles and polygon walls. Therefore, grain interior is divided into smaller regions by diffuse boundaries with high density of dislocation. The strengthening mechanism relies on constraining

dislocation motion to render material harder and stronger using methods including, solid solution strengthening, precipitation hardening, dispersion hardening and grain size reduction (Suzuki et al., 2013).

The solid solution hardening performs a result of an interaction between the mobile dislocation and solute atoms which are accomplished based on dissolving one metal or several metals (solutes) into another (solvent). Therefore, this mechanism is done during metal casting, when all metals are in liquid form. Two types of solid solution namely; substitutional and interstitial solution have been introduced as two types of solid solution. In substitutional solution atoms of solute metal replace atoms of the solvent material in the crystal lattice. Since the solute and solvent atoms are of different sizes, they interrupt the regularity of the crystal lattice and subsequently hinder the motion of dislocation around this interruption. The second type of solid solution is called an interstitial solution. In this case, solute atoms are small enough to fit into spaces between the solvent atoms in the crystal lattice, which acts by confining the motion of dislocations (Suzuki et al., 2013). This strengthening mechanism is widely used in the industry; however, several limitations confine the application of this method. In this mechanism, it is important that all metals have the same range of melting point. Furthermore, there is limit into the amount of solute that can be dissolved into the solvent known as the solubility limit.

The precipitation strengthening is processed by heating an alloy at a constant temperature (the aging temperature) and subsequent rapid cooling from a higher temperature (Ardell, 1985). The first plausible explanation for precipitation hardening was introduced as that strengthening occurred in alloys in which the solid solubility increased with temperature, thereby enabling a new phase to form at a lower temperature by precipitation from initially saturated solid solution (Ardell, 1985). The very first explanation of precipitation hardening was used the concept of interaction

between dislocations and the internal stresses produced by misfitting coherent precipitation (Mott & Nabarro, 1940). Later the correlation between the strength of an alloy containing hard particles to the ratio of the shear modulus of the dislocation and the average planar spacing of the particles was derived (Ardell, 1985). The precipitated hardened metals exhibit higher yield strength in the case of polycrystalline material or the critical resolved shear stress (CRSS) of single crystals, however age hardening of metals and alloys can have profound negative effects on ductility, fracture toughness, susceptibility to stress corrosion cracking (Ardell, 1985).

The strength in some alloys may be enhanced by the presence of extremely small (1 nm up to 1 μm) and uniformly dispersed particles within the original phase matrix. The second phase particles are the most potent strengthening agent which controls the mechanical properties of the alloy by acting as pinning sites which hinder the motion of dislocations. There have been many investigations of dispersion hardening method to produce metals with higher flow stress. As an example "SAP" composite was produced by implementing 14% Al_2O_3 in pure aluminum matrix. Another material namely "TD Nickel" was fabricated by using 1-2% ThO_2 in Ni-20%Cr. This strengthening method is widely used for producing cutting tools. For instance cemented carbide is produced by adding tungsten carbide particles into cobalt matrix (Benjamin, 1970).

It is well established that, grain boundaries act as barriers to slip, hence by decreasing a polycrystalline grain size higher number of barriers can be introduced to the structure. Figure 2.2 demonstrates schematic of strengthening by means of dislocation pile-up in grain boundaries (Pearson, 2013).

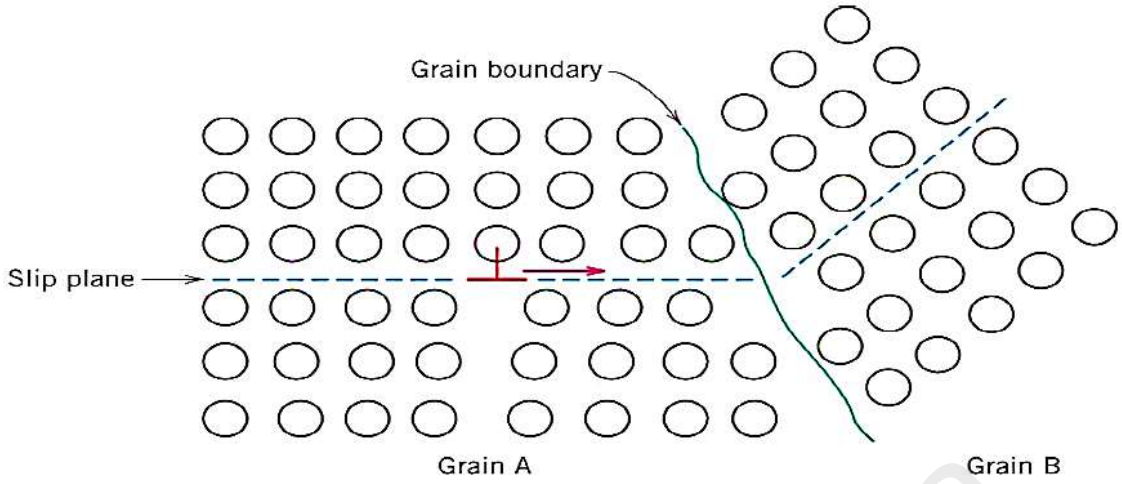

Figure 2.2: Schematic illustration of the motion of a dislocation as it encounters a grain boundary (Pearson, 2013)

Efforts to understand polycrystalline metallic materials work hardening as a function of grain size have a long history. The first finding to be phrased in essentially modern terms was that of Taylor (Taylor, 1934). In this work it was assumed that each grain underwent the same homogeneous strain as did entire workpiece, an incorrect assumption. Later it was shown that deformation could be locally inhomogeneous without invalidating Taylor's calculation of work done; however, has generally not been applied to analyze the work hardening behavior (Bishop & Hill, 1951).

The grain size effect is usually discussed in the yield point, to whether accuracy that may establish in different conditions, and often in flow stress at a higher plastic strain. In this regard, many researches have been accomplished and describe the correlation of grain size and flow stress in the form of power law as (Dunstan & Bushby, 2014):

$$\sigma_y = \sigma_0 + kd^{-x} \tag{2-1}$$

where, σ_0 is the Peierls stress, or it may be the strength due to work-hardening, k is the strengthening coefficient, d is the relevant grain size and x is the scaling factor. Hall and Petch showed that strength of iron and steel depends on grain size (d), with exponent of ½ as:

$$\sigma_y = \sigma_0 + kd^{-1/2} \tag{2-2}$$

From equation (2-2) it follows that the yield strength increases with the reduction of the grain size. Therefore, high strength materials can be processed by refining the grain size into ultrafine grain (UFG) or nanocrystalline structure. UFG materials are formally defined as solid with average grain size of 1μm to 100 nm. Additionally, for bulk UFG metals there are other requirements of fairly homogeneous and equiaxed microstructure. At the same time polycrystalline materials having a grain size smaller than 100 nm are termed as nanocrystalline materials. Materials with UFG structure exhibit higher yield stress, ultimate strength in room temperature compare with coarse grain (CG) structure. Also, fatigue strength and low-temperature superplasticity could be improved by grain refinement of CG structure to UFG structure (Gleiter, 1989; Valiev, 2004).

2.3. Severe plastic deformation methods

In recent years, intensive attention is centered on bulk metallic materials with UFG structure due to the superior mechanical and physical properties. Several methods have been proposed for production of UFG structure materials; however, these methods can be categorized as 'bottom-up' such as methods powder processing methods and 'top-down' like heavy plastic deformation methods (Valiev et al., 2000).

The production of UFG materials using "bottom-up" methods are carried out using techniques such as inert-gas condensation, high-energy milling and cryogenic ball-milling. These techniques allow for wide range of versatility, for example, nanostructure composite materials can be produced by these techniques. However, these techniques require pre-generated small crystalline structure. Moreover, residual porosity and impurity in compact powder can be potentially produced by powder techniques (Gleiter, 1989; Mehrer, 2007).

Severe plastic deformation (SPD) as a "top-down" method was introduced as a direct method for production of bulk UFG structure. The basic idea of SPD techniques is to

introduce large plastic deformation at relatively low operating temperature in presence of high pressure. In this way, the intensive fracture due to the large plastic strain is avoided as a result of unchanged bulk material shape after deformation process. SPD techniques overcome difficulties connected with powder-based techniques such as residual porosity, contamination in the final product; also, SPD techniques have great potential for commercialization (Azushima et al., 2008).

In this regard, over the past three decades various types of SPD techniques have been introduced (Estrin & Vinogradov, 2013); however, three techniques including high pressure torsion (HPT) (Valiev et al., 1991), accumulative roll bonding (ARB) (Saito et al., 1999) and equal channel angular extrusion (ECAE) (Segal, 1999) have the capability for industrial applications. As the main goal of this research is to introduce innovative applications of ECAE, therefore, this method is reviewed in details and regarding two remaining techniques (HPT and ARB) a brief introduction through sections 2.3.1 and 2.3.2 are presented.

2.3.1. High pressure torsion

High-pressure torsion (HPT) refers to a processing technique in which the sample, generally in the form of a thin disk, is subjected to torsional straining under a high hydrostatic pressure (Valiev et al., 2006). The principle of HPT is illustrated schematically Figure 2.3. A method of torsion straining under high pressure can be used for fabrication of disk type samples. An ingot is held between anvils and strained in torsion under the applied pressure (P) of several GPa. A lower holder rotates and surface friction forces deform the ingot by shear. Due to the specific geometric shape of the sample, the main volume of the material is strained in conditions of quasi-hydrostatic compression under the applied pressure and the pressure of sample outer layers. As a result, in spite of large strain values, the deformed sample is not destroyed (Valiev et al., 2006).

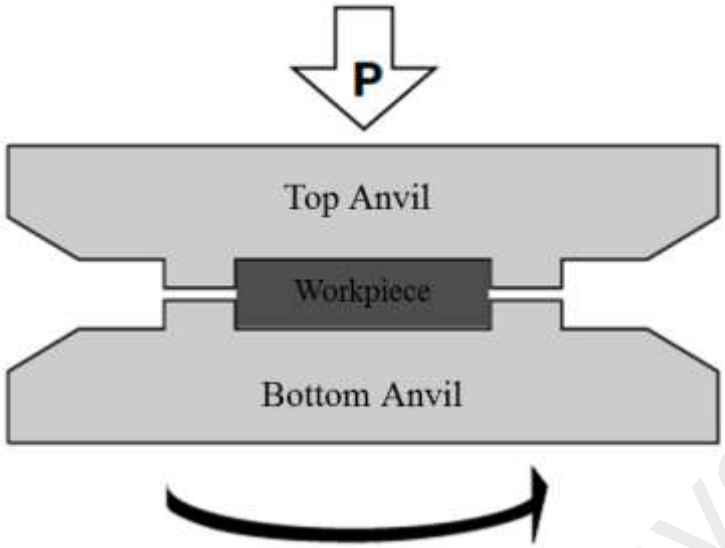

Figure 2.3: Principles of high-pressure torsion: a sample is held between anvils and strained in torsion under applied pressure (P) (Valiev et al., 2006)

2.3.2. Accumulative roll bonding

Accumulative roll bonding (ARB) was developed based on conventional rolling process. In this process, conventional cold rolling process equipment is used in order to produce UFG structure in sheet metallic components. The principle of ARB is illustrated in Figure 2.4.

In this process, a sheet is rolled so that the thickness is reduced to one-half of the thickness in a pre-rolled condition. The rolled sheet is then cut into two halves that are stacked together. To achieve good bonding during the rolling operation, the two contact faces are degreased and wire-brushed before placing them in contact and the stacked sheets are then rolled again to one-half thickness. Thus, a series of rolling, cutting, brushing, and stacking operations are repeated so that ultimately a large strain is accumulated in the sheet. It is possible to heat the sheet when rolling but at a temperature where there is no recrystallization. For the ARB process, the equivalent strain after N cycles, ε_N, is given by $\varepsilon_N = 0.80N$ (Saito et al., 1999; Tsuji et al., 2003).

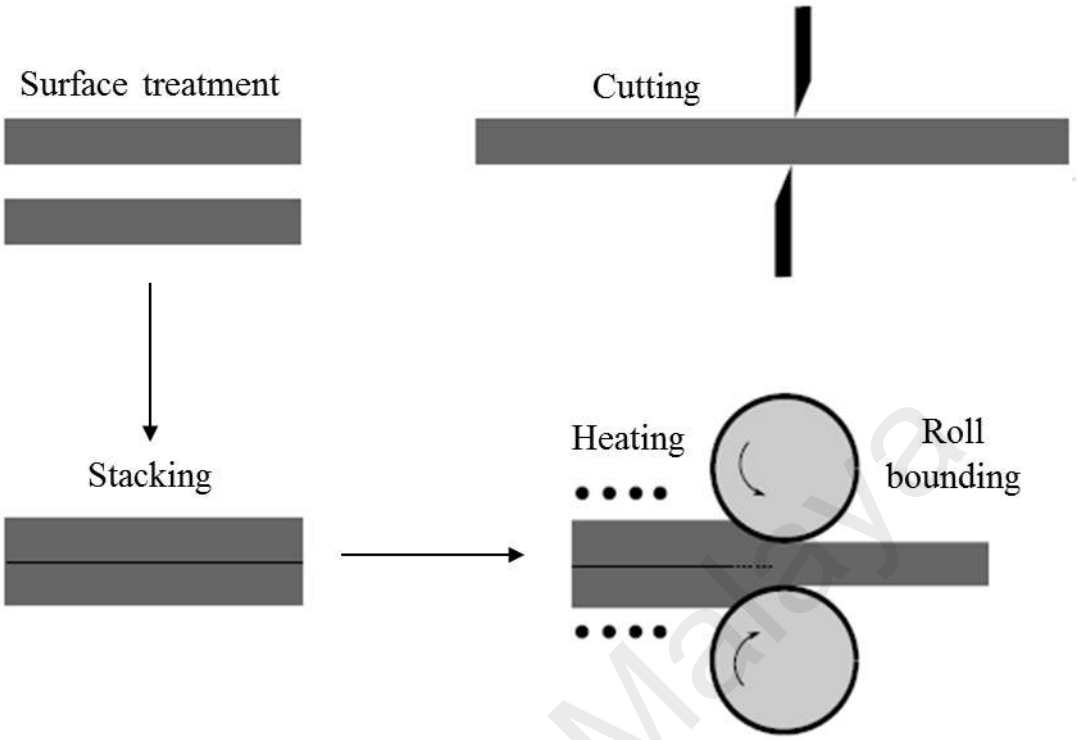

Figure 2.4: The principle of accumulative roll bonding (ARB) (Saito et al., 1999)

2.4. Equal channel angular extrusion

Equal channel angular extrusion (ECAE) was introduced by Segal in the former USSR (Segal, 1999). In this process, a workpiece with circular or rectangular cross-section is extruded using a punch through a special die, consists of two channels with an equal cross-section, intersect by an arbitrary angle, namely channel angle (φ). The outer arch of the die channel can be curved with an inclination angle. The angle of this arch ranges from 0° to π-φ and called corner angle (ψ) (Segal, 1999).

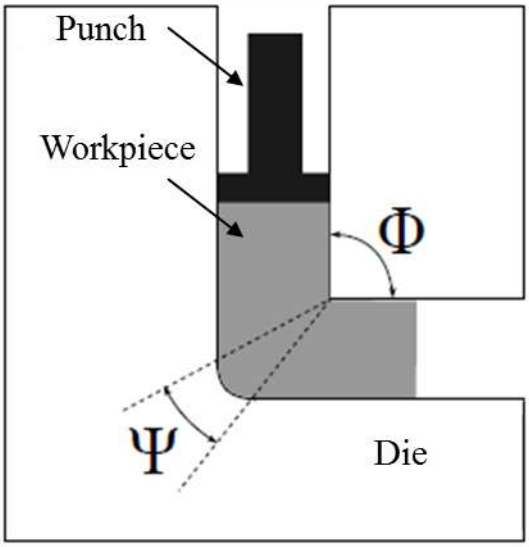

Figure 2.5: The principle of equal channel angular extrusion (ECAE) (Segal, 1999)

Figure 2.5 shows the schematic illustration of ECAE. When a workpiece passes through this abrupt angle, intense shear stress is imposed onto the workpiece while the initial diameter of the workpiece remains unchanged. This extreme shear stress is produced in the workpiece during extrusion and subsequently produces a structure with finer structure. Currently, ECAE is the most common SPD technique for several reasons including (Segal, 1999):

- First, it can be applied to fairly large billets thus creating the potential for producing materials that may be used in a wide range of structural applications.
- Second, it is a relatively simple procedure that is easily performed on a wide range of alloys and, except only for the construction of the die, processing by ECAE uses equipment that is readily available in most laboratories.
- Third, ECAE may be developed and applied to materials with different crystal structures to many materials ranging from precipitation-hardened alloys to intermetallics and metal-matrix composites.
- Fourth, reasonable homogeneity is attained through most of the as-pressed billet provided the pressings are continued to a sufficiently high strain.

- Fifth, the process may be scaled-up for the pressing of relatively large samples and there is a potential for developing ECAE for use in commercial metal-processing procedure.

Repetitive extrusion leads to accumulation of shear strain in the workpiece and ultimately producing workpiece with finer structure. This repetition can be accomplished by considering different strain paths which are obtained by consecutive rotation of the workpiece between extrusion cycles (Valiev & Langdon, 2006). In this regard, four main routes have been developed which determine the workpiece microstructure as a result of different slip systems introduced by each route. These four routes are schematically presented in Figure 2.6, where route A is the consecutive extrusion without rotation of workpiece. The processing in route B is the repetitive extrusion when the workpiece is rotated by 90° and can be divided into routes B_a (90° rotation in opposite sense) and B_c (90° rotation in the same sense). Finally, route C is the 180° rotation of the workpiece in each consecutive extrusion (Langdon et al., 2000).

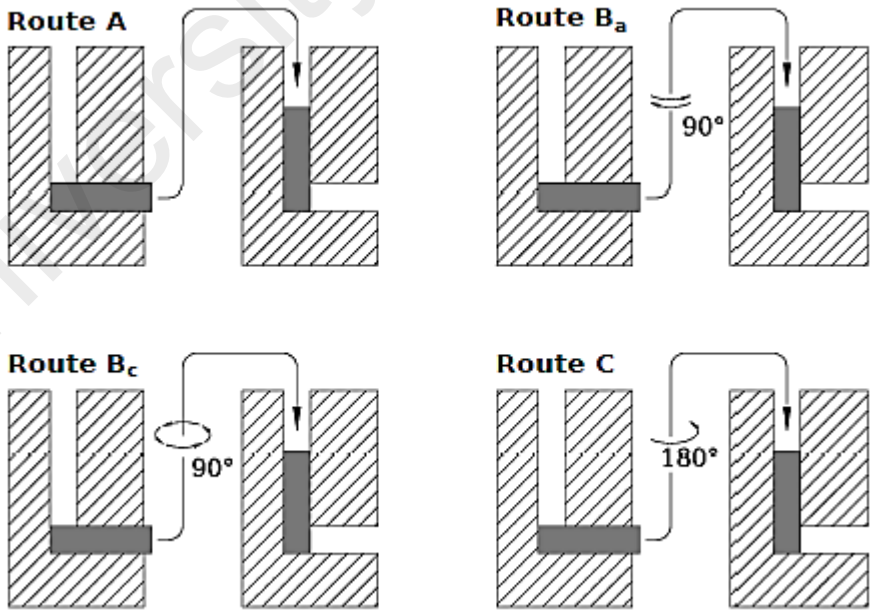

Figure 2.6: Four processing routes for ECAE (Langdon et al., 2000)

Figure 2.7(a) through 2.7(d) schematically illustrates the deformation of a cubic element contained within a workpiece on its passage through the die abrupt angle, where the

shaded plane in Figure 2.7(a) demonstrates the theoretical shear plane. Meanwhile, planes X, Y and Z are the three mutually orthogonal planes of sectioning that lie perpendicular to the longitudinal axis of the pressed workpiece and parallel either to the side faces or to the top face of the sample at the point of exit from the die, respectively.

It is apparent from Figure 2.7(a) that a single pressing through the die shears the cubic element into a rhombohedral shape. However, it is also apparent that the deformation occurring in subsequent pressings will depend upon the nature of any rotation of the sample. The effect of the second passage through the die is shown in Figure 2.7(b) to 2.7(d). It is clear from the figures that route A exhibits a significant distortion of the rhombohedra, route B increases the distortion in the X and Z planes, and route C restores the cubic element so that strain has been introduced to the element without any distortion of the workpiece elements.

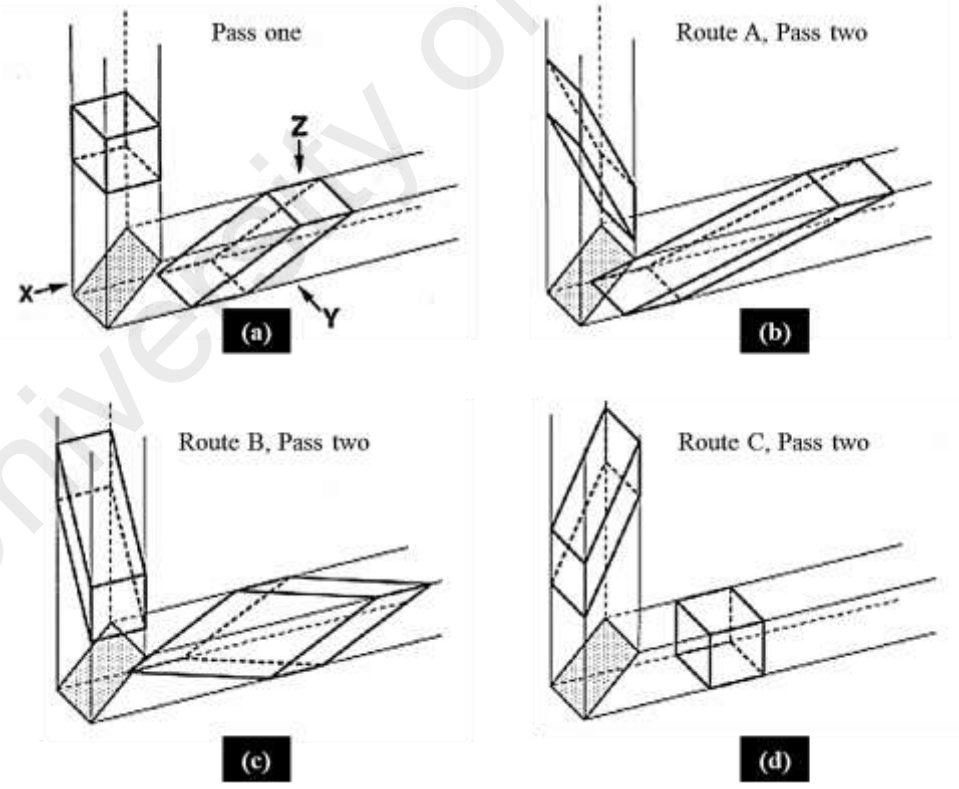

Figure 2.7: Schematic illustration of element distortion in (a) a first pass and second pass in (b) route A, (c) route B and (d) route C (Valiev & Langdon, 2006)

In order to analyze the effect of pressing route on the workpiece microstructure some experimental investigations have been carried out. Literature indicates that route B_c

presents the optimum procedure to obtain a homogeneous equiaxed microstructure with high angle grain boundaries (Langdon et al., 2000; Valiev et al., 2006). It was reported that, the UFG microstructure of aluminum after ten passes in route A was identical to four passes of the process in route B_c (Azushima et al., 2008). Additionally, it is worth to mention that, route B_c provides the optimum dislocation density, grain size, and grain shape for aluminum and titanium, but there is not any evidence that other metals behave similarly.

2.4.1. Equal channel angular extrusion derivative methods and applications

In order to enhance the efficiency of the ECAE process in producing refined structures, as well as to adopt this technique for mass production, a number of modified techniques have been developed in recent years. A repetitive side extrusion process with back pressure with the principle presented in Figure 2.8(a), was developed in order to provides the possibility of producing a workpiece with uniform microstructure (Azushima & Aoki, 2002). Two turn ECAE as illustrate by Figure 2.8(b) is another developed technique to increase the efficiency of the process (Rosochowski & Olejnik, 2002). Moreover, equal channel angular drawing (ECAD) was introduced for production a rod with longer length compared to ECAE as is depicted in Figure 2.8(c) (Chakkingal et al., 1998). Rotary die ECAE (Figure 2.8(d)) has been developed as an energy efficient method which can be repeated up to 30 passes (Estrin & Vinogradov, 2013).

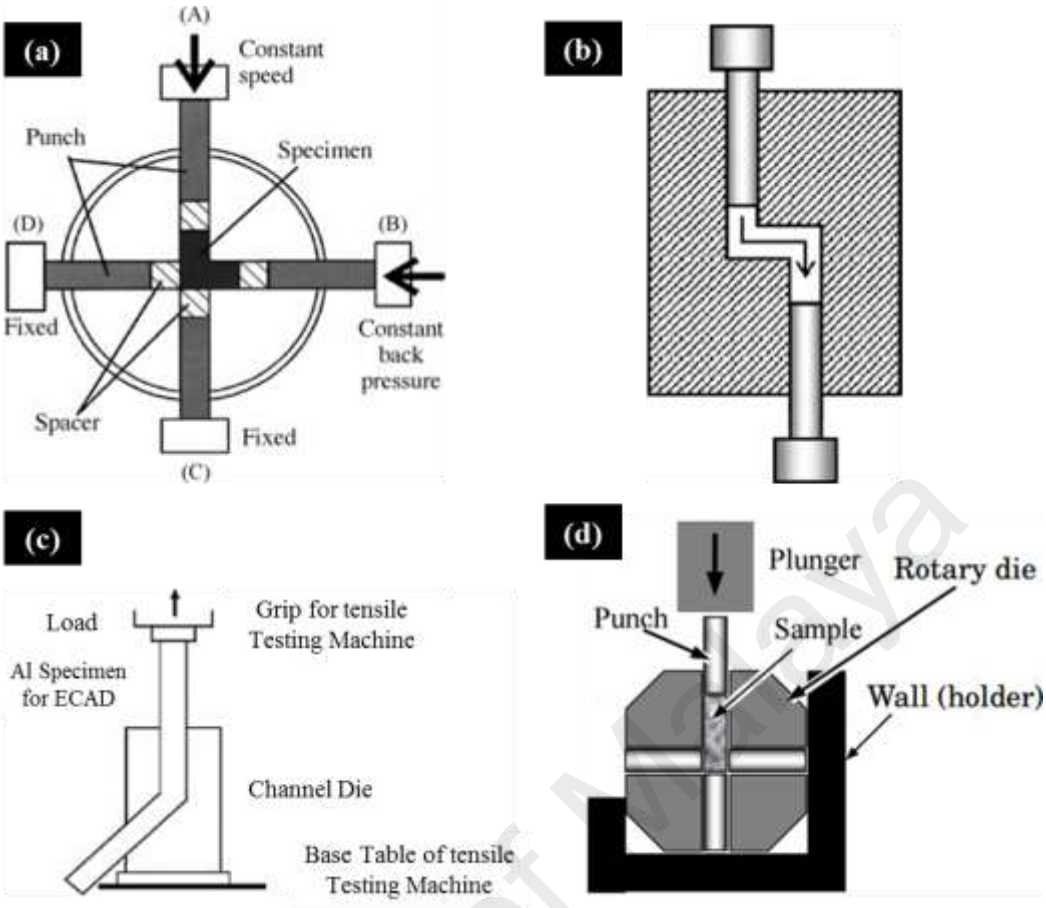

Figure 2.8: Schematic representation of (a) repetitive side extrusion process with the back pressure (Azushima & Aoki, 2002), (b) two-turn ECAE (Rosochowski & Olejnik, 2002), (c) equal channel angular drawing process (ECAD) (Chakkingal et al., 1998), (d) rotary die ECAE (Estrin & Vinogradov, 2013)

Besides the aforementioned processes, other continuous ECAE methods have been developed to increase the production rate (Azushima et al., 2008). Conshearing process was developed as a continuous ECAE for fabrication of the UFG sheet metal product. In this process, the ECAE die is positioned at the end of satellite mill as illustrated in Figure 2.9(a). Continuous confined strip shearing (C2S2) was developed as another continuous ECAE process for fabrication of UFG sheet product. The principle of the process is similar to conventional rolling process, except that the lower roller with a high rough surface is used, in order to feed the sheet into the ECAE die as illustrated in Figure 2.9(b). The advantage of this technique over conshearing is a possibility of using ECAE die with 90° channel angle (Lee et al., 2001).

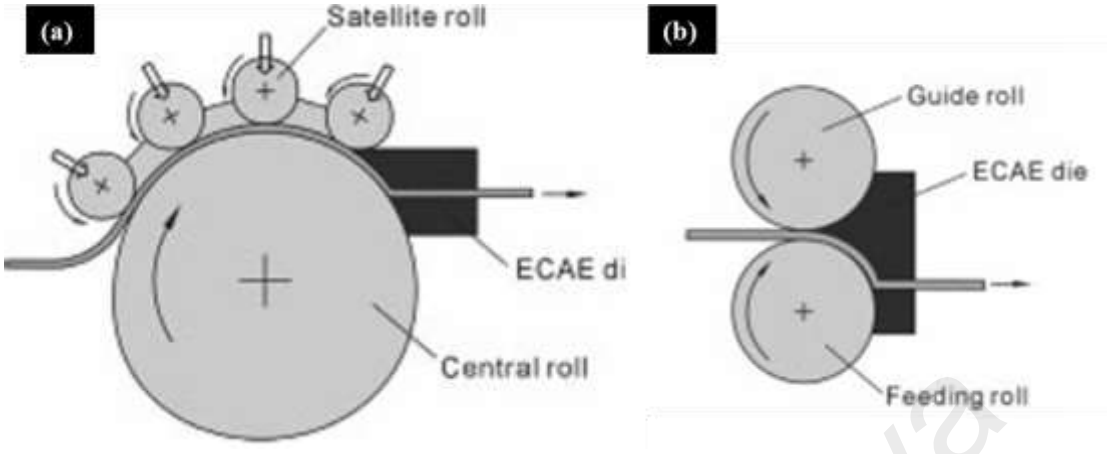

Figure 2.9: Schematic illustration of (a) conshearing process (Saito et al., 2000) and (b) continuous confined strip shearing (C2S2) (Lee et al., 2001)

In addition, researches have been carried out to study the capability of ECAE to produce wires with ultrafine microstructure, gears for MEMS applications and steel components for cryogenic applications (Valiev et al., 2007). Also, ECAE was used for fabrication of ex situ metal-ceramic composites (Casati et al., 2014). In this research, commercially pure aluminum and Al_2O_3 powders were consolidated by ECAE which resulted in nanocomposite matrix with ultrafine structure and high homogeneity. Moreover, the capability of ECAE for consolidation of Ti-6Al-4V powder was taken under consideration (Yapici et al., 2003). In another work, ECAE was successfully used to consolidate commercially pure titanium chips into a fully dense bulk rod (Luo et al., 2012). Moreover, ECAE was successfully used for fabrication of laminated composite (bi-layer and multi-layer) of different alloys (Han et al., 2010; Liu et al., 2009).

2.4.2. Application of ECAE for possessing tubular components

Tubular components are widely used in many branches of engineering such as aircraft, automotive, cooling towers, pressure vessels, pipelines and offshore platforms. Hence, production of tubular components with promising mechanical properties remains a primary driver in material science.

A number of researches have been carried out in order to develop SPD methods for processing bulk material with primary shapes of a rod, block and sheet; however, the SPD methods for processing of tubular components is less developed and limited to laboratory methods. With this regard, a variety of SPD processes, such as tubular channel angular pressing (TCAP) (Faraji et al., 2011), tube channel pressing (TCP) (Farshidi et al., 2014), high-pressure tube twisting (HPTT) (Tóth et al., 2009), and stagger spinning (Xia et al., 2014) have been developed to produce UFG structures with tubular geometries. Tubular materials with UFG structures can be successfully produced via these methods; however, limitations such as low production rates, material inhomogeneity, short lengths of the final product, and SPD process complexity have restricted their widespread applicability for mass production.

TCAP was designed based on the pressing the tubular components into the die which the diameter of workpiece experiences expansion in the first pass. In order to obtain the initial shape, disassembly of the die is necessary and workpiece should be trimmed and pressed again. This process was used for SPD treatment of commercial AZ91 magnesium alloy and a significant enhancement in hardness from 51 HV to 78 HV was obtained after one cycle (Faraji et al., 2011). However, the die set in this method of SPD is very complicated and low surface quality as well as short length of the tube limits the industrial application of this method.

TCP was used for SPD treatment of tubular AA 6061-O with thickness of 3 mm. Results showed notable improvement in mechanical properties in the terms of yield stress, ultimate strength and hardness, which increased up to 2 times after 5 passes (Farshidi et al., 2014). The rotation of the die after each pass or a designed press with two rams is necessary in this process which reduces the applicability of this process for mass production.

A technique was also developed which introduced the processing of tubular components with thin wall. In this process workpiece's inner surface are constrained by a mandrel with specified elastic modulus also the outter surface constrained by a die. The mandrel is pressed by press ram and as a consequence of the mandrel's slight expansion in the radial direction, a large hydrostatic stress is imposed onto the tube. This hydrostatic stress provides a large friction force on both sides of the tube and by a simultaneous rotation of the die the SPD process is completed. However, the complexity of this process and tube thickness limit the wide application of this process (Tóth et al., 2009).

Stagger spinning is another SPD technique for producing UFG structure in thin walled tubular components, based on power spinning process. In this process the inner surface of the tube is constrained by a mandrel and three rollers are positioned on the same longitudinal cross-section which controlled the thinning ratio of tube. It is worth mentioning that in this process the initial dimension of tube is changed as a result of tube thinning.

In a prior study, the ECAE process was modified to produce pure titanium components with UFG structures, in which sand-filled titanium tubes were extruded through a die with a 150° channel angle (Nagasekhar et al., 2006). In another study, pure tubular copper with an initial wall thickness of 3.5 mm was successfully ECAE-treated with a flexible polyurethane rubber pad (Djavanroodi et al., 2013). Microhardness results from this study revealed a 32% and 57% improvement after the first and fourth passes, respectively.

2.4.3. Application of ECAE for joining dissimilar materials

The inevitable need to enhance energy efficiency through decreasing fuel consumption has considerably boosted demand for lightweight materials over the last decade in various transportation industries (Hirsch & Al-Samman, 2013). High strength steels

have been amongst the most promising materials for structural components. However, their relatively high density has urged industries to utilize thinner steel sheets to lighten structures, which may deteriorate the crashworthiness of components. To solve this issue, a variety of lightweight materials including magnesium alloys and aluminum alloys have been employed as substitutes for steels. Amongst them, aluminum alloys have attracted exceptional attention due to their high strength-to-weight ratio and excellent corrosion resistance. However, the sole usage of aluminum alloys in mass production is not cost effective (Taban et al., 2010). Hence, considering the need for components with high strength, low weight, and reasonable price, combining steels and aluminum alloys through dissimilar material joining methods seems an ideal solution. Due to outstanding applicability, the dissimilar joining of steels and aluminum alloys has undergone extensive research in order to find which joining techniques offer desirable quality while lessening the final cost and amount of labor.

Depending on the operating temperature, applied pressure and state of materials during joining, steel-to-aluminum joining techniques fall into three categories: fusion joining, solid-state joining and mechanical fastening (Mori et al., 2013). The tremendous discrepancies in the thermo-physical properties of steel and aluminum alloys, including heat conductivity and coefficient of thermal expansion, can lead to the formation of structural deficiencies, such as residual stress storage, crack nucleation, and porosity formation during fusion joining (Dharmendra et al., 2011). Furthermore, the metallurgical incompatibility between these two materials originates from their poor solid solubility that can promote the formation of brittle Fe-Al intermetallic compounds, which are detrimental to a joint's mechanical properties (Yan et al., 2010).

Amongst the solid-state methods, joining by plastic deformation is a promising technique of joining dissimilar materials with sufficient ductility, such as steel and aluminum alloy owing to minimal thermal effects as well as reduced residual stress

(Mori et al., 2013). A technique for the plastic joining of a high-strength serrated shaft and a disc was introduced to produce an automobile axle by inducing the shaft into the disc hole at room temperature (Kitamura et al., 2012). In another plastic joining process, shafts made of high-strength steel were directly infixed into high-temperature discs (Matsumoto et al., 2008). In another study, the rotary swaging process was utilized in order to join tube/tube cupric parts, which produced joints with acceptable tensile properties (Zhang et al., 2014). Friction stir welding is another joining process to produce plastic joints between dissimilar metals (Wu et al., 2015). Cold roll bonding is another solid state joining method which has been employed to join dissimilar metal sheets of aluminum and steel. In a study, the bond strength of Al/Fe joints processed through cold roll bonding was measured as 17.6 MPa (Yang et al., 2009).

Despite the advantages furnished by the methods mentioned above, plastic joining through SPD provides the extra benefit of producing metallic components with UFG structure and superior mechanical properties (Valiev et al., 2015). ECAE process was employed to produce bimetallic components (Eivani & Taheri, 2007). This investigation proved the capability of this method to produce promising joints between aluminum and copper.

2.5. Process parameters

2.5.1. Effect of die geometry

Microstructure evolution of metallic materials through plastic deformation has been extensively studied over the last few decades (Sevillano et al., 1980). It is generally accepted that in ambient temperature average grain size decreases by accumulating strain at metallic materials. Therefore, understanding the phenomena associated with strain evolution in a workpiece is important to design successful ECAE process. The deformation behavior in ECAE is pure shear, similar to pure torsion; however, the main difference between ECAE and pure torsion or other plastic deformation processes is that

deformation takes place in the immediate vicinity of plane pass through the intersection of the two die's channel (Kim et al., 2001). Hence, the deformation zone in ECAE treated workpiece is localized compared to pure torsion. Figure 2.10 schematically illustrates an element deformation behavior through pure shear and ECAE for a die with channel angle of (φ) and corner angle (ψ) of 0°.

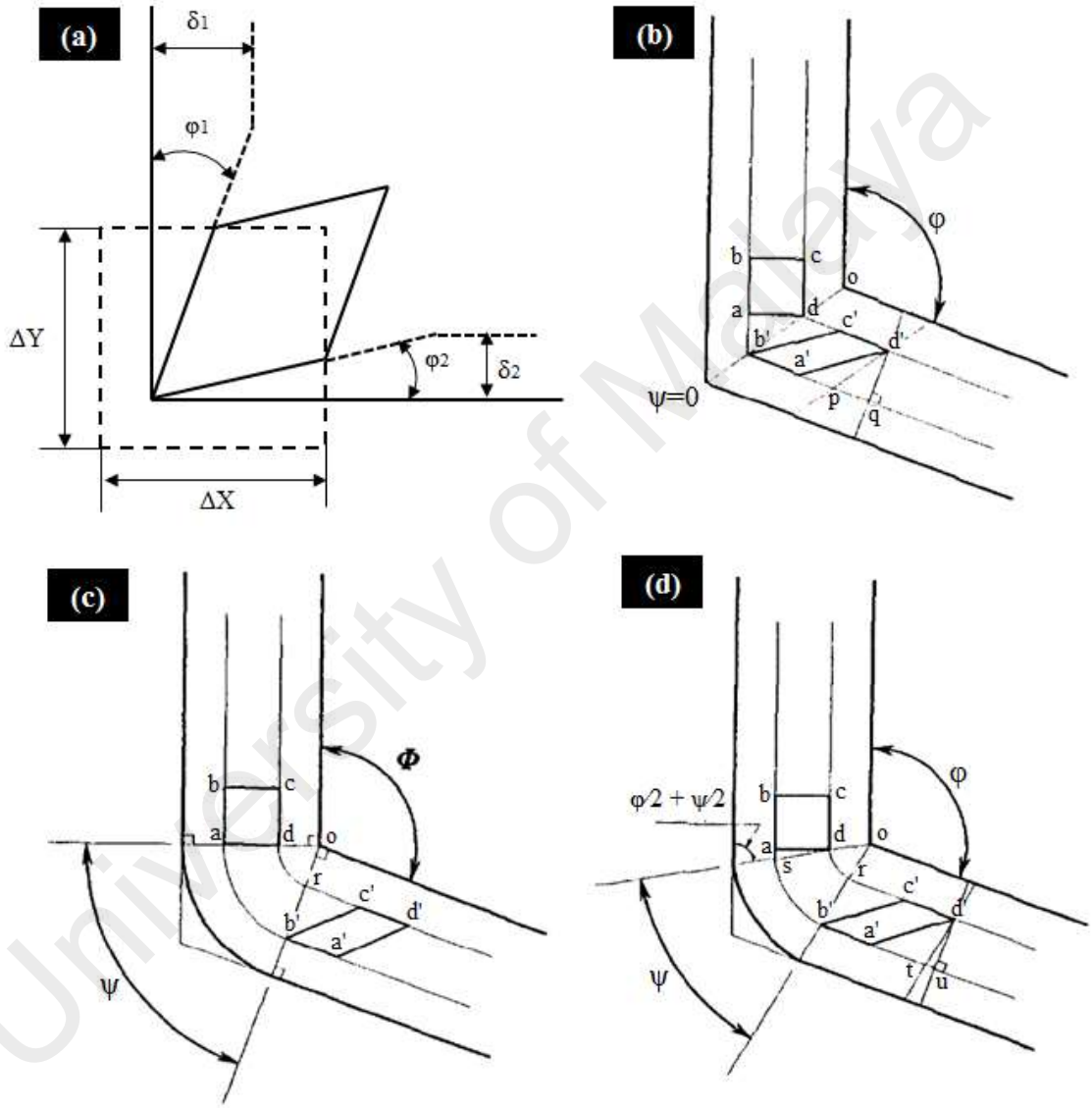

Figure 2.10: Schematic illustration of a deformed elements in (a) pure shear and moving through the ECAE die with (b) ψ=0, (c) ψ=π-φ and (d) ψ lies between 0 and π-φ (Segal, 1999)

In order to measure the distortion of an element under pure shear stress (arbitrary deformation) in a plane, the engineering shear strain (γ) is defined for an element with

length of ΔX and height of ΔY (Figure 2.10(a)) as shown below(Chandrupatla et al., 1997) :

$$\gamma = \varphi_1 + \varphi_2 \tag{2-3}$$

where, φ_1 and φ_2 are distortion angles. These two angles are considered as a function of displacement fields' $u = (x, y)$ in the x direction and $v = (x, y)$ in the y. Therefore displacement vector is defined as:

$$\underline{u} = u(x, y)i + v(x, y)j \tag{2-4}$$

Hence, the γ can be defined as a function of displacement field as $\gamma(x, y)$ and φ_1 and φ_2 are defined as:

$$\varphi_1 \cong tan\varphi_1 = \frac{\delta_1}{\Delta Y} \tag{2-5}$$

$$\varphi_2 \cong tan\varphi_2 = \frac{\delta_2}{\Delta X} \tag{2-6}$$

δ_1 is a displacement in x direction but it comes because of change in y, and likewise δ_2 is a displacement in y direction but it comes because of change in x. Therefore:

$$\delta_1 = \frac{\partial u}{\partial y}\Delta Y + O(\Delta Y^2) \tag{2-7}$$

$$\delta_2 = \frac{\partial v}{\partial x}\Delta X + O(\Delta X^2) \tag{2-8}$$

Hence, by considering equations (2-5) and (2-6), this will give:

$$\varphi_1 = \frac{\partial u}{\partial Y} + O(\Delta Y^2) \tag{2-9}$$

$$\varphi_2 = \frac{\partial v}{\partial X} + O(\Delta X^2) \tag{2-10}$$

By considering equation (2-3) we have:

$$\gamma = \frac{\partial u}{\partial Y} + \frac{\partial v}{\partial X} \tag{2-11}$$

The homogeneous distribution of strain in the entire workpiece through ECAE can be obtained if the deformation follows pure shear perfectly. Figure 2.10(b) illustrates the principle of ECAE for die with channel angle of φ and corner angle of ψ=0. A small initially square element $abcd$ becomes deformed by shear onset of passage through die abrupt angle into the configuration given by $a'b'c'd'$. Therefore shear strain, γ, by considering equations (2-3) and (2-5) will give us:

$$\gamma = \frac{a'q}{d'q} \tag{2-12}$$

From Figure 2.10(b), $qd' = ad$ and $ab' = dc' = a'p = pq = adcot(\varphi/2)$. Therefore, for the condition where ψ=0:

$$\gamma = 2\cot(\frac{\varphi}{2}) \tag{2-13}$$

In Figure 2.10(c) where ψ=π-φ, the shear strain, γ is given by:

$$\gamma = \frac{rc'}{rb'} \tag{2-14}$$

where, $rb' = da = oa - od$ and $ab' = dc' = oa\psi = (rc' + od\psi)$ so that $rc' = (oa - od)\psi$. Therefore, for this condition:

$$\gamma = \psi \tag{2-15}$$

In the situation where ψ represent an intermediate angle between 0 and π-φ as is indicated by Figure 2.10(d), the shear strain, γ, is given by:

$$\gamma = \frac{a'u}{d'u} \tag{2-16}$$

where, $d'u = ad$ and $a'u$ is obtained from the $a'u = (a't + tu) = (rc' + as)$, $as = adcot(\varphi/2 + \psi/2)$, $ab' = dc' = (as + os\psi) = rc' + od\psi$ and $(os - od) = adcosec(\varphi/2 + \psi/2)$, so that $a'u = 2adcot(\varphi/2 + \psi/2) + ad\psi cosec(\varphi/2 + \psi/2)$. Therefore, shear strain, γ, for this condition is given by:

$$\gamma = 2cot(\varphi/2 + \psi/2) + \psi cosec(\varphi/2 + \psi/2) \quad (2\text{-}17)$$

The equivalent plastic strain ε_{equ} in general form is represented by:

$$\varepsilon_{equ} = \sqrt{2/3}\,[\varepsilon_x^2 + \varepsilon_y^2 + \varepsilon_z^2 + \frac{\gamma_{xy}^2 + \gamma_{yz}^2 + \gamma_{zx}^2}{2}]^{1/2} \quad (2\text{-}18)$$

By substituting equation (2-17) into equation (2-18) and considering $\varepsilon_x = \varepsilon_y = \varepsilon_z = \gamma_{yz} = \gamma_{zx} = 0$ the equivalent strain, ε_{equ} after one pass is given by (Segal, 1999):

$$\varepsilon_{equ} = \frac{1}{\sqrt{3}}(2cot(\varphi/2 + \psi/2) + \psi cosec(\varphi/2 + \psi/2)) \quad (2\text{-}19)$$

Since the same amount of strain is accumulated in the workpiece after each pass, the equivalent plastic strain, ε_{equ} after P extrusion pass is calculated as:

$$\varepsilon_{equ} = \frac{P}{\sqrt{3}}(2cot(\varphi/2 + \psi/2) + \psi cosec(\varphi/2 + \psi/2)) \quad (2\text{-}20)$$

It is worth mentioning that, common assumptions in this geometric analysis of strain include: die surfaces are frictionless, the workpiece completely fill channel and material behavior is close to ideal (rigid perfectly plastic) (Li et al., 2004).

Microstructure homogeneity and hardness uniformity are proportional to homogeneity of the EPS, which is imposed on the workpiece by SPD process (Horita & Langdon, 2005). Strain inhomogeneity index (C_i) has been proposed as a factor to quantify the degree of deformation inhomogeneity as (Li et al., 2004):

$$C_i = \frac{\bar{\varepsilon}_{max}^P - \bar{\varepsilon}_{min}^P}{\bar{\varepsilon}_{ave}^P} \quad (2\text{-}21)$$

where, $\bar{\varepsilon}_{max}^P$, $\bar{\varepsilon}_{min}^P$ and $\bar{\varepsilon}_{ave}^P$ indicate the maximum, minimum and average effective plastic strain, respectively. Die channel angle (φ) and die corner angle (ψ) are the origin of in-homogeneity behavior in ECAE process (Wei et al., 2006). The evaluation of C_i for different die configuration indicated that increasing die channel angle (φ) will

decrease C_i values, while having a reverse effect on amount of EPS accumulated in the workpiece (Nagasekhar & Tick-Hon, 2004).

2.5.2. Extrusion pressure

Extrusion pressure is an important factor for successful ECAE process design. It determines the capacity of required press and also gives the estimation of forces that are imposed onto the die and punch throughout the process. Exact analytical solutions for the required extrusion force through ECAE must be both statically (geometrically self-consistent) and kinematically (satisfying required stress equilibrium everywhere in the deforming body) admissible. Frequently it is simpler to use limit theorems that allow one to make analyses that result in calculated forces that are known to be either correct or too high or too low than the exact solution.

Lower bound analysis has been proposed as an analytical method based on satisfying stress equilibrium while ignoring geometric consistency. Therefore, this method estimates lower or correct amount of plastic deformation force. On the other hand, upper-bound analyses predict stress or forces that are known to be too large. Upper bounds are based on satisfying yield criteria and geometric self-consistency while no attention is paid to satisfying equilibrium.

An upper bound based solution was proposed by (Alkorta & Sevillano, 2003) in order to show the effect of different ECAE parameters such as channel angle and material hardening behavior on extrusion force in the absence of friction. According to these authors, in the particular case of a Hollomon-type strain-hardening ($\sigma(\varepsilon) = \sigma_0 \varepsilon^n$) behavior of materials the pressure was calculated as follows:

$$P_{ECAE} = \int_0^{\varepsilon_p} \sigma(\varepsilon) d\varepsilon = \frac{\sigma_0}{1+n} \left[\frac{2\cot((\varphi+\psi)/2) + \psi}{\sqrt{3}}\right]^{1+n} \quad (2\text{-}22)$$

Voce-type strain-hardening behavior, which gives a more realistic strain-hardening behavior of metallic materials described as (Sevillano et al., 1980):

$$\frac{\sigma_s - \sigma}{\sigma_s - \sigma_Y} = \exp(-\frac{\varepsilon - \varepsilon_Y}{\varepsilon_c}) \quad (2\text{-}23)$$

where, σ_s, σ_Y, ε_Y and ε_c are the material constants. By considering equation (2-23), the extrusion pressure was obtained as (Alkorta & Sevillano, 2003):

$$P_{ECAE} = \sigma_s.\varepsilon_p - \varepsilon_c(\sigma_s - \sigma_Y) \times [\exp\left(\frac{\varepsilon_Y}{\varepsilon_c}\right) - \exp\left(-\frac{\varepsilon_P - \varepsilon_Y}{\varepsilon_c}\right)] \quad (2\text{-}24)$$

2.5.3. Effect of friction

Friction is one of the important process parameters, which retards the flow of the surface materials and subsequently increase the shear strain at the bottom region and lower shear strain at the top region of the workpiece. In ECAE, friction is one of the important factors which affect overall deformation behavior, load requirement and strain evolution.

It was reported that, strain and inhomogeneous deformation increase by friction. Furthermore, friction condition changes the degree in which the die's internal corner is filled and the magnitude of the shear developed within the homogeneously deformed section of the workpiece (Prangnell et al., 1997). Similarly, it was reported that, strain homogeneity increase with friction (Dumoulin et al., 2005; Suo et al., 2006). However, there are contradictory results which indicate that strain is independent of friction by considering the material strain hardening behavior(Yang & Lee, 2003).

In order to analyze the effect of friction on strain evolution, required punch pressure and material deformation behavior through ECAE; coulomb and shear friction models have been vastly used by researchers. The effect of coulomb and shear friction model through metal forming processes have been investigated and results show that in friction sensitive processes the coulomb friction model provides more acceptable results than

shear friction model. However, the conventional practice is to use shear friction model for bulk metal working processes such as forging, extrusion and coulomb friction model for sheet metal forming (Joun et al., 2009).

Coulomb's law is the most common form of friction law, which states, that the magnitude of friction forces (f_F) is proportional to the magnitude of the normal force (f_N) as:

$$f_F = \mu f_N \tag{2-25}$$

where, μ is called the friction coefficient or coulomb constant. Equation (2-25) equivalently can be expressed the state of stress as:

$$\sigma_F = \mu \sigma_N \tag{2-26}$$

where, σ_F and σ_N represent friction stress and normal stress, respectively. Coulomb's law is conceptually correct at very small pressures, i.e. the limiting tangential force approaches zero as the pressure tends to zero. This friction law is usually found applicable at low contact pressures relative to material strength, before a great deal of deformation. However, at higher contact pressure, materials properties should enter into consideration (Wagoner & Chenot, 1996).

Equation (2-26) can be expressed numerically in sticking and slipping conditions as follow (Wagoner & Chenot, 1996):

$$\| \sigma_F \| < \mu \sigma_N \tag{2-27}$$

$$\| \sigma_F \| = -\mu \sigma_N . t \tag{2-28}$$

where, equations (2-27) and (2-28) represent sticking and sliding conditions respectively. Relative velocity v_r is presented by tangential vector t in equation (2-28) along the sliding direction, which is expressed as $t = \frac{v_r}{\|v_r\|}$.

From equations (2-27) and (2-28), a discontinuity in friction forces during the transition from sticking condition to sliding one can be concluded, which cause difficulty in numerical simulation. Hence, the arctangent model based on continuously differentiable function in terms of the relative sliding velocity was proposed as (Chen & Kobayashi, 1978):

$$\sigma_F = -\mu\sigma_n \frac{2}{\pi}\tan^{-1}\left(\frac{\| v_r \|}{\alpha}\right).t \tag{2-29}$$

where, α is the value of relative sliding velocity below which sticking occurs.

While coulomb friction law properly estimates the friction force for non-deforming bodies, it notably overestimates the friction at high contact pressures. It was shown that friction at the contact region cannot exceed the shear strength even if interface bounded tightly (welded). This extreme condition called sticking and generally represented as:

$$\sigma_F = \tau_{max} \tag{2-30}$$

where, τ_{max} is the shear strength of the softer material alone. According to the Tresca yield criterion, the shear strength is calculated as:

$$\tau_{max} = \frac{\bar{\sigma}}{2} \tag{2-31}$$

According to Tresca yield criterion, onset of yielding depends only on the largest shear strength in the body. With the convention, if we consider $\sigma_1 \geq \sigma_2 \geq \sigma_3$, this criterion can be expressed as $\sigma_1 - \sigma_2 = Y$. The constant *Y* can be found by considering a tension test, where Y is the yield strength of the material.

By considering the von Mises yield criterion the shear strength can be found as:

$$\tau_{max} = \frac{\bar{\sigma}}{\sqrt{3}} \tag{2-32}$$

The von Mises criterion postulates that yielding will occur when the value of the root-mean-square shear stress reaches a critical value. This is expressed mathematically as:

$$\bar{\sigma} = [(\sigma_1 - \sigma_2)^2 + (\sigma_2 - \sigma_3)^2 + (\sigma_3 - \sigma_1)^2] = 2Y^2 \quad (2\text{-}33)$$

where σ_1, σ_2, and σ_3 were principle stresses values.

A modification to sticking friction was proposed based on the fact that, shear strength seldom exceed the shear strength of the softer material. This generalization is expressed as follows,

$$\sigma_F = m\tau_{max} \quad (2\text{-}34)$$

where, *m* is constant known as the friction factor. According to the shear friction model the sticking and slipping conditions can be expressed similarly to coulomb friction model as:

$$\| \sigma_F \| < m\frac{\bar{\sigma}}{\sqrt{3}} \quad (2\text{-}35)$$

$$\| \sigma_F \| = -m\frac{\bar{\bar{\sigma}}}{\sqrt{3}}.t \quad (2\text{-}36)$$

The shear friction model is also implemented using the arctangent approximation as follows,

$$\sigma_F = -m\frac{\bar{\sigma}}{\sqrt{3}}\frac{2}{\pi}\tan^{-1}\left(\frac{\| v_r \|}{\alpha}\right).t \quad (2\text{-}37)$$

Coulomb friction model was employed to analyze effects of friction through ECAE and results indicated significant influence of friction on the deformation inhomogeneity (Suo et al., 2006). In another research, three cases including frictionless condition (ideal condition), varying shear friction factor (*m*=0.025, 0.05 and 0.1) and varying coulomb friction coefficient (μ=0.025, 0.05 and 0.1) were considered to analyze strain inhomogeneity, workpiece corner gap and punch pressure through ECAE (Balasundar & Raghu, 2010). Results showed the corner gap between workpiece and die decreases gradually with shear friction but rapidly with coulomb friction model. Moreover, the inhomogeneous deformation measured using the deformation inhomogeneity index was

found to increase gradually with increasing shear friction value but rapidly with coulomb friction model. For a friction value of 0.1, coulomb model predicts a highly inhomogeneous deformation with fold formation. Furthermore, the load required to deform a strain hardening material in an ECAE process cannot decrease continuously and hence the predictions of coulomb friction model are not correct. The current coulomb friction model has to be modified to reduce the friction force when the shear stress reaches a limiting value so that it can be used in ECAE process.

2.5.4. Effect of pressing speed and temperature rise effect

Pressing speed is one of the important factors which affects heat generation pattern through ECAE, which in turn induces phase transformation or change in micro structure significantly in grain boundaries. As a result of this variation, flow stress of the workpiece material as well as other mechanical properties may change with different pressing speeds.

The ECAE can be considered as the steady state process like hot rolling or casting except for two end parts of the workpiece, as the length of the workpiece is much greater than its diameter. Heat transfer in ECAE can be described by means of convention $(\rho C u(\frac{dT}{dt}))$, where ρ, C, u, T and t denote density, heat capacity, velocity, temperature and time, respectively. Heat transfer by the means of conduction is defined as $(k(\frac{d^2T}{dx^2}))$, where k and x are thermal conductivity and coordinate in the length direction, respectively. In ECAE due to the high-speed motion of the workpiece the effect of convection is significantly higher than conduction and therefore, the conduction effect can be neglected through analysis. This generated temperature is stored in the workpiece and also transferred to the die.

The ideal work (*w*) through plastic deformation is obtained as (Kobayashi et al., 1989):

$$w = \int_0^{\varepsilon} \bar{\sigma} d\bar{\varepsilon} \tag{2-38}$$

The internal heat generation due to plastic deformation work is almost 90% of the ideal work. Hence, the workpiece shape remains unaltered after the ECAE process stress saturated in the workpiece and equation (2-38) is then approximated as (Kobayashi et al., 1989):

$$w = \bar{\sigma}\bar{\varepsilon} \tag{2-39}$$

where, ε is the final strain and σ represents the final amount of saturated stress in the workpiece. The heat generation per unit area between the workpiece and die (q_s) is calculated as (Kobayashi et al., 1989):

$$q_s = \sigma_F u = m\left(\frac{\bar{\sigma}}{\sqrt{3}}\right)u \tag{2-40}$$

The frictional heat considered to be distributed uniformly between the workpiece and die, thus, half of the frictional heat considered to be transferred to workpiece. By neglecting the temperature distribution within main deformation zone, the heat transfer problem reduces to a lumped analysis, in which details of temperature distribution within workpiece is neglected and an average temperature increment is considered. Therefore, energy balance can be written as (Kim, 2001):

$$\rho C V \Delta T = 0.9\bar{\sigma}\bar{\varepsilon}V - Ah\Delta T\Delta t + 0.5m\left(\frac{\bar{\sigma}}{\sqrt{3}}\right)uA\Delta t \tag{2-41}$$

where, *V*, *ΔT*, *A*, *Δt* and *h* denote the volume of the calculation domain, the temperature increment in the domain, the outer surface area of the workpiece which is in contact with the die, the dwell time of the domain within deforming zone and the heat transfer coefficient between die and workpiece, respectively. In this equation, the left hand side term is the energy stored in the workpiece and the first term at the right side is the energy generated through plastic deformation. Second and third terms denote heat

transferred to the outer part of the deforming zone and heat generated as a result of friction, respectively. By taking the passing time of the volumetric center point through the main deforming zone, the average dwell time *Δt* can be obtained as (Kim, 2001):

$$\Delta t = \frac{D}{u}\frac{\psi}{\pi\sqrt{2}} \tag{2-42}$$

where, *D* is the diameter of the workpiece. Therefore, temperature rise during the ECAE process, *ΔT,* can be obtained as (Kim, 2001):

$$\Delta T = \frac{0.9\bar{\sigma}\bar{\varepsilon} + 0.5m\left(\frac{\bar{\sigma}}{\sqrt{3}}\right)u\frac{A}{V}\Delta t}{\rho C + \frac{A}{V}h\Delta t} \tag{2-43}$$

where, the volume (*V*) and the surface area (*A*) of the main deformation zone are:

$$V = (\pi^2/4)D^3(\varphi/2\pi) \tag{2-44}$$

$$A = (\pi^2 D^2)(\varphi/2\pi) \tag{2-45}$$

Considering equation (2-43) it can be interpreted that material parameters and process factor determine the temperature rise during ECAE. In this regard, flow stress of the material, punch speed, strain, dies channel angle; die initial temperature and friction factor are the parameters that increase the workpiece temperature during the process. On the contrary, workpiece density, heat capacity, die corner angle and die cooling rate are the parameter that decrease the temperature.

The reports regarding the effect of temperature rise on materials property through ECAE is rather contradictory. Influence of pressing speed on microstructural evolution through ECAE indicated that the speed of pressing has no significant influence on the equilibrium grain size of pure Al and Al-1% Mg alloy (Berbon et al., 1999). However, it was reported that strain rate and strain hardening exponent determine the accumulation and distribution of dislocations (Kim et al., 2001).

2.6. Numerical simulation of ECAE process

Due to the industrial prospects of ECAE, significant progress has been made not only in the understanding of fundamental properties of ECAE-treated materials such as strength fatigue, superplasticity, elasticity, internal friction and corrosion but also in analyzing the process itself. Because the evolution of microstructures and mechanical properties of the deformed material are directly related to the amount of plastic deformation, understanding the phenomenon associated with the strain development is very important in ECAE. In this regard, many theoretical methods have been proposed to interpret deformation behavior of workpiece during ECAE, such as strain analyzes using geometrical consideration, smooth particle hydrodynamic (SPH), upper bound analysis and finite element analysis (FEA).

Common assumptions in these geometrical analyses are die workpiece frictionless contact condition, the plastic flow occurs uniformly over a plane perpendicular to workpiece axis, the workpiece completely fills the die cavity and the material behavior is close to rigid perfectly plastic (ideal condition). Moreover, in comparison with analytical approaches, the FE method accounts more realistically for the material properties and boundary conditions and can serve as a guide for analytical models. FEA has been applied to investigate many factors that influence the deformation, including material constitutive behavior (strain hardening or softening, strain-rate sensitivity), die geometry (φ, ψ, moving die) and processing variables (such as friction, backpressure, and thermal condition). Furthermore, analyzing coupled effect of process parameters which affect plastic deformation zone (PDZ) as a crucial factor is neglected in stress analyzed based methods (Li et al., 2004).

In ECAE, the workpiece is subjected to external forces in order to pass die channel abrupt angle to obtain a certain amount of grain refinement. Under the action of these forces, the workpiece undergoes deformation which is measured by strain. Also internal

forces are developed in the workpiece as a result of external forces, which is described by stress as an intensity of these forces. Additionally, stress-strain values depend on geometry and materials of workpiece. This involves solving the following set of governing equations including; strain-displacement relations, stress-strain relations and equation of motion.

FEA of ECAE has been carried out for the die sets with channel angle of 90° and 100° considering the effect of friction (Prangnell et al., 1997). The FEA model has been constructed assuming plane strain condition. To check the validity of FEA model, results were compared to the shape change of a pure aluminum workpiece after partial passage through the die. The results indicated that die channel angle and friction condition significantly affect the deformation behavior of the workpiece in the terms of total EPS and strain inhomogeneity.

A comprehensive FEA was carried out to study the formation of the plastic deformation zone (PDZ) and pressing load requirement regarding punch displacement during a single pass of ECAE for die with channel angle (φ) of 90° (Li et al., 2004). Furthermore, coupled effects of material response, corner angle (ψ=0°, 45° or 90°) and friction were studied in this research. Also, morphology and strain rate sensitivity of PDZ as the two chief characteristics which determine strain inhomogeneity was addressed. The FEA was carried out assuming plane strain condition considering three variables namely, material strain hardening (perfectly plastic and elastic plastic hardening material), die corner angle (ψ=0°, 45° or 90°) and friction coefficient, (μ=0, 0.025, 0.075, 0.1, 0.125 or 0.15). They reported that assuming the strain hardening effect alters the length of dead zone (the head and tail of workpiece). Additionally, with the increase of ψ, the length of dead zone increases notably for elastic-perfectly plastic case but remains almost same for strain hardened case. Also it was shown that, in the steady state region, notable strain inhomogeneity form on the plane perpendicular to the

axis of the workpiece occurred for all cases except for perfectly plastic material with ψ=0°. Strain inhomogeneity increased with ψ in both materials, although this effect is less notable in the case of strain hardening material. Moreover, friction assisted in reducing the free surface gaps that form between a strain hardening material and the die, but further increased the degree of heterogeneity.

Explicit FEA using 2D plane strain condition was carried out in order to address the discrepancy in strain inhomogeneity originated by using die set with different corner angle (ψ). The analyses were performed for die with φ=90° and ψ=0°, 10°, 20° and 28°. The inability of materials to flow in the case of sharp corner angle was resembled by severe mesh deformation at the end of simulation. Also, non-uniform deformation behavior in the outer surface and core of the workpiece were related to different contact condition. Moreover, smaller corner angle (ψ) led to narrower deformation zone (ideal pure shear) and subsequently produced the workpiece with higher strain homogeneity; however, imposed larger stress concentration in the workpiece. The optimal corner angle (ψ) of 10° was reported for processing the workpiece with optimize homogeneity without involving detrimental effects (Nagasekhar & Tick-Hon, 2004).

Deformation heterogeneity of a workpiece during a single pass of ECAE was analyzed by using 3D FE-model assuming that friction coefficient between the workpiece and the channel varies from 0 to 0.15 with an increment of 0.05. They signify that 3D FE-model simulation is more efficient than 2D one for analyzing strain inhomogeneity. Furthermore, it was shown that friction coefficient significantly affects strain homogeneity, whereby the increase of friction coefficient resulted in subsequent increase of the average plastic strain and inhomogeneity index except in the Y-plane (parallel to workpiece axis after extrusion). Also, comparison of the 3D model results with analytical and experimental results indicated a good consistency (Suo et al., 2006).

FEA of ECAE with focus on the effect of coulomb and shear friction models on deformation behavior, strain distribution and punch force signified that the corner angle that the workpiece makes decreases gradually with shear friction but rapidly with coulomb friction model. Moreover, the inhomogeneous deformation measured using the deformation inhomogeneity index (I) based on the width of the workpiece was found to increase gradually with increasing shear friction value but rapidly with coulomb friction model. For a friction value of 0.1, coulomb model predicted a highly inhomogeneous deformation with fold formation. Also it was shown that average strain increases gradually with increasing shear friction but more rapidly with coulomb friction model. The strain inhomogeneity index predicted that homogeneity was attained more rapidly with increasing coulomb friction value but it did not account for the inhomogeneous deformation that happens at high coulomb friction. Regarding punch load results, it was indicated that to deform strain hardening material shear friction model predict higher accuracy rather than coulomb friction model, hence the shear friction model should be used in ECAE simulation (Balasundar & Raghu, 2010).

FEA was performed in order to study the corner gap formation between the die and workpiece during the ECAE process for the strain hardening and quasi-perfect plastic materials by considering plane strain condition (Kim et al., 2000). The mechanism of the formation of die corner gap was explained using the von-Mises stress distribution. Results signify that, large corner gap decreases the average EPS and strain homogeneity in the ECAE-treated workpiece.

2.7. Mechanical properties of ECAE-treated metals

The UFG metals produced by ECAE cannot be produced by conventional thermomechanical treatment (TMT). As a consequence, ECAE-treated metals demonstrate suitable combinations of mechanical properties compared with the CG metals manufactured by conventional TMTs (Azushima et al., 2008). However,

conflicting results were reported for the ductility. While some researchers have reported UFG structure show lower ductility compared with CG structure, several observations have reported improvement in the ductility of the UFG structure processed by ECAE (Valiev et al., 2002).

Large number of researches has been accomplished and reinforces the dependence of grain size and yield flow according to Hall-Petch equation for wide range of metals. In this regard, the effect of ECAE on yield strength, ultimate strength, elongation at breaks and fatigue endurance was vastly investigated. The results of several researches have been summarized in Table 2.1. As can be seen from this table, significant improvement was achieved for ECAE-treated materials, associated with extreme reduction in grain size.

On the other hand, ductility has been decreased as a result ECAE. This reduction in ductility attributed to the decrease in hardening exponent as a consequence of strain accumulation. However, significant improvement in ultimate tensile strength (almost 25-35%) of AA 6xxx series without compromising ductility in compression with their conventional T6-heat treated was reported (Roven et al., 2005). Furthermore, tensile strength to rupture for this series of aluminum alloy is increased by a factor of 1.5 to 2 as a result of ECAE treatment. Additionally, it was shown that mechanical properties of ECAE treated AA 6061 using route B_c in terms of yield stress and ultimate strength considerably increased while the tensile ductility decreases (Chung et al., 2002).

Mg alloys subjected to ECAE demonstrate impressive ductility enhancement, which is supposed to due to specific textures forming by pure shear in hcp materials (Lapovok et al., 2005). Tensile elongation of Mg alloys, ZK60 (Lapovok et al., 2005) and AZ31(Lapovok et al., 2008) after the ECAE processing reach to the superplastic deformation regime.

Table 2.1: Yield strength ($\sigma_{0.2}$), ultimate strength (σ_{UTS}), elongation (δ) and fatigue endurance limit (σ_{f0}) of light alloy processed by ECAE (Estrin & Vinogradov, 2010)

Material	**Processing**	**$\sigma_{0.2}$ (MPa)**	**σ_{UTS} (MPa)**	**δ**	**σ_{f0} (MPa)**
AA 6061	O	150	270	48	40*
	T6	276	310	12	50*
	ST ECAE, 1, 125° C	310	375	20	80*
	ST ECAE $4B_c$, 125° C	380	425	20	<60*
AA 7075	O	105	230	17	
	T6	503	525	9	
	ECAE $2B_c$ + NA 1 Month	650	720	8.4	
AA 2124	T851	455	492	7.2	125**
	T851+ECAE $8B_c$, BP	330	602	7.2	290***
Cu 99.96%	A	140	240	46	65
	ECAE 8B	390	440	22	80
	ECAE $12B_c$	480	520	18	80
Cu 99.95%	A	68	332	45.5	
	ECAE, 1	342	342	8.9	
	ECAE $2B_c$	407	424	8.6	
	ECAE $4B_c$	415	455	8.2	
	ECAE $8B_c$	385	449	8.5	
	ECAE $12B_c$	358	423	8.5	
	ECAE $16B_c$	348	407	10	
Cu 99.98%	ECAE $20B_c$	375	440	15	
Cu 99.99%	ECAE $8B_c$	375	378	N/A	170
Cu-0.36 Cr	ECAE 8A, AG 500° C, 1h	409	427	24	170
	ECAE $8B_c$, AG 500° C, 1h	456	467	20	160
	ECAE 8CA, AG 500° C, 1h	438	454	23	180
Fe 99.95%	A	90	260	54	
	ECAE $4B_c$	696	723	7	
	ECAE 8B	850	980	1	
Fe-0.15 C-0.25 Si-1.1 Mn	ECAE A, 480° C 1h	937	943	11	
	ECAE A, 480° C 24h	805	823	12	
	ECAE A, 480° C 72h	713	733	19	

$\sigma_{0.2}$: Yield stress, σ_{UTS}: Ultimate tensile strength, δ: Elongation at break, σ_{f0}: Fatigue endurance limit (on the basis of 10^7 symmetric push-pull cycles and stress ratio of R=-1, if otherwise not specified), O: as-received annealing, AG: ageing, NA: natural ageing, ST: solution treatment

*: R=0.05

**: Based on 5×10^5 cycles to failure

***: Total strain control test at 2×10^5 cycles to failure

Improvement of both strength and ductility is a challenging task which is crucial for many industrial applications. The first strategy to achieve this goal is to proper selection of chemical composition and specific processing plan, combining the effect of ECAE and pre/post processing such as heat treatment. In this regard, cryodrawing and cryorolling prior to ECAE for tailoring stacking fault energy for high ductility and strength were carried out (Zhao et al., 2006). Results revealed significant enhancement

in strength coupled with improved ductility as a result of simultaneous accumulation of twins and dislocations during tensile test However, it is important to consider an overestimation in the elongation to failure in uniaxial test as a result of using sub-size samples.

Similarly, it was found that the influence of SPD on the ductility of Al alloys may be ambivalent (Altan, 2006). Moreover, according to Table 2.1, it is concluded that pure materials and dilute solutions are more responsive to grain refinement, which provide the possibility of replacing them with their alloys (Estrin & Vinogradov, 2013).

Uniform elongation is another important factor that should be taken under careful consideration. A sharp yield point followed by a plateau, which appeared specifically in stress/strain curve of bcc materials and specifically annealed steels leads to non-uniform plastic deformation, namely Luder band formation (Jafarlou et al., 2014). This non-uniformity does not improve as evident from the stress/strain curves of ECAE treated materials; however, the materials' resistance against localized plastic flow in post-necking regime can notably increase (Estrin & Vinogradov, 2013).

Strength and ductility also govern the fatigue endurance and toughness which are considered as the most important secondary properties. Materials with high strength and sufficient ductility in combination with high fatigue endurance can be considered as ideal materials for industrial application. Materials behavior under cyclic load is conventionally considered at low cycle fatigue (LCF) and high cycle fatigue (HCF) regimes based on the applied strain amplitude. HCF testing corresponds to probing a material's resistance to crack initiation, whereas LCF testing corresponds to assessing the material's tolerance to defects in a regime when fatigue life is controlled by crack propagation (Estrin & Vinogradov, 2010).

Based on the foregoing consideration, a traditional fatigue improvement strategy relies on the following correlation: the higher the strength under monotonic loading, the higher the fatigue life. Proportionality between the tensile strength and fatigue endurance limit for heat treatable and non-heat treatable aluminum alloy is shown in Figure 2.11 (reproduced figure). This is certainly not a firm "law", and the effectiveness of the strategy for improving fatigue properties by raising the ultimate tensile strength depends on the material and the grain refinement process (Estrin & Vinogradov, 2013).

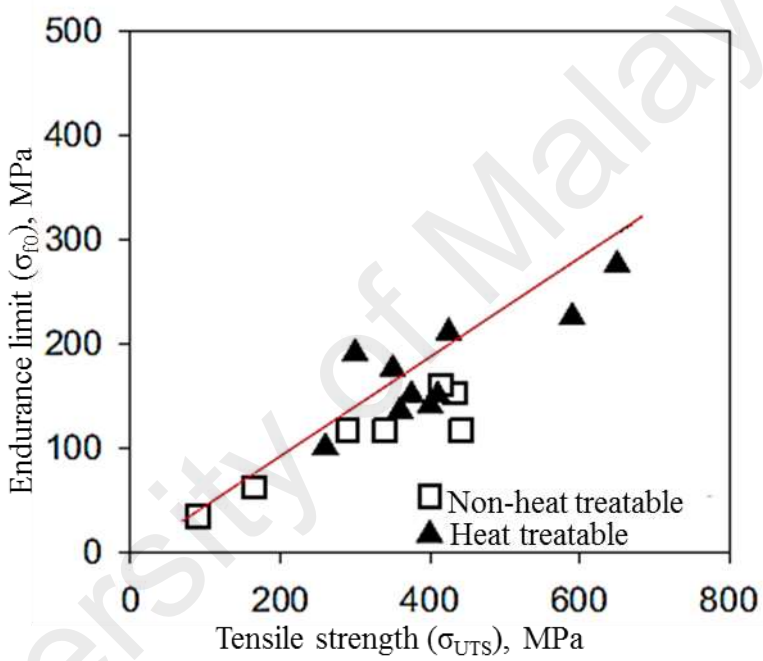

Figure 2.11: Proportionality of tensile strength and fatigue endurance for heat treatable and non-heat treatable aluminum alloy (Estrin & Vinogradov, 2010)

Fatigue tests of light alloy with UFG structure produced by SPD techniques generally demonstrate significant improvement in HCF. However, this improvement is not as notable as the improvement of strength under monotonic loading. Indeed, while for conventional metals the ratio of endurance limit to tensile strength is typically greater than 0.5, the ceiling value of 0.5 has not commonly exceed 0.5 for UFG metals. Furthermore, the results for LCF regime are worse which UFG metals and alloys are consistently inferior in their ability to sustain cyclic loads regardless of SPD technique. The inferior LCF performance of UFG metals can be addressed by greater availability

of grain boundaries in orientations favorable for crack propagation in metal with UFG structure (Estrin & Vinogradov, 2010).

In LCF testing under constant total or plastic strain amplitude, the cyclic response exhibits remarkable variations in the stress amplitude depending on the type of slip and the purity of the material. Beside the different stress amplitude levels, a distinctly different cyclic hardening/softening behavior is observed for various aluminum alloys. It has long been recognized that the microstructure of high purity metals produced by SPD is inherently unstable and is prone to recovery and grain coarsening at low homologous temperatures, e.g. at room temperature, even in the absence of loading (Skrotzki et al., 2007).

In this regard relatively pure single phase fcc aluminum with UFG structure, under cyclic deformation softening behavior (i.e. a decrease of stress amplitude with the number of cycles or the cumulative strain for a given strain amplitude) was observed. This phenomenon in pure metals is usually addressed by the ease of dislocation annihilation and is inherited from plastic pre-staining regardless of how severe it was. A mechanism of cyclic softening associated with dynamic grain coarsening, which is specific to SPD processed metals (Höppel et al., 2006).

Single-phase Al-Mg alloy AA 5056 show some slight cyclic softening under much higher stress amplitudes than those observed for commercial purity (CP) Al. As grain (dislocation cell) coarsening in this AA 5056 alloy is not pronounced, cyclic softening is attributed primarily to the dislocation recovery. In the precipitation hardenable Al-Mg-Sc alloys, the numerous precipitates stabilize the structure decisively, so that it remains ultrafine- or fine-grained during annealing for 1 h at temperatures up to 400 °C. No grain coarsening was observed after low- or high-cycle fatigue of this alloy (Cavaliere & Cabibbo, 2008). Increasing amount of Mg results in greater tensile

strength and higher level of cyclic stress amplitude, while increasing processing temperature leads to formation of fine, rather than UFG structure exhibiting considerable cyclic hardening due to ordinary dislocation accumulation (Estrin & Vinogradov, 2010).

Higher stress levels, lower ductility and susceptibility to strain localization in macroscopic shear bands in UFG Al and Al-alloys, result in reduced LCF life as compared to those of fully annealed reference alloys. Nevertheless, the LCF properties can be considerably improved by post-ECAE annealing at moderate temperatures, which reduces the initial dislocation density, the internal stresses and the number of stress risers and also leads to relaxation of stressed grain boundaries. In particular, it was suggested that by producing a bi-modal grain structures with co-existing populations of small and large grains, a favorable combination of strength and ductility may be achieved, which also promotes improved fatigue performance. This can, indeed, apply to LCF due to higher ductility associated with the presence of coarse grains. Indeed, coarse grains yield at lower stresses than the rest of the polycrystal, thereby providing a natural pathway for early strain localization and premature failure either due to cracking at the interfaces between the coarse grains and the surrounding fine-grain matrix or due to transgranular surface crack initiation in a coarse shear band (Estrin & Vinogradov, 2010).

It was shown that, the cyclic response at LCF and HCF strongly depend on the composition for both cases of heat treatable and non-heat treatable aluminum alloys: the higher the degree of alloying, the stronger response in terms of stress amplitude for a given strain amplitude. The same trend is seen in high-cycle regime increasing Mg content in Al-alloys results in longer fatigue life for the same stress amplitude (May et al., 2007).

The results for Al alloys pressed to a small number of passes (1 or 2) suggest that processing to moderate, rather than excessively high, strains may offer an attractive trade-off between the processing cost and energy efficiency and improvement of fatigue properties, particularly if HCF is of primary concern. The judicious choice of processing parameters, such as temperature, strain rate and back pressure, and the initial state of the material becomes decisive for ensuring the ultimate performance after reasonably moderate straining (Chung et al., 2002).

A notable improvement was observed in fatigue life of single pass treated AA6061 by a factor of almost 10 compared to a T6 treated one. This result is significant since the improvement was obtained in both LCF and HCF regimes. However, of subsequent passes (for passes) this advantage disappeared especially in the HCF regime. The discrepancy in fatigue life between the single passed and multi-passed treated AA 6061 was correlated to the difference in grain boundary angle believed to affect the resistance of micro-crack nucleation during cyclic loading. Therefore, it was concluded that when a balance between high strength and fatigue endurance is an important design factor a single passed alloy can be an optimum selection (Chung et al., 2002).

2.8. Research gap and aim of the present work

The review of research works indicates that mechanical and fatigue properties of many different types of pure metals and alloys which are processed by ECAE have been evaluated. However, there are few reports on mechanical properties, fatigue and fretting fatigue behaviour of AA 6063. Due to the vast application of AA 6063 in different fields of the industry it is necessary to analyse these aforementioned properties. Additionally, the influence of heat treatment, hard anodizing and the combination of these two processes on mechanical, fatigue and fretting fatigue properties of ECAE treated AA 6063 can give an insight for further enhancement of this alloy for industrial application. Therefore, by considering this gap the following aim is considered:

Evaluation of mechanical, fatigue and fretting fatigue properties of AA 6063 processed by ECAE.

According to literature, tubular metallic components with improved mechanical properties are crucial in different fields of industry. Several techniques have been proposed for SPD treatment of tubular components; however, the complexity of these processes and short length of the tube are limiting their industrial application. By considering these limitations, the second aim of this research was considered as; Development of ECAE for SPD treatment of tubular components.

The study of ECAE indicated that significant amount of shear stress is imposed to the workpiece onset of passing the die abrupt angle. This amount of stress is in the range of many solid state plastic joining processes. On the other hand joining rod shape and cylindrical components is challenging issue due to the small common interface. In this regard joining AA 6061 and mild steel SAE 1018 is considered due to the promising combination of mechanical properties and difficulty of joining these two materials indicates in several researches. By considering these issues and high capability of ECAE to impose ultra-large stress to the workpiece and also wide industrial application of light weight material, the third aim of this research sets up as: Development of ECAE for solid state joining of tubular AA 6061 and cylindrical mild steel SAE 1018.

CHAPTER THREE: RESEARCH METHODOLOGY

3.1. Introduction

This chapter has been organized to provide a detailed account of evaluation of the mechanical properties of AA 6063-O (section 3.2), ECAE treatment of tubular AA 6061-O (section 3.3) and the application of ECAE to join AA 6061-O and SAE 1018 mild steel (section 3.4) as illustrated in Figure 3.1.

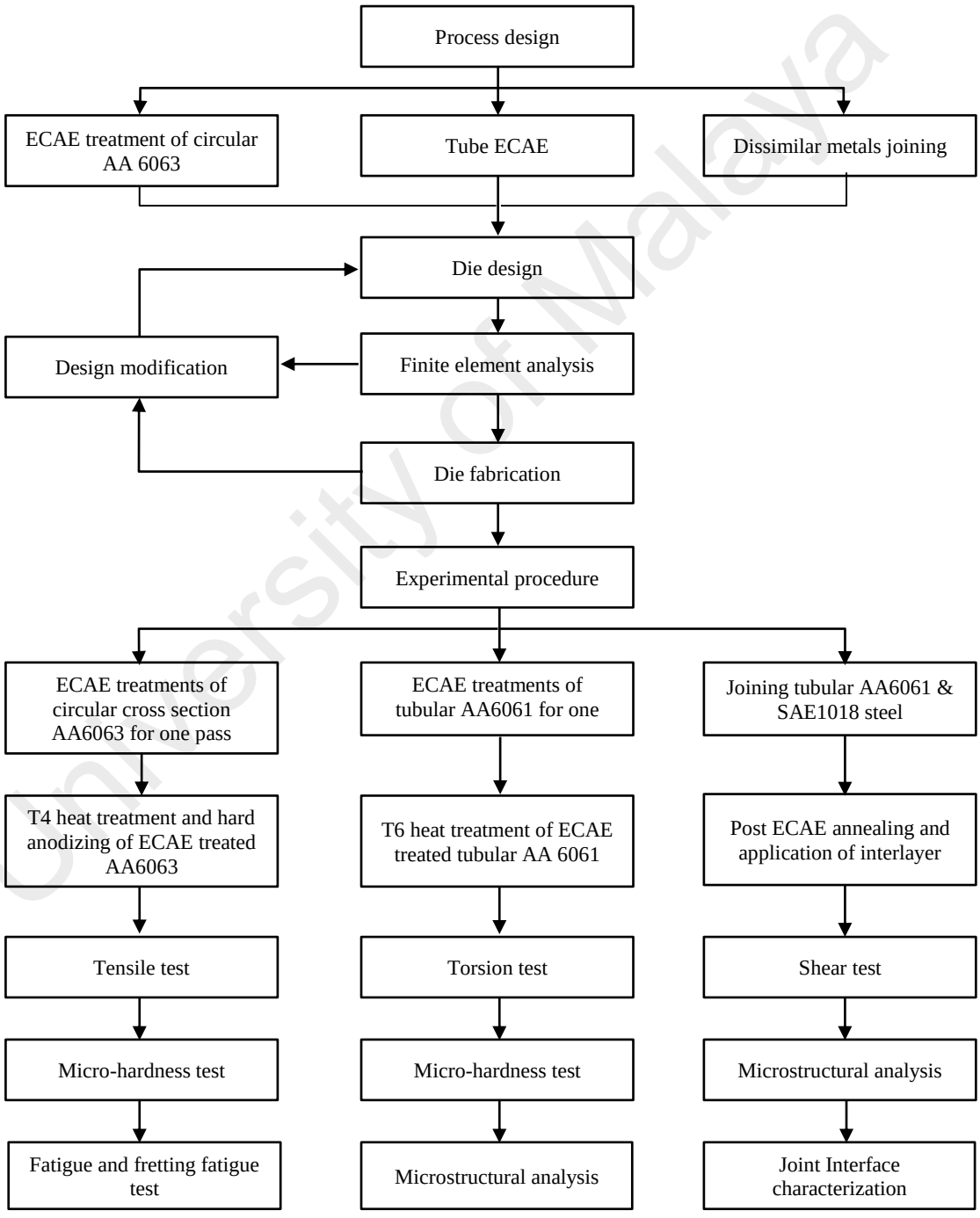

Figure 3.1: Flowchart of the current research

3.2. Evaluation of the mechanical properties of ECAE-treated AA 6063-O

Aluminum alloy 6063 (AA 6063) is widely used in different industrial fields, such as construction and transportation due to acceptable formability, proper weld ability and corrosion resistance. However, the mechanical properties of this alloy, such as hardness, tensile strength, fatigue life and fretting fatigue behavior are not appreciable (Miller et al., 2000).

Fretting is a contact damage process that occurs when fatigue load is imposed on a component while it is in contact with an adjacent component. This phenomenon leads to oscillatory micro-slipping at the components' surfaces, which actuates existing crack nucleation and eventually leads to unanticipated structure failure (Heredia et al., 2014).

A traditional fretting fatigue improvement strategy is coating as a surface modification method in industrial applications wherever contact parts are subjected to small amplitude-relative motion as a result of vibration or cyclic loads. The effects of hard and soft coating on fretting fatigue behavior have been studied broadly (Rajasekaran et al., 2008). In order to reduce the detrimental effect of fretting fatigue, hard anodizing (HA) is extensively applied in industry as an efficient coating technique. Besides, HA significantly increases surface hardness and corrosion resistance while simultaneously serving decorative purposes (Bouchama et al., 2013).

Non-age-hardenable Aluminum alloys including AA 5xxx are not responsive to the SPD process in terms of fatigue life (Patlan et al., 2001). On the other hand, grain refinement, tensile strength, ductility and surface hardness enhancement and also improvement of fatigue life for age hardenable aluminum alloy such as AA 6xxx series are efficiently obtained by the SPD process (Cavaliere & Cabibbo, 2008; Vinogradov et al., 2003).

For prospective engineering applications of AA 6063, the resistance under small-amplitude oscillatory motion potentially occurring between mating surface subjected to

vibration or cyclic loads in combination with fretting fatigue (cyclic bulk fatigue load) needs to be considered along with tensile strength and ductility under monotonic load (Blanchard et al., 1991).

The objective of this section is to evaluate the influence of ECAE, HT and HA on the mechanical properties of AA 6063. ECAE was used in this research to produce an UFG structure. Subsequently, the processed parts were heat-treated and anodized, and finally, the plain and fretting fatigue lives of coated and uncoated samples with UFG were investigated.

3.2.1. Base material and Experimental details

The experiments were conducted using commercial AA 6063 having chemical composition and mechanical properties as tabulated in Table 3.1. The mechanical properties of AA 6063-O were obtained experimentally by conducting a number of tensile tests in accordance with ASTM standard E8/E8M-11 (E8/E8M–11, 2011).

Table 3.1: Chemical composition and mechanical properties of as-received AA 6063-O

Chemical composition (wt %)							**Mechanical Properties**				
Al	Mg	Si	Fe	Mn	Zn	Cu	σ_y (MPa)	σ_{uts} (MPa)	E (GPa)	υ	ε_{uts}
Balance	0.49	0.45	0.2	0.05	0.02	0.01	34.2	72.7	65	0.33	11.3

The influences of heat treatment (HT) and hard-anodized coating on mechanical properties, and fatigue and fretting fatigue behavior of the ECAE treated AA 6063-O have been investigated in this section. In this regard, five sample types were prepared for experimental investigation. Sample types and related nomenclature used in this investigation are summarized in Table 3.2.

Table 3.2: Details of processes used in the current study with corresponding nomenclatures

Sample	Process	Process nomenclature
1	Raw material	As-received
2	Heat treatment	HT
3	Equal channel angular extrusion	ECAE
4	Equal channel extrusion and heat treatment	ECAE+HT
5	Equal channel angular extrusion, heat treatment and hard anodizing	ECAE+HT+HA

3.2.2. The ECAE processing and heat treatment

The ECAE process was carried out using a die set fabricated with H13 tool steel, heat treated to hardness of 60 HRC and machined with surface roughness of 0.8 μm. Figure 3.2 demonstrates the schematic diagram of ECAE die set, where φ is the die channel angle equal to 90° and corner angle (ψ) of 25° which were confirmed by FEA in advance. ECAE workpieces were cut from the AA 6063-O rod with a length of 110 mm and a diameter of 10 mm along the extrusion direction of the as-received rods.

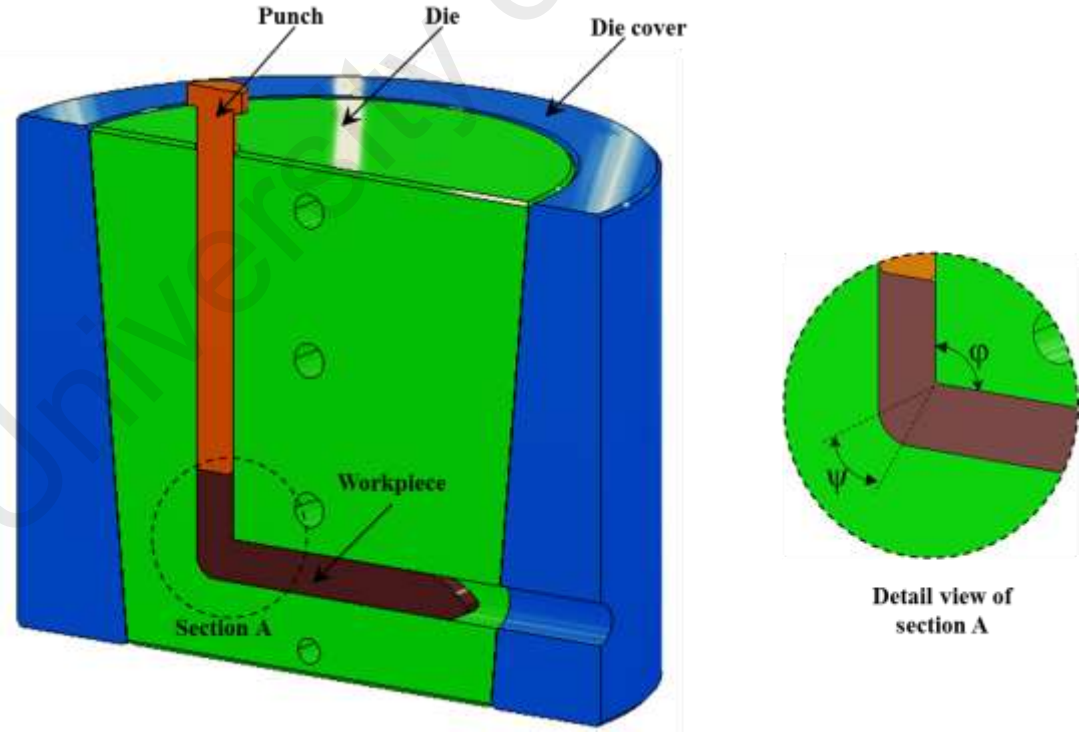

Figure 3.2: Pictorial drawing of equal channel angular extrusion (ECAE)

Influence of internal heating during ECAE process was investigated by (Pei et al., 2003). Their results indicated that for pressing speeds of 0.18, 1.8, and 18 mm s^{-1} temperature rises of about 1, 45 and 75 K (1, 45 and 75 °C) occur in aluminum alloy workpieces, respectively. The ECAE process in this research was carried out at room temperature under constant pressing speed of 2 mm s^{-1} which considerably minimizes heat generation during deformation. Furthermore, die and workpiece surfaces were lubricated using MoS_2, to minimize the frictional effects on contact surfaces. One pass of ECAE was considered for all samples since the maximum increase of ultimate tensile stress occurs in the first cycle (Azushima et al., 2008). Figure 3.3 shows fabricated die and experimental set up. The pressing was carried out using 100 kN Instron press 4469 according to aforementioned set up.

T4 heat-treatment conditions were considered for the as-received and ECAE treated workpieces. In T4 process, the samples were solution treated at 793 K (520° C) for 1 hour and instantaneously quenched by water.

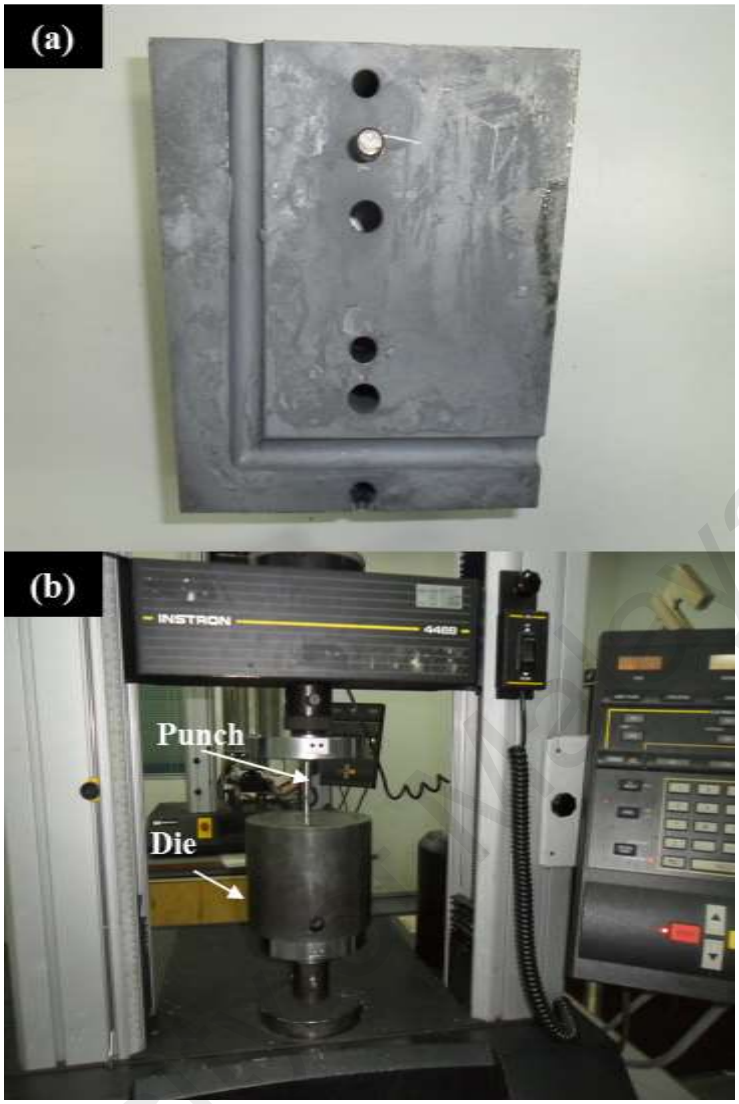

Figure 3.3: (a) ECAE die set and (b) initial configuration of tool set

3.2.3. Sample preparation for plain and fretting fatigue testing

Following the ECAE process, all workpieces were machined in accordance with the ISO 1143:2010(E) standard at an initial surface roughness of $R_a = 0.6 \pm 0.1\ \mu m$ by CNC lathe turning machine to study the plain and fretting fatigue lives (ASM, 2010). All workpieces were subsequently polished with 800/2400 grit silicon carbide paper. Dimensions of the fatigue and fretting fatigue workpiece are shown in Figure 3.4.

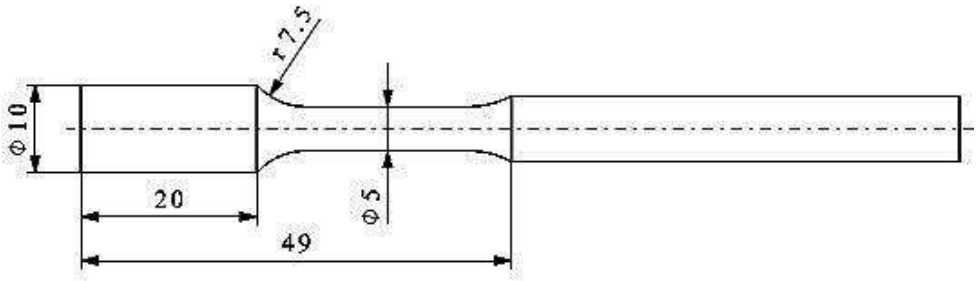

Figure 3.4: Geometry of the fatigue and fretting fatigue specimen according to ISO 1143:2010(E)

3.2.4. Hard anodizing procedure

The hard anodizing process is similar to conventional sulfuric anodizing, except it is done at reduced temperatures, higher unit amperage, and higher final voltage. The oxide layer (Al_2O_3) is the same as that formed in other anodizing processes, with the distinction being that it is much thicker than any hitherto obtainable.

Initially, samples surface preparation included cleaning to eliminate surface contamination. In the first stage, minor surface imperfections and remaining lubricant particles were removed with hot sodium hydroxide solution (temperature of 60° and 25 weight %). Eventually concentrated aqueous mixture of nitric (0.5 weight %) and phosphate acids (0.5 weight %) was used to smooth the samples surface. A near-mirror surface was obtained by this solution. Subsequent to surface cleaning, the workpieces were suspended in electrolytic bath (sulfuric acid diluted by distilled water) as an anode and direct current was passed through the bath therefore oxygen and hydrogen were produced at the anode surface (workpiece) and cathode (graphite) respectively. As a result of this chemical reaction a layer of alumina (Al_2O_3) was created on the surface of workpieces. The anodizing operating parameters are tabulated in Table 3.3.

Table 3.3: Hard anodizing operating parameters

Electrolyte	Temperature (°C)	Current density (A/dm^2)	Voltage (V)	Time (min)
Sulfuric acid (**15**% weight)	0	2	30	30

The oxygen reacted with the anode (workpiece) to form a durable and abrasion resistant thin aluminum oxide (Al_2O_3) layer, while hydrogen was simultaneously produced at the cathode. The HA process produced a uniform, dense and significantly hard oxide layer (coating) on the workpiece surface compared with a natural oxide layer. A schematic of the hard anodizing process is depicted in Figure 3.5.

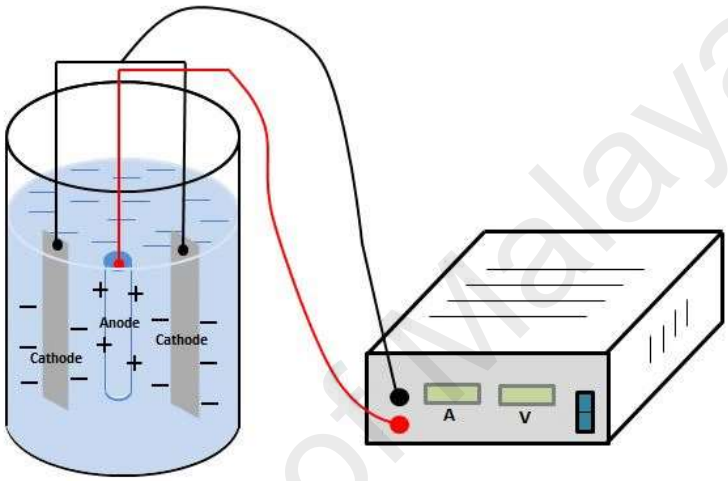

Figure 3.5: Schematic diagram of the hard anodizing process

3.2.5. Fretting fatigue test

In order to examine plain and fretting fatigue lives of samples (Table 3.2), three samples for each loading cases were prepared according to Figure 3.4. It worth mentioning that the heat treatment hard anodizing processes have been accomplished after machining of samples according to Figure 3.4. A fatigue test specimen was gripped by the chuck and bearing, and loaded rotationally in the in-house developed rotating bending test machine (Neu, 2011). The contact force between the workpiece and contact pads was adjusted by application of the fretting ring's screw using torque wrench.

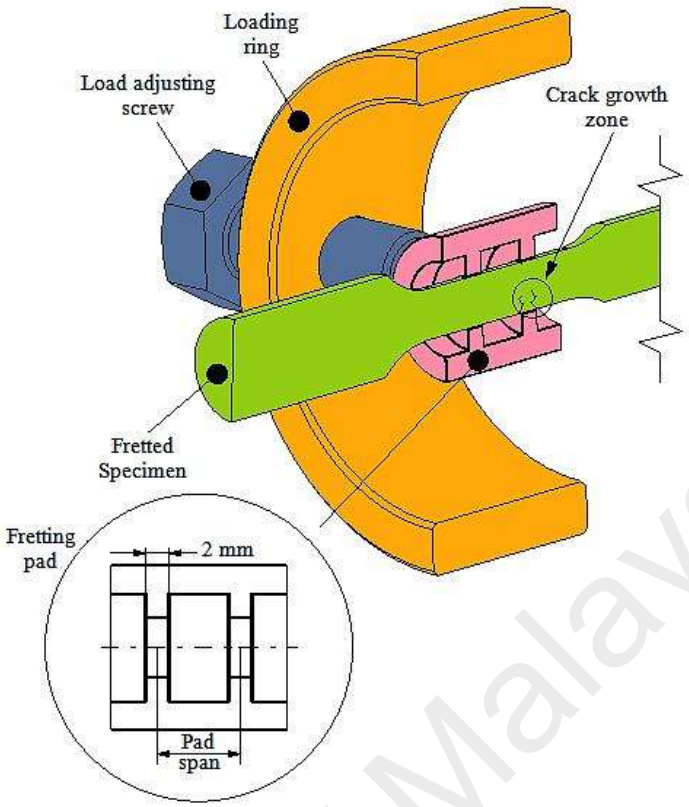

Figure 3.6: Assembly of fretted specimen with rotating bending fretting fatigue machine

An AISI 4140 steel flat bar with 300 HV hardness, ultimate tensile strength (σ_{uts}) of 700 MPa and yield stress (σ_y) of 420 MPa was used to fabricate the fretting fatigue pads. The specimen material is softer than the pads but the hard-anodized coatings (310HV) are harder than pads. To simulate the fretting fatigue condition, bridge-type friction pads and a ring-shaped load cell were designed and constructed. The schematic of the fretting fatigue test ring and friction pads is depicted in Figure 3.6. The fretting fatigue test apparatus was applied at a frequency of 50 Hz and constant contact pressure of 100 MPa at room temperature to attain S/N curves. The nominal maximum cyclic stress was set at a value expected to result in fatigue life between 10^4 and 10^7 cycles. Endurance limit of 1×10^7 cycles was considered for current test according to (Almaraz et al., 2012; Estrin & Vinogradov, 2010). The stress required to produce fretting was transmitted to the contact area via a calibrated proving ring as schematically illustrated in Figure 3.6 through the loading pads. Two bases (contacting surfaces) were considered for each

loading pads, through which the load was imposed onto the sample. The pad span (distance between the centers of the fretting pad's feet) was selected of 6.8 mm. The pad's base width was 2 mm. The loading pads revolved accompanied by the workpiece, and this simulates the fretting fatigue conditions between the workpiece and pads.

Normal force was imposed onto the sample by an adjustable screw and was measured by a load cell. The frictional force created by this normal force had to be calibrated before testing. In order to calibrate the testing load, two strain gages in the direction of friction and another two strain gages at a right angle to this direction, were attached to the pads and wired to create a Wheatstone bridge circuit to measure the elastic strain induced by frictional force. This configuration of strain gages cancels out the effects of rising temperature due to the friction at the contact surfaces. Figure 3.7 shows the force-displacement calibration curve for the present research. This curve was obtained by repetition of several load cases in order to calibrate the frictional force versus displacement.

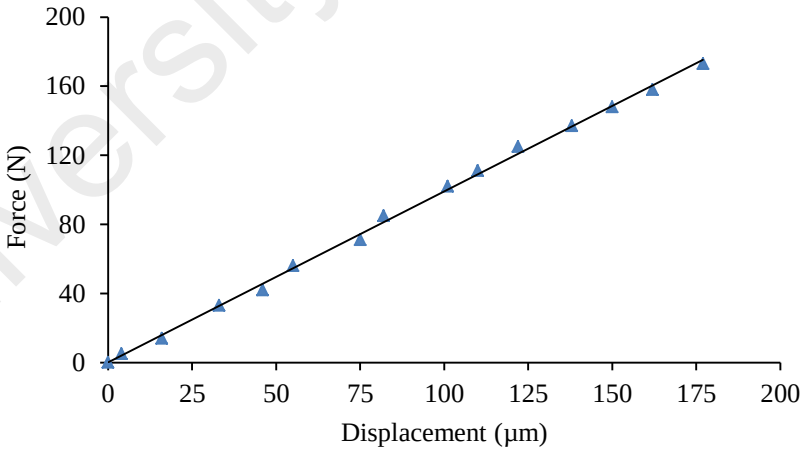

Figure 3.7: Force-displacement calibration curve for the friction pads' load cell

3.3. ECAE treatment of tubular components

Due to the vast application of lightweight tubular metallic alloys in many branches of engineering such as aircraft, automotive, cooling towers, pressure vessels, pipelines and offshore platforms production of tubular with efficient mechanical properties is

indispensable. In this regard, the objective of this section of thesis is to develop the ECAE process for the SPD of aluminum alloy.

3.3.1. The principle of tube-ECAE

A new method based on ECAE was developed for grain refinement of tubular metallic components. The principle of tube-ECAE, illustrated in Figure 3.8(a) is based on the process of pressing a tubular workpiece through a die with a channel angle of $\varphi=120°$ and a corner angle of $\psi=22°$. The outer surface of the tube is constrained by the channel surface of the die and the tube inner cavity is filled with hydraulic oil to prevent sample failure during processing.

In order to preserve and prevent hydraulic oil leakage within the cavity, the two inner tube ends were threaded, and a screw was fastened to one end of the tube with sealing tape. Finally, the workpiece cavity was completely filled with hydraulic oil and subsequently sealed by fastening with the second screw. Schematic representations of the initial workpiece are illustrated in Figure 3.8(b).

A severe shear was imposed to the tubular workpiece during extrusion through the point of intersection between two parts of the die channel. A large quantity of plastic strain accumulated in the workpiece as a result of the ultra-large shear stress. The deformation mode in this process was a simple shear, controlled by the die corner (ψ) and channel (φ) angles. According to the principle of processing and incompressibility of the applied hydraulic oil, the process precisely resembled conventional ECAE.

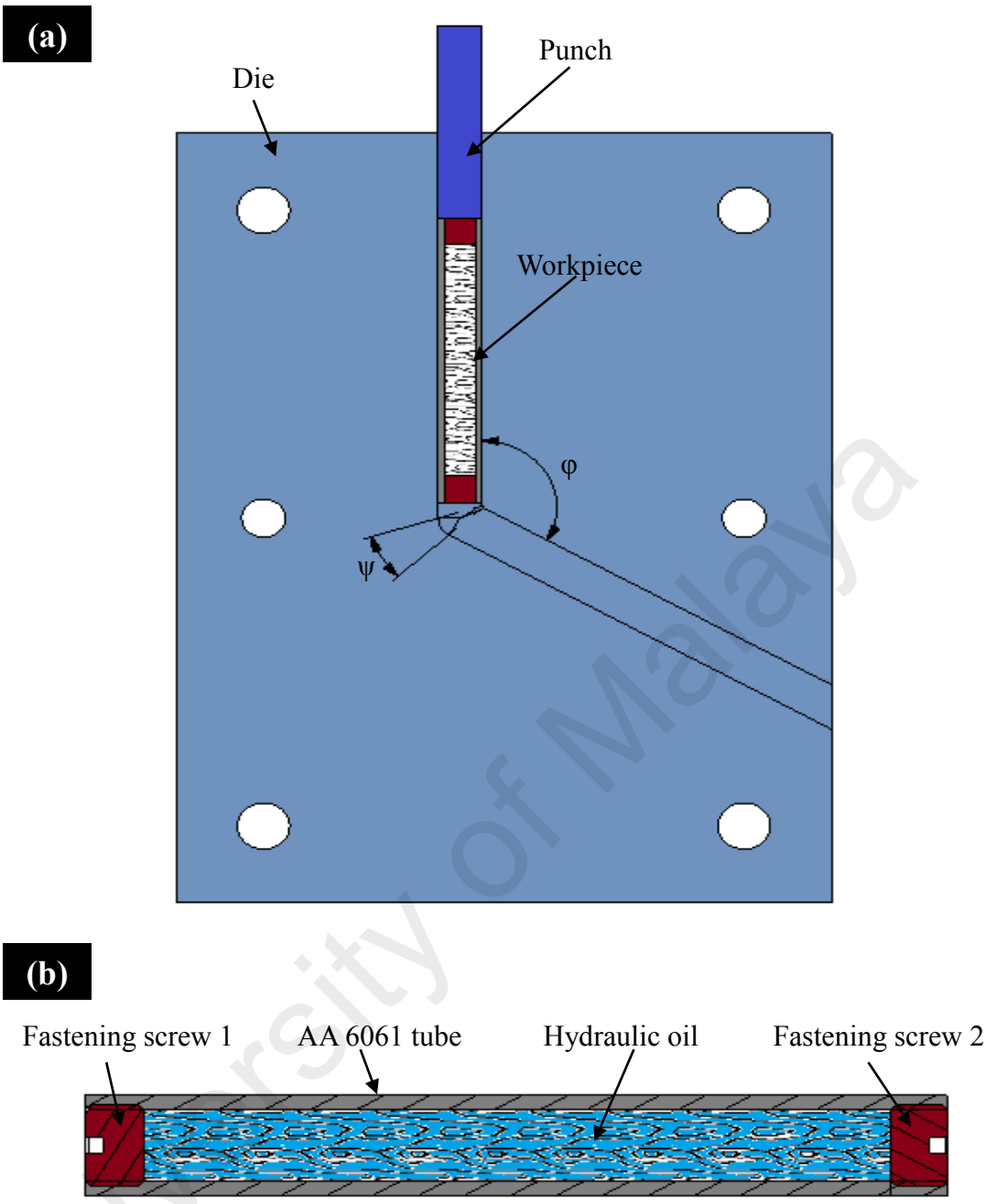

Figure 3.8: Schematic illustration of (a) the tube-ECAE principle and (b) the assembly of the initial workpiece

3.3.2. Base materials

The 6061-O aluminum alloy (wt. %: 95.85 Al, 1.2 Mg, 0.75 Si, 0.6 Fe, 0.4 Cu, 0.15 Mn, other elements <balance>) was used as the test material in this section. Due to the exceptional mechanical and metallurgical properties of this grade of aluminum alloy, including good weldability, proper affinity to various coatings, workability, and high corrosion resistance, AA 6061-O has been extensively utilized in various industrial

applications such as: construction (couplers, connectors, appliance fittings, and hinge pins), transportation (aircraft, marine, automotive fittings, brake pistons, hydraulic pistons), and electronics industries (electrical fittings and connectors). Furthermore, heat treatment hardening methods such as T6, T7, and T8 are also available for this grade of aluminum alloy (Heinz et al., 2000; Miller et al., 2000; Ozturk et al., 2010).

Component mechanical properties, including yield stress (σ_y) , ultimate tensile strength (σ_u), Young modulus (E), strain at peak stress (ε_u), Poisson's ratio (υ), work hardening exponent (n), and strength coefficient (k) were determined by conducting a number of tensile tests in accordance with ASTM standard E8/E8M-11 (E8/E8M–11, 2011). The measured elastic-plastic properties of AA6061-O are listed in Table 3.4.

Table 3.4: Elastic-plastic properties of AA 6061-O

Mechanical properties	σ_y (**MPa**)	σ_u (**MPa**)	E (GPa)	ε_u	υ	n	k (MPa)
Measured value	55	125	70	0.27	0.33	0.2	105

3.3.3. Tube-ECAE processing and heat treatment

The die set with a 10 mm internal channel diameter was machined (final surface roughness of 0.8 μm) with a 120° channel angle and a 22° corner angle from bulk H13 tool steel, which was heat treated to achieve a hardness value of 610 HV.

Segmented AA 6061-O tubes (75 mm length) filled with SAE 30 hydraulic oil were fed through a die channel into the die's abrupt angle using a punch coupled to a 100 kN press at 1 mm·s^{-1} at room temperature to minimize heat generation effects during deformation. Furthermore, the die channel and aluminum alloy tube surfaces were lubricated with molybdenum disulfide (MoS_2) to minimize contact surface friction effects. Figure 3.9 reveals the fabricated tool set and ECAE initial set up on Instron press 4469.

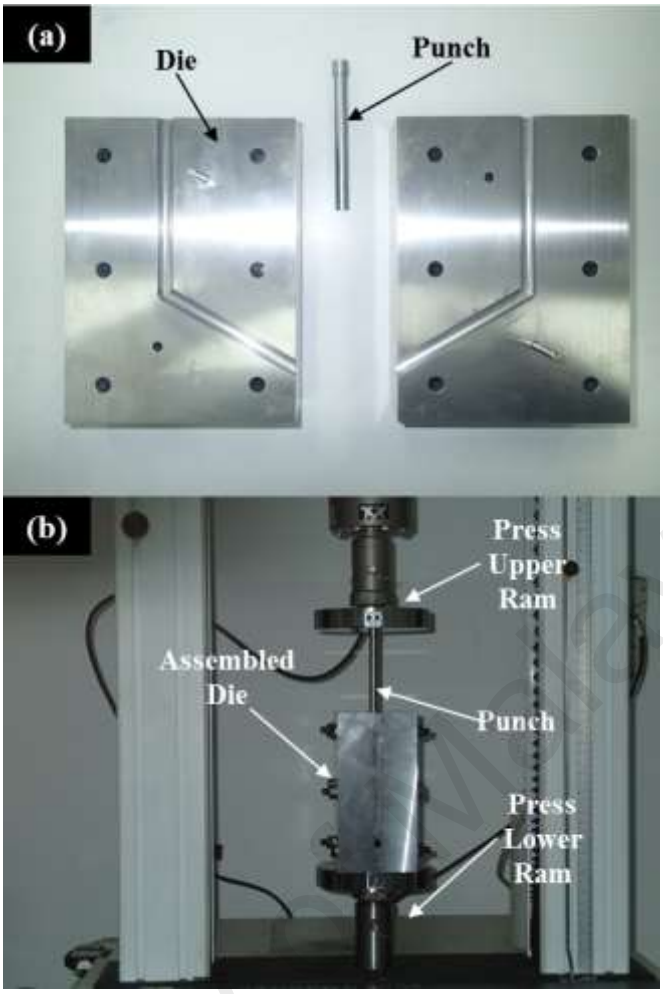

Figure 3.9: (a) Fabricated tool set and (b) initial ECAE set up

In order to determine the effects of heat treatment, ECAE-treated workpieces were heat treated through the T6 procedure. For the T6 process, samples were solution treated at 520 °C for 1 hour and instantaneously quenched with water. The workpieces were artificially aged at 170 °C for 8 hours.

Influence of ECAE and double treatment, including ECAE and T6 heat treatment, on the microstructure evolution and mechanical properties of ECAE-treated tubular AA 6061-O were investigated. Therefore, three sample types (Table 3.5) were prepared for the experimental investigation.

Table 3.5: Workpiece types and their corresponding nomenclature

Sample	Process	Process nomenclature
1	Raw material	As-received
2	Equal channel angular extrusion	ECAE
3	Equal channel angular extrusion and heat treatment	ECAE+HT

3.4. The application of ECAE to join dissimilar metals

In the present section, the ECAE process is employed to join dissimilar metals. In the first stage, the principle of a newly developed process was designed. Afterwards, experiments are carried out in order to join tubular AA 6061 components with SAE 1018 steel rods. Moreover, the influence of a 60Ag-30Cu-10Sn interlayer in addition to a post-ECAE annealing process on joint quality is studied.

3.4.1. The principle of ECAE joining

ECAE joining, as an incremental shearing process, was employed in this research to join aluminum alloy and steel parts through imposing very high strain and no change in the cross-sectional dimensions of the parts to be joined. As illustrated in Figure 3.10, the principle of ECAE joining is based on pressing the mating materials through the bent zone of a die set channel using a punch. The die set consists of two hollow cylindrical channels with equal cross section diameters of 10 mm, which are coupled through a bent zone at $\varphi = 90°$ and $\psi = 25°$ angles known as channel angle and corner angle, respectively.

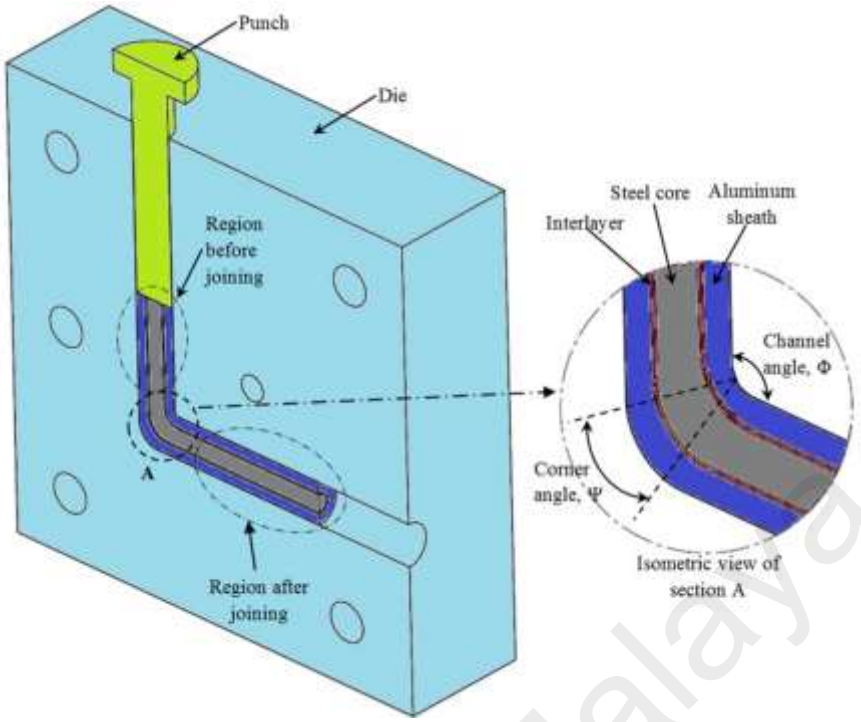

Figure 3.10: Schematic illustration of the ECAE joining principle

3.4.2. ECAE joining process and heat treatment

Prior to ECAE joining, the materials were cleaned in order to remove surface contamination and any remaining lubricant. Two joining configurations (with and without interlayer) were considered: 1) the steel core was assembled into the aluminum sheath without an interlayer, and 2) the workpiece had an interlayer, in which the interlayer foil was rolled around the steel core and embedded into the aluminum alloy sheath.

Prior to inserting the workpiece into the die channel inlet, the outer surface of the aluminum alloy sheath as well as the internal surface of the die channel were sprayed with solid lubricant (MoS_2) in order to reduce friction effects. After that, ECAE joining was carried out for one pass at room temperature by pressing the workpiece into the channel using a 100 kN Instron press at pressing speed of 3 mm/s.

Furthermore, to investigate the post-ECAE annealing effects on the joints' metallurgy and strength, the workpieces, including those joined without an interlayer as well as

with an interlayer, was subjected to annealing at 220, 320, 420 and 520 °C for 60 min. Annealing was performed in a chamber furnace by exposing the workpieces directly to the abovementioned temperatures. In order to minimize the detrimental effect of residual stress during cooling period, which may lead to crack formation at joint interface, the samples were quenched at average rate of ~ 20 °C/s.

3.4.3. Base materials

The base materials utilized in the current study are commercial mild steel (SAE 1018) and pre-tempered aluminum alloy (6061-O). The steel components were provided in the form of cylindrical bars with diameter and length of 4.75 and 70 mm, respectively, to be used as the inner assembly part (core). The aluminum alloy parts were supplied in hollow tubular shape with diameter, length and wall thickness of 10, 70 and 2.5 mm, respectively, and these formed the outer part (sheath) of the assembly. Besides, 60Ag-30Cu-10Sn interlayer foil (hereafter AgCuSn) 0.1 mm thick served as interlayer in the current study. The chemical compositions (in weight %) of the base metals and interlayer are given in Table 3.6.

Table 3.6: Chemical composition of materials (Wt. %)

Component	Material	Composition
Sheath (Tube)	AA 6061-O	Balance Al, 0.8% Mg, 0.4% Si, 0.25% Cu, Max 0.15% Mn, Max 0.7% Fe
Core (Rod)	SAE 1018	Balance Fe, 0.18 % C, 0.15% Si, 0.6 Mn, Max 0.04% P, Max 0.05% S
Interlayer	60Ag- 30Cu-10Sn	60% Ag, 30% Cu, 10% Sn

The mechanical properties of the base materials were determined by conducting a number of tensile tests in accordance with ASTM standard E8/E8M-11 (E8/E8M–11, 2011) using Instron 4469 tensile strength tester equipment. The components' measured mechanical properties, including yield stress (σ_y), ultimate tensile strength (σ_u), Young's modulus (E), strain at peak stress (ε_u), Poisson's ratio (υ), strength coefficient (k) and work hardening exponent (n) are given in Table 3.7.

Table 3.7: Mechanical properties of the materials used in the process

Material	Mechanical properties						
	σ_y *(MPa)*	σ_u *(MPa)*	*E (GPa)*	ε_u	υ	*n*	*k (MPa)*
AA 6061-O	56	125	70	0.25	0.33	0.2	205
SAE 1018	210	330	210	0.22	0.3	0.26	530
60Ag- 30Cu-10Sn	120	180	150	0.32	0.34	0.34	580

3.4.4. Interlayer selection and joinability

The interlayer selected for the current study is a 60Ag-30Cu-10Sn foil with a solidus-liquidus range of 602-718^{0}C. Compared with the Sn-rich Sn-Ag-Cu tertiary system that has mainly been applied in the electronics industry, the 60Ag-30Cu-10Sn alloy demonstrates better mechanical properties particularly at higher temperatures (Wiese & Wolter, 2007). The existence of copper in the matrix of this interlayer causes the formation of nanoscale Cu intermetallic precipitates, which can impede dislocation movement and lead to significant enhancement in the alloy's strength (Wiese & Wolter, 2007). Furthermore, copper is able to increase the wettability of aluminum through decreasing its surface tension, particularly at higher temperatures, therefore improving the cohesion between the interlayer and adjacent aluminum alloy (Ghosh et al., 2009).

Besides, the promising compatibility of silver with aluminum has been proven in previous studies, although the formation of $AlAg_2$ and $AlAg_3$ intermetallic phases is reportedly a main drawback at high temperatures (Bhanumurthy et al., 2006). Therefore, the annealing temperature was kept below the liquids threshold of aluminum alloy during post-ECAE heat treatment to avoid the excessive formation of such intermetallics. On the other hand, as silver and iron are metallurgically incompatible, the presence of copper in the interlayer matrix can enhance the joinability of the interlayer to steel, particularly by considering the fact that copper and silver are quite compatible with each other and do not form any intermetallic compound (Bhanumurthy

et al., 2006).

Finally, the presence of a small portion of tin element with a relatively lower melting point compared with other interlayer constituents can promote the wettability and the cohesion of the interlayer to both mating materials upon reaching annealing temperature. In addition, the low percentage of tin decreases the possibility of the age-softening phenomenon occurring, during which tin-rich crystals and Ag_3Sn particles tend to grow particularly at higher temperatures (Ghosh et al., 2009).

The microstructure of the 60Ag-30Cu-10Sn interlayer along with the distribution of its elements is shown in Figure 3.11. As observed in the figure, the interlayer microstructure includes dark Cu-rich regions with needle-like morphology dispersed throughout the Ag and Sn matrix.

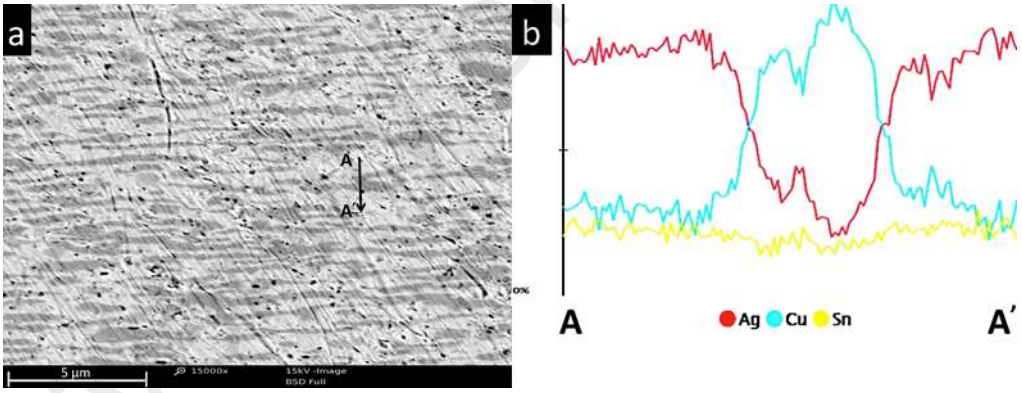

Figure 3.11: Overview of the 60Ag-30Cu-10Sn interlayer including its (a) microstructure and (b) chemical analysis that shows the distribution of constituent elements

3.5. Sample preparation for mechanical and metallurgical analyses

In order to prepare the workpieces to determine mechanical properties including yield strength, ultimate strength and ductility the procedure according to ASTM standard E8/E8M-11 (E8/E8M–11, 2011) was followed and tests have been carried out using Instron press 4469.

Vickers microhardness tests with an applied load and duration of 9.8 N and 10 seconds, respectively, were performed according to the ASTM E384-11e1 (E384-11e1, 2011) on plane perpendicular to workpiece axis cross sections via "Mitutoyo AVK-C200" equipment. The mean hardness for each workpiece was obtained from 2 different indentation lines across the workpiece cross sections. During hardness tests, to avoid interference with work-hardened regions of previous indentations, an offset of 2.5 times the indentation diagonal was accounted for between two successive hardness tests. Based on the length of the indentation diagonal measured under the optical microscope in addition to the applied load, the following equation was employed to evaluate the Vickers hardness (HV):

$$HV = \frac{1.8544\ F}{d^2} \tag{3-1}$$

where, F represents the test load (kgf) and d is the average length of two indentation diagonals (mm).

To examine the strength of the joints, a number of shear tests were carried out based on the principle described in Figure 3.12. The shear strength of ECAE joints was examined at room temperature using a universal testing machine (Instron 4469) with 1 mm/s crosshead rate. Three workpieces were tested for each process parameter to assure that the results are highly reproducible.

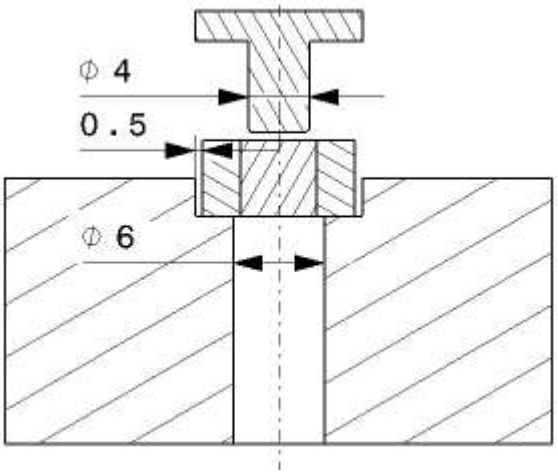

Figure 3.12: Schematic representation of the setup for joint shear strength testing

Following tube-ECAE, all workpieces were prepared for torsion testing according to the ASTM standard E143-13 (E143-13, 2013) in order to study their torsional strength (yield and ultimate value). In order to ensure the reproducibility of shear test result, three samples were prepared for each sample type. Although torsion testing has not been extensively utilized for the evaluation of mechanical properties as much as tensile testing (Dieter & Bacon, 1986), this destructive test can evaluate the mechanical properties of tubular components processed through SPD by allowing for an examination of the full-size components, unlike other methods such as the ring hoop tensile test (Babaei et al., 2014) or ring test (Arsene & Bai, 1998).

Following ECAE and subsequent heat treatment, the workpieces were cut in small pieces 5 mm thick and their cross sections were ground using sand paper of up to 2000 grit. The workpieces were mirror-polished using alumina suspension (down to 0.1 μm) and then cleaned using distilled water and ethanol ultrasonically for subsequent visual characterization. In order to reveal the workpieces' microstructure, metallographic etching was implemented using a mixture of 10 ml H_2O_2 + 20 ml HCl + 50 ml distilled water for the steel part and Kroll's reagent (2 ml HF + 6 ml HNO_3 + 90 ml distilled water) for the aluminum alloy part.

The workpieces' microstructure and joints' interfaces were visually investigated with an Olympus BX61 optical microscope and a Phenom ProX scanning electron microscope in backscattered mode. The chemical composition and fractured sections were characterized by energy-dispersive spectroscopy (Phenom ProX SEM/EDX) using the spot and line scanning modules. Crystallographic characterization of the workpieces and the fractured sections was done with a Pananalytical empyrean x-ray diffractometer using Cu Kα radiation in order to recognize the exact phases formed by the existing chemical elements. The x-ray patterns were obtained at a step width of 0.026^0 and the peaks were indexed using software configured with the XRD system.

In order to investigate the nanomechanical characteristics of the ECAE joint, the variations in hardness across the joints' interfaces were investigated with a Hysitron TI-750D Ubi nano indenter. This equipment uses a three-sided pyramidal diamond indenter (Berkovich indenter tip) with curvature radius of 150 nm. The thermal drift was retained below $\pm$ 0.05 nm/s for all nanoindentation experiments in this study. Furthermore, the loading and unloading durations were set to 30 s at a constant rate of 12 mN/min. Maximum indentation load and holding time at maximum load were set to 6 mN and 3 s respectively. To increase the result reliability, 10 indents were performed on each workpiece and the distance between successive indentations was controlled so as to prevent mutual effects.

3.6. ECAE performance criteria

The ECAE process is a metal flow process operating in pure shear and characterized by several fundamental factors as (Valiev & Langdon, 2006):

- The amount of strain imposed to workpiece in each separate pass.
- The slip systems operating during the pressing operation.
- The consequent shearing patterns present within the as-pressed workpiece.

Taken together, these various processes define uniquely the precise nature of the pressing operation. In this regard, the distribution of EPS, evolution of microstructure and mechanical properties of the workpiece after process were analysed.

It is recognized that grains are effectively refined as a consequence of continuous straining in materials with medium or high stacking fault energies such as aluminum alloys (Wang et al., 2006). Thus, the FEA has been used in order to evaluate the distribution of EPS as a factor to evaluate the capability of ECAE to produce components with finer grain structures (Li et al., 2004).

The slip systems operating during the pressing operation, determine the grains' size and orientation after the ECAE processing. In order to confirm the acceptable performance of designed die the microstructures of processed workpieces have been observed using optical microscope to confirm the formation of equiaxed grains.

Other important factor which determines the grain evolution through ECAE is the temperature rise. It was established that the operating temperature (T_{ECAE}) should be kept below 0.4 of material melting point (T_{melt}) (Valiev & Langdon, 2006). In this research to minimize the effect of friction which leads to temperature raises the pressing speed was controlled as well the surfaces of die and workpiece was lubricated using MoS_2 solid state lubricant.

Finally, the mechanical properties of workpiece after ECAE including yield strength, ultimate strength, ductility and surface hardness were evaluate using numbers of uniaxial tensile and microhardness tests.

CHAPTER FOUR: FINITE ELEMENT ANALYSIS

4.1. Introduction

In the present work, three dimensional (3D) FE-analysis of ECAE has been carried out in order to simulate ECAE-treatment of AA 6063-O with circular cross section, ECAE-treatment of tubular AA 6061-O and joining of aluminum tube and steel rod using elasto-plastic Abaqus/Explicit package.

The main outputs of FE-analysis which have been considered include: (1) analysis deformation behavior of the workpiece through ECAE process in order to design and fabricate tool set as well as confirm the capability of ECAE for processing tubular components and joining dissimilar metallic materials, (2) the evaluation of equivalent plastic strain (EPS) and strain inhomogeneity through process (This output is shown by PEEQ in Abaqus).

It was found that 3D FEA simulation of ECAE provides more efficient results in order to analyze homogeneity of plastic strain in compare with 2D FEA (Suo et al., 2006). Since ECAE is a low-speed operation, the quasi-static condition was considered during FEA. It is well-established that an explicit solution method is among the most promising techniques to solve quasi-static problems. Additionally, in order to precisely determine the deformation behavior of the workpiece as well as to reduce the discrepancy between the numerical and experimental results, the FE-model was set up in accordance with mechanical and geometrical properties identical to those utilized during experiments as explained by details in chapter three.

During ECAE, the accumulation of strain occurred with microstructural evolution subsequently leads to grain refinement and increase of strength. The continuum mechanic based constitutive model based on Prandtl-Reuss theory is expressed the deformation behavior of material through ECAE as:

$$d\underline{\varepsilon}^P = \frac{3}{2}\langle\frac{\bar{\sigma} - \sigma_y}{K}\rangle^{1/m}\frac{d\sigma'}{\bar{\sigma}} \quad (4\text{-}1)$$

where, $d\underline{\varepsilon}^P$, $d\sigma'$, $\bar{\sigma}$ and σ_y represent the plastic strain increment tensor, deviatoric stress tensor, effective stress and yield strength, respectively. The plastic resistance constant, K and hardening exponent, m are determined through tensile test at 450 °C. The deformation behavior is coupled with microstructure evolution through empirical relation by means of accumulated EPS as:

$$\frac{1}{d} = \frac{1}{d_\infty} + \left(\frac{1}{d_0} - \frac{1}{d_\infty}\right)\exp(\frac{-\bar{\varepsilon}}{\varepsilon_c}) \quad (4\text{-}2)$$

where, d and d_0 represent after deformation and initial grain sizes, respectively andε_c and d_∞ are material constants. Accumulated EPS, $\bar{\varepsilon}$ is calculated through analytical equation (equation (2-20)) or employing FEA. Thus, by considering the Hall-Petch law (equation (2-1)) the distribution of plastic strain is employed as a factor to evaluate the capability of ECAE to produce components with finer grain structures.

4.2. Finite element modelling of ECAE

The deformation procedure during the ECAE process was carried by generating 3D FE-model based on principle describe in Figure 3.2 and dimensions are illustrated in Figure 4.1. The die channel angle (φ) and corner angle (ψ) considered in this research were 90° and 37°, respectively. A selection of these angles is based on evolution of equivalent plastic strain (EPS) (Valiev et al., 2000) and strain inhomogeneity (Basavaraj et al., 2009) in the workpiece after ECAE process.

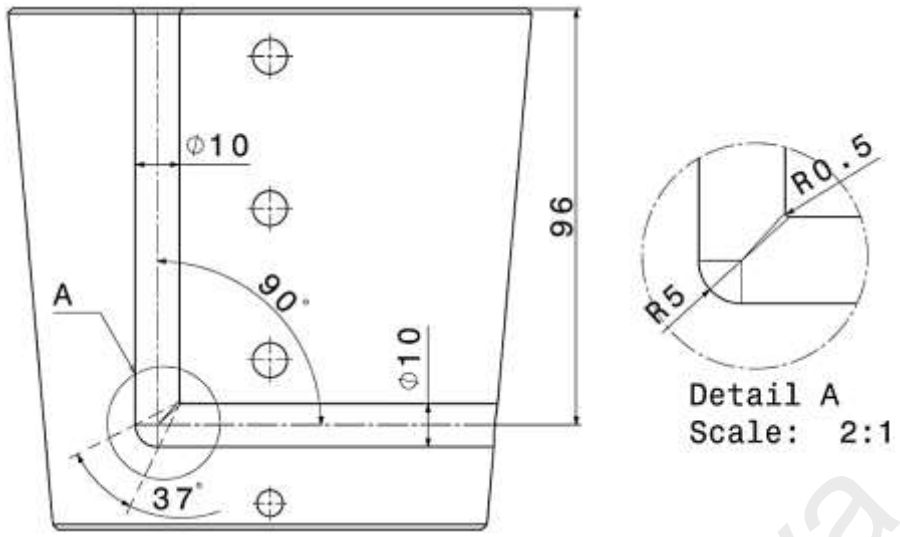

Figure 4.1: ECAE die and respective dimensions used in FEA

The workpiece was considered as a deformable isotropic part and meshed into 6144 brick elements with reduced integration and hourglass control (C3D8R) such that throughout the process the workpiece could produce reasonable results under severe deformation. The material used for the workpiece in the simulation was AA 6063-O with material properties represented in Table 3.1. The hardening behavior of the materials throughout the FEA was described by $\sigma=40\varepsilon^{0.15}$ obtained experimentally using tensile test data. Furthermore, the die and punch were modelled as analytical rigid parts to reduce computational time.

The downward displacement of 70 mm in the z-direction is applied to punch with a prescribed velocity of 7 mm/s. The encastre boundary condition ($U_1=U_2=U_3=UR_1=UR_2=UR_3=0$) is prescribed to the die reference point. The contact between the die and the workpiece was modelled using the penalty scheme and Coulomb friction with a friction coefficient (μ) of 0.1. Furthermore, Abaqus provide the possibility of simultaneous defining of Coulomb and maximum shear stress friction models, which slipping starts regardless of contact pressure if the value of equivalent shear stress exceeds the maximum shear strength. In this regard, the shear friction factor, m of 0.35 was assigned to the FE-model.

4.3. Finite element modelling of tube-ECAE

The deformation behavior of AA 6061-O tube during the ECAE process was analyzed by generating 3D FE-model based on principle describe in Figure 3.8 and dimensions are illustrated in Figure 4.2. The die channel angle (φ) and corner angle (ψ) considered in this research were 120° and 22°, respectively. A selection of these angles is based on evolution of equivalent plastic strain (EPS) (Valiev et al., 2000) and strain inhomogeneity (Basavaraj et al., 2009) and possibility of failure in workpiece during ECAE process.

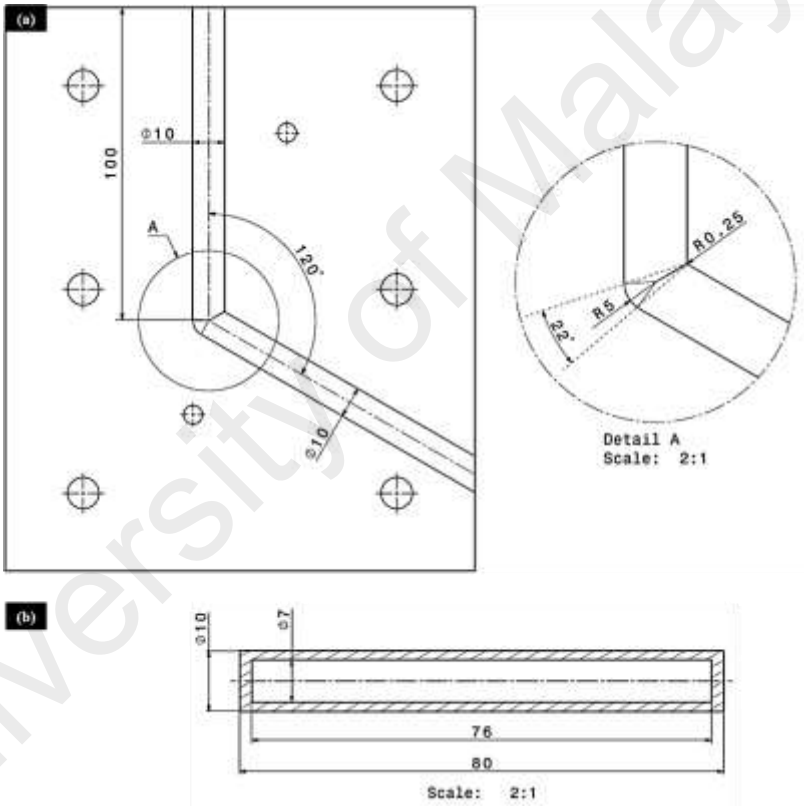

Figure 4.2: (a) ECAE die and (b) tubular workpiece used in FE-modelling

The workpiece was considered as a deformable isotropic part with mechanical properties which is summarized in Table 3.4. The FEA mesh configuration for the workpiece (tube) consisted of 4500 eight-node brick elements with reduced integration and hourglass control (C3D8R). This element type allowed the workpiece to demonstrate reasonable results under severe deformation. The ECAE die and punch

considered as a rigid body to reduce the computational time using a 4-node 3D bilinear rigid quadrilateral element (R3D4).

In order to define boundary conditions, the die was constrained in all directions ($U_1=U_2=U_3=UR_1=UR_2=UR_3=0$) and downward displacement of 75 mm, with velocity of 7.5 mm/s was assigned to punch. The contact between the tool set and workpiece was defined using the penalty algorithm by considering the rigid parts (die and punch) and deformable parts as the master and slave surfaces, respectively. The Coulomb constant μ in the contact interfaces was set to 0.1, which was in the range of a typical ECAE process (Li et al., 2004).

The response of the tube under SPD depended on the shear imposed by the die channel's abrupt angle in addition to the pressure exerted by the fluid, which in turn was affected by tube deformation. Therefore, mechanical response predictions for the hydraulic oil-filled cavity were important for the simulation. With this regard, the Abaqus 6.13 "Surface-based fluid cavity" module was utilized to model the hydraulic oil-filled workpiece cavity. The compressibility of the hydraulic oil was introduced by defining the bulk modulus. The density of the "SAE 30" hydraulic oil and the bulk modulus were considered to be 850 kg/m^3 and 1.5 GPa, respectively, at 20 °C (Totten et al., 2003).

4.4. Finite element modelling of dissimilar joining using ECAE

To characterize the deformation behavior and evolution of EPS throughout the joining process, a 3D FE-model has been constructed according to the principle of the process illustrated in Figure 3.10 and dimensions according to Figure 4.3. Since ECAE joining is a low-speed operation, the quasi-static conditions were considered during the simulation process. In order to precisely determine the deformation behavior of the workpiece as well as to reduce the discrepancy between numerical and experimental results, the FE-model was set up in accordance with mechanical and geometrical

properties identical to those utilized during the experimental process as listed in Table 3.7.

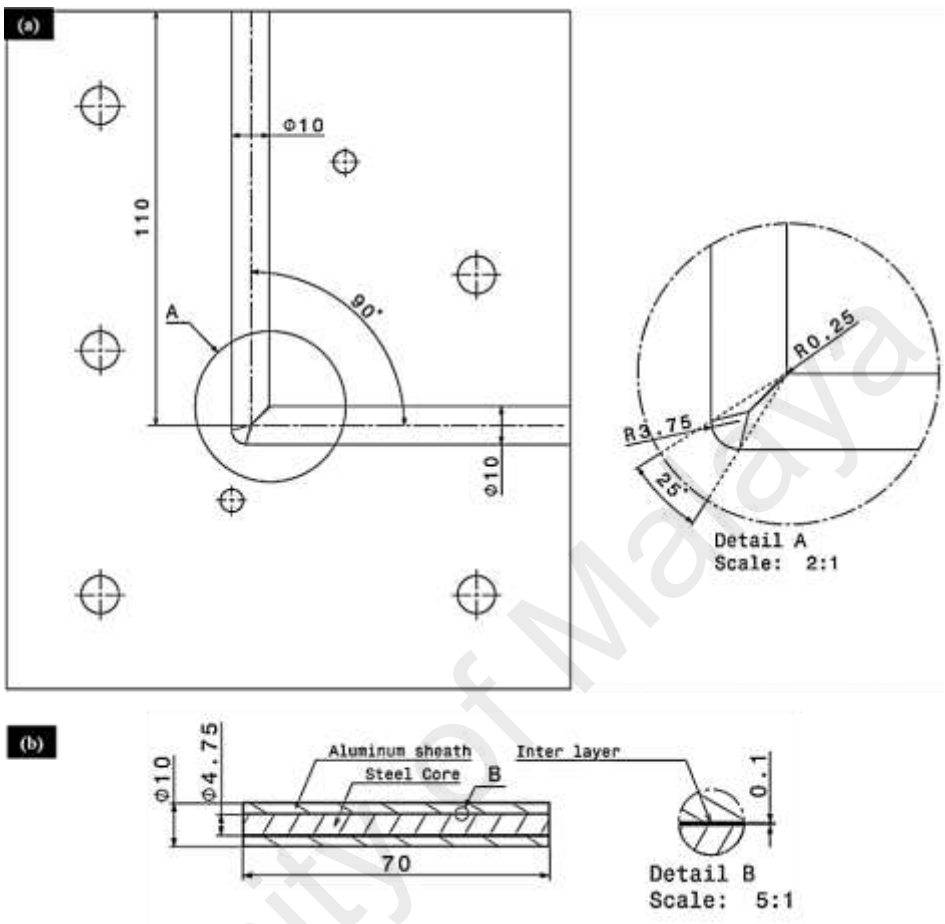

Figure 4.3: (a) ECAE die and (b) assembled workpiece including aluminum sheath, steel core and interlayer used in FE-modelling

The FE mesh configurations for the aluminum sheath, interlayer, and steel core were 2832, 1888 and 1824 eight-node brick elements, respectively, with reduced integration (C3D8R) and hourglass control. In addition, the die and punch were considered as rigid components as well as all three components considered isotropic.

The punch movement was controlled by a prescribed velocity boundary condition which it is given a velocity of 7 mm/s for displacement of 70 mm. Also, the die movement was constrained in all directions as (U_1=U_2=U_3=UR_1=UR_2=UR_3=0). The contact condition between the workpiece, die and punch was defined using a penalty algorithm by considering the rigid and deformable parts as master and slave surfaces, respectively. It

is worth mentioning that Coulomb's constant, μ, at the contact interfaces was set to 0.1, which is within the range of a typical ECAE process (Li et al., 2004).

4.5. Models verification and validation

The biggest challenge in FEA is validation, carefully chosen and closely monitored physical model that confirm whether or not physical reality and virtual reality line up. A consensus among FEA analysts is that validation ensures that there are no hidden disconnects between the model and the physical testing, that correct physical properties are used, and that properties are analyzed accurately based on correct principles of physics. The model validations in this research have been carried out through controlling the model convergence as well as validation of model by comparison of accumulated EPS in current models and previously set up ones.

To visualize the convergence of FEA models, the variation of strain energy vs process period for different mesh size was controlled (Rao, 2004). As an initial run, the workpiece was meshed by 1300 C3D8R elements, and the variation of strain energy was monitored during the simulation. This analysis was terminated during simulation due to excessive mesh distortion as a result of using coarse mesh. The mesh refinement process was repeated to obtain unchanged value for strain energy. In this regard, five other models with the total element numbers of 2312, 3220, 4200, 5250 and 6144 were carried out and variation of strain energy during the simulation was controlled. The variations of total strain energy versus element numbers are summarized in Figure 4.4. As shown in the graph the analyzed solution converges for models, which were mesh with total number of elements greater than 4200.

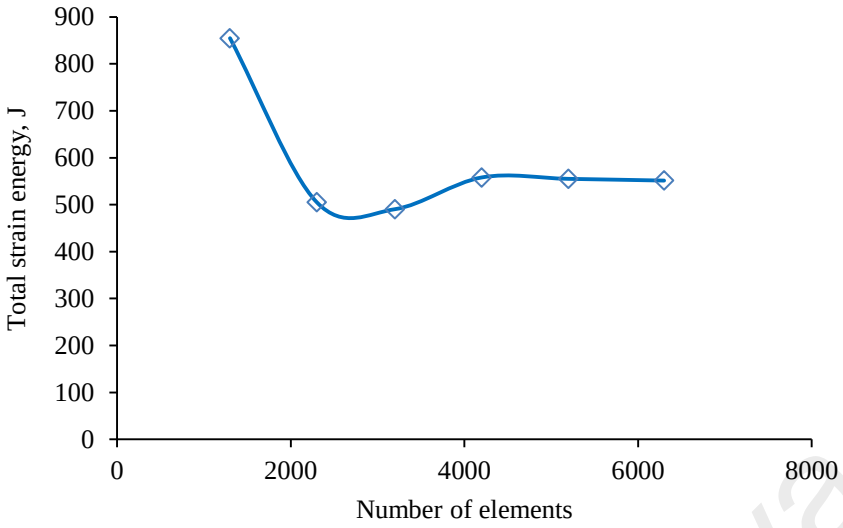

Figure 4.4: Variation of total strain energy vs number of elements in model

The computational efficiency of the simulation in the explicit procedure was increased by artificially increasing the material density using the mass scaling factor. Mass scaling is a tried and proven method for reducing run times in quasi-static analyses where the velocity is low and the kinetic energy is very small relative to the internal energy.

In order to avoid result errors due to the amplified inertia forces, the ratio of kinetic energy to internal energy was monitored to confirm the quasi-static response of the explicit method. The kinetic energy of deforming material should not exceed 5% of internal energy throughout the simulation, however in early increments of explicit analysis an increase of kinetic energy can be neglected due to movement of deformable body before the start of significant deformation (*Abaqus 6.11 user documentation*, 2011). The variation of kinetic energy and 5% of internal energy during the ECAE process are illustrated in Figure 4.5. As can be clearly seen from the graph the value of kinematic energy is significantly below the 5% of internal energy except at early increments of simulation which deformable part just is pushed into the die cavity without having deformation. As an example, in the increment 5.E+05, the value of kinetic energy is almost 5J while the 5% of internal energy is around 4.0E+03 j.

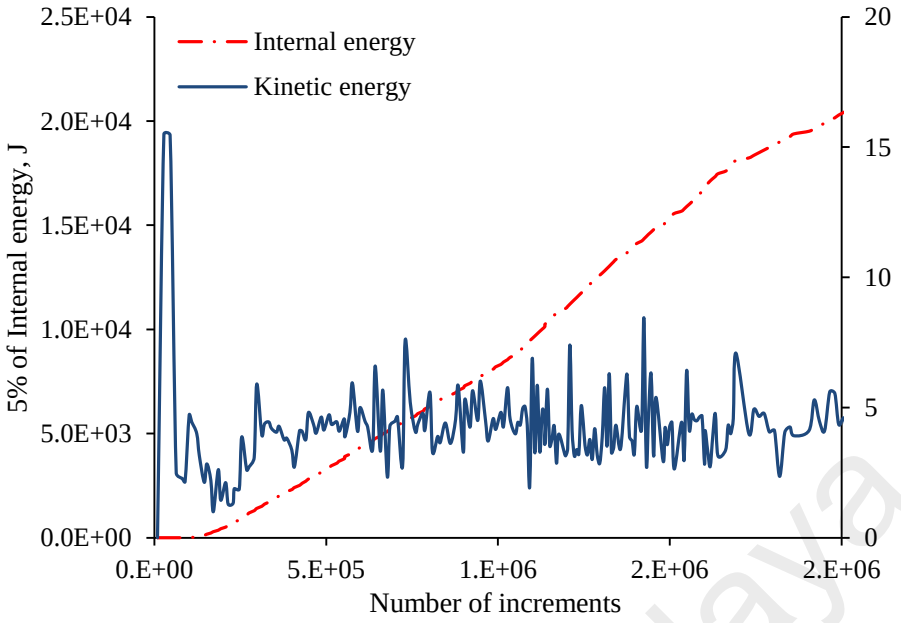

Figure 4.5: Variation of kinetic energy versus 5% of internal energy during ECAE process

In order to validate the physical feature of FEA models through this research the value of EPS which is obtained through ECAE is compared with value obtained from analytical analysis (equation (2-20)). The values of EPS obtained through ECAE depending on different die configuration are illustrated in Figure 4.6. In this regard, the values of EPS, which are obtained through FEA, have been compared with the values presented in Figure 4.6, in order to validate the physical feature of the model.

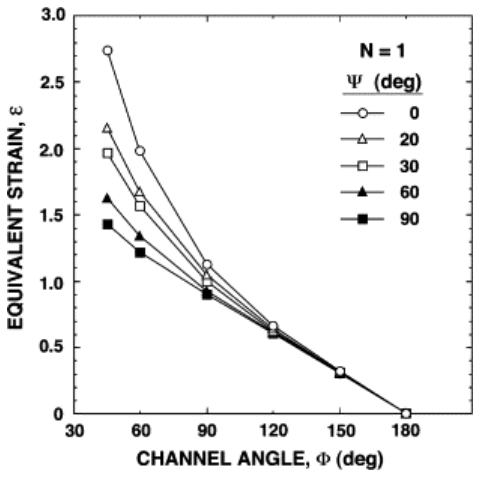

Figure 4.6: Variation of the EPS with the channel angle, Φ, over an angular range of Φ from 45° to 180° for values of the corner angle, Ψ, from 0° to 90° for a single pass (Valiev & Langdon, 2006)

One of the important issues should be considered through the tube pressing is an evaluation of the possible ductile fracture. It is well known that ductile fracture is related to the ability of a metal to withstand a notable degree of deformation prior to fracture when the value of EPS exceeds the fracture strain value ($\bar{\varepsilon}_f$). Prior studies have shown that fracture strain could be correlated to the work hardening exponent (*n*), obtained via uniaxial testing according to the Considère criterion (Wagoner & Chenot, 1996), or in case of complex stress states such as ECAE, through stress triaxiality (Bao & Wierzbicki, 2004).

To explain in detail, for a Hollomon material (isotropic), the power law equation can be used to find the end of uniform elongation as:

$$\bar{\sigma} = k\bar{\varepsilon}^n \tag{4-3}$$

where, *K* and *n* are the strength coefficient and work hardening exponent constants, respectively. The value of equivalent stress ($\bar{\sigma}$) is calculated using equation (2-33).

Accordingly in the case of uniaxial tension, at the end of uniform elongation, the slope of the stress/strain curve was zero. Therefore, we could use equation (4-3) to obtain the load (P) as:

$$In\ P = In\ k + n In\ \bar{\varepsilon} + In\ A_0 - \bar{\varepsilon} \tag{4-4}$$

where, A_0 was the initial area of the tensile test cross section. We can now set equation (4-4) equal to zero in order to obtain the uniaxial tension test criterion:

$$\frac{d(In\ P)}{d\varepsilon} = \frac{n}{\bar{\varepsilon}} - 1 = 0 \tag{4-5}$$

Therefore, according to the uniaxial tension criterion, ductile fracture at the fracture strain value ($\bar{\varepsilon}_f$) could be predicted when:

$$n = \bar{\varepsilon} = \bar{\varepsilon}_f \tag{4-6}$$

As evident, equation (4-6) was independent of stress triaxiality, which significantly affected the occurrence of ductile fracture in the case of three-dimensional processes such as tube ECAE. Stress triaxiality (η) was represented as follows:

$$\eta = \frac{\sigma_m}{\bar{\sigma}} \tag{4-7}$$

where, $\sigma_m = (\sigma_1 + \sigma_2 + \sigma_3)/3$ is the hydrostatic stress. It was found that potential for ductile fracture decreased by increasing the stress triaxiality (Hancock & Mackenzie, 1976). Therefore, the fracture strain ($\bar{\varepsilon}_f$) and stress triaxiality (η) were inversely proportional:

$$\bar{\varepsilon}_f \propto \exp(-\alpha \frac{\sigma_m}{\bar{\sigma}}) \tag{4-8}$$

where, α is the material constant. In order to evaluate the potential for fracture in this study, the point under the greatest amount of strain was monitored during FEA.

CHAPTER FIVE: RESULTS AND DISCUSSION

5.1. Introduction

This chapter is devoted to discuss and analyze the numerical and experimental tests which were carried out to evaluate mechanical properties of AA 6063, capability of ECAE to use for SPD treatment of tubular components and application of ECAE for joining of dissimilar materials.

5.2. Evaluation of the mechanical properties of ECAE-treated AA 6063-O

5.2.1. FE-simulation

Based on the results obtained from FEA, influence of die geometry on workpiece deformation pattern, amount of EPS imposed on the workpiece, the pattern of variation in EPS along prescribed paths and EPS inhomogeneity are discussed in this section.

Figure 5.1 illustrates the plastic deformation zone, steady state zone and corner gap (gap between die internal surface and billet) in the ECAE process. Die channel angle (φ) and workpiece material properties are the two most effective parameters that control the workpiece deformation pattern and amount of EPS (Nagasekhar & Tick-Hon, 2004). According to the results obtained from FEA, a die with channel angle (φ) of 90° successfully produces a sound workpiece and impose notable amount of EPS to workpiece.

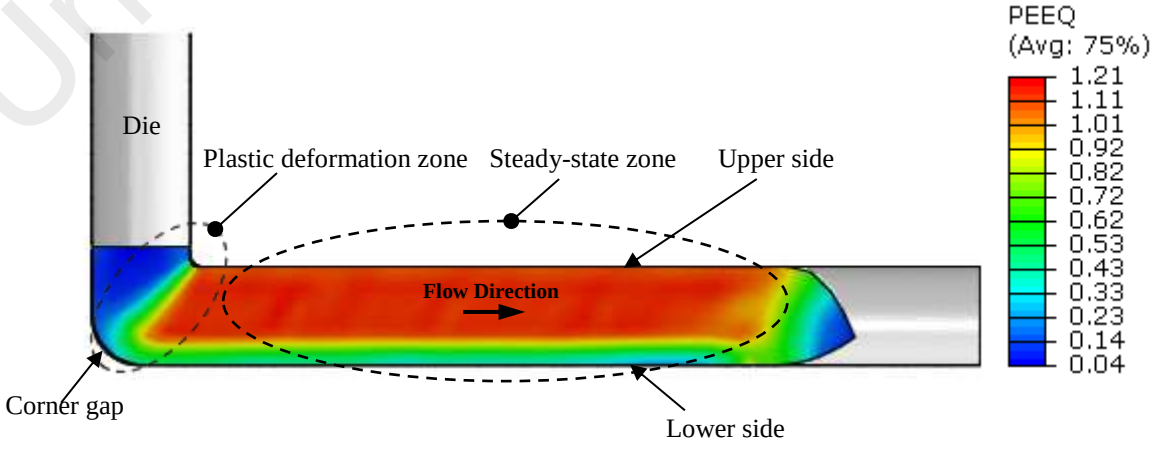

Figure 5.1: Major zones of the ECAE-treated workpiece using die with ψ=37° and φ=90°

According to the results obtained from FEA, as a consequence of strain accumulation in workpiece during ECAE processes an enhancement in mechanical properties of workpiece can be expected. Figure 5.2(a-d) shows the distribution of EPS in the processed workpiece for punch strokes 0, 10, 45 and 75 mm, respectively. Figure 5.2 shows that, significant high amount of EPS is accumulated to the workpiece as it passes through the die abrupt angle. In this regard, the approximate average strain introduced to the workpiece according to FEA is ~ 0.92. This value is in accordance to the value of 0.99 obtained using equation (2-19).

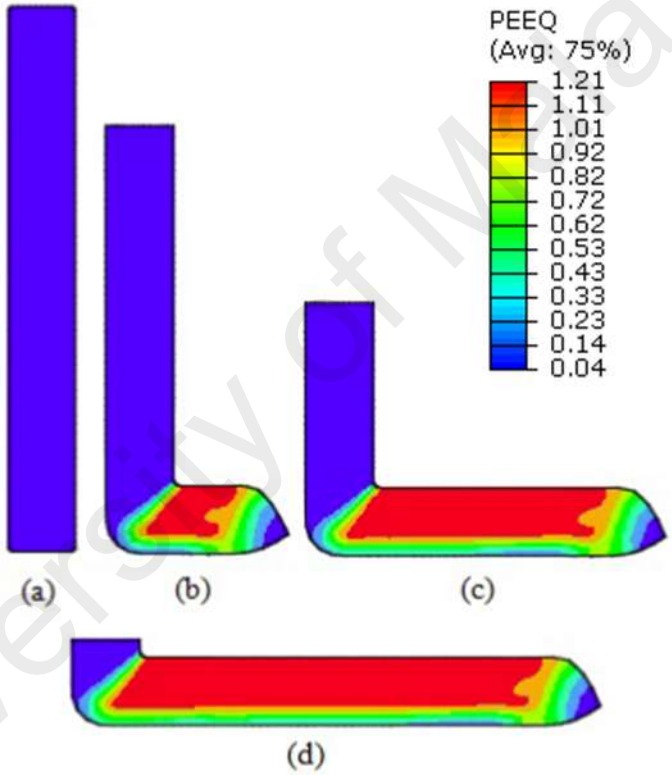

Figure 5.2: FE results for equivalent plastic strain distribution in the workpiece under ECAE: Stroke (a) 0 mm, (b) 10 mm, (c) 45 mm and (d) 75 mm

As is obvious from Figure 5.2, the distribution of EPS is not uniform in the processed workpiece. To evaluate this non-uniformity in EPS distribution, a virtual plane perpendicular to the flow direction in steady state zone was considered to quantify the EPS variation. Over this plane, two paths along the outer circumferential direction and the diameter of the pressed workpiece were defined. These distributions are illustrated in Figure 5.3.

It is clear in Figure 5.3 that distributions of EPS at the cross section of the workpiece after ECAE are non-uniform and have similar trends along the outer circumferential and diametric paths. The EPS value in the upper side (Figure 5.1) reached a maximum value of ~1.1, while in lower side dropped to minimum value of ~ 0.6.

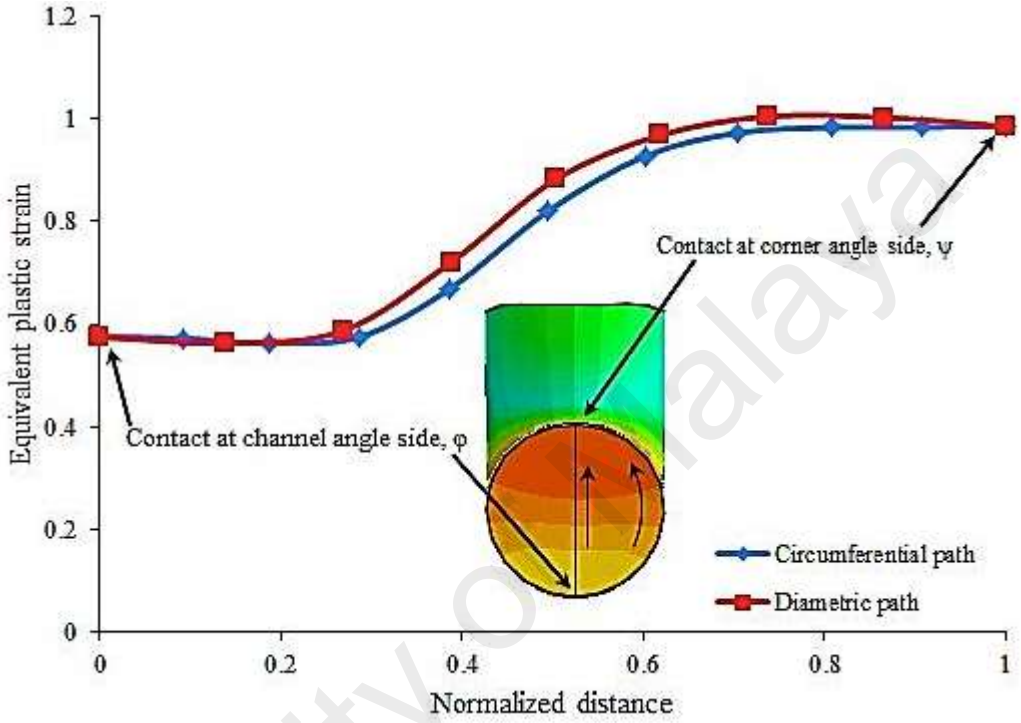

Figure 5.3: Distribution of EPS in diametric and circumferential paths at the cross section of a specimen after ECAE

In-homogeneity index, C_i, defined by equation (2-21) in steady state zone is almost 0.52 for current design (ψ=37° and φ=90°), which provide acceptable strain homogeneity in workpiece compared with results obtained for different die configuration by (Basavaraj et al., 2009).

5.2.2. Mechanical properties

In order to investigate the tensile strength and ductility of the samples indicated in Table 3.2 a number of tensile tests according to ASTM Standard E8 were performed. The tensile test results are illustrated in Figure 5.4.

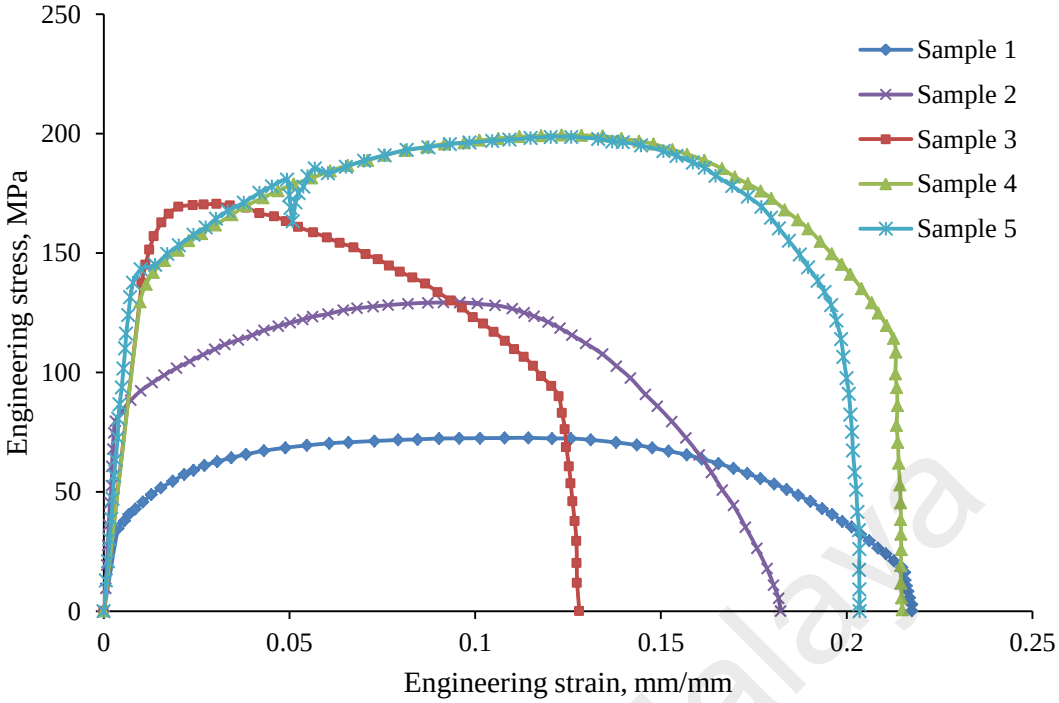

Figure 5.4: Measured engineering stress-strain curves for as-received (sample 1), heat-treated (sample 2), ECAE- treated (sample 3), ECAE+heat-treated (sample 4) and ECAE+heat treated+ hard anodized (samples 5)

In the ECAE process, the grains are refined as a result of extreme EPS which is imposed on the workpiece. The sub-micron size grains prohibited the dislocation movement more effectively. Grain size and metal strength are described by the Hall-Petch relationship (Dunstan & Bushby, 2014). As indicated in Figure 5.4, the yield stress of the sample processed by ECAE (sample 3) significantly improved by almost 300% and 95.4% in comparison with the as-received material (sample 1) and HT material (sample 2) respectively. However, ultimate tensile strength improvement occurred for samples 4 and 5 as a result of heat treatment after the ECAE process.

An abrupt drop in stress-strain curve of sample 5 (HA coated sample) was observed after a strain of about ε=0.05. In the case of uncoated samples (samples 1-4), as result of continuing extension, strain localization in sample deformation length and reduction in cross sectional area of sample occurs uniformly until necking point. However, in the case of coated sample (sample 5) as a result of different material properties of coated layer (Al_2O_3) and substrate material (AA6063), series of cracks are nucleated in coated

layer (brittle layer). These cracks in coated layer are accumulated and sudden fracture in coated layer occurs. This phenomenon can be attributed to the observed drop in stress-strain curve of sample 5.

The data obtained for the presentation of tensile ductility following SPD processing are rather contradictory. While some researchers reported enhanced tensile ductility after SPD owing to the combination of UFG size effects and high-density dislocations in a new mechanism (Valiev et al., 2002), several others claimed that after the SPD process show low tensile ductility due to strong strain of localization materials (Estrin & Vinogradov, 2010). Tensile test results indicate that SPD process improves the yield stress (0.2 % offset strength), while having a slight detrimental effect on ductility (elongation at break). Tensile test results show that yield stress of sample 3 (ECAE processed) increased by ~ 90% compared with sample 2 (heat treated); however, heat treatment following the ECAE process does not improve the yield stress. Yield stress value for samples 4 and 5 confirm this finding. Results also show that the ECAE process has no significant negative effect on ductility of the AA 6063. A significant improvement of ~ 65% in ductility of ECAE processed AA 6063 can be obtained by considering the post-ECAE heat treatment process.

Concerning fatigue behavior, an increase in the strength of metallic alloys in nanostructure state justifies the exception for fatigue strength enhancement as well; however, the probability of decreasing tensile ductility must be carefully considered.

The hardness and tensile test results for five samples are demonstrated in Figure 5.5(a) through 5.5(c). The average surface hardness value of each sample was achieved from 3 different points on the sample's surface area. Also, to investigate the variation of surface hardness across the workpiece surface area after ECAE, micro hardness testing was carried out on 3 equidistant points in longitudinal direction.

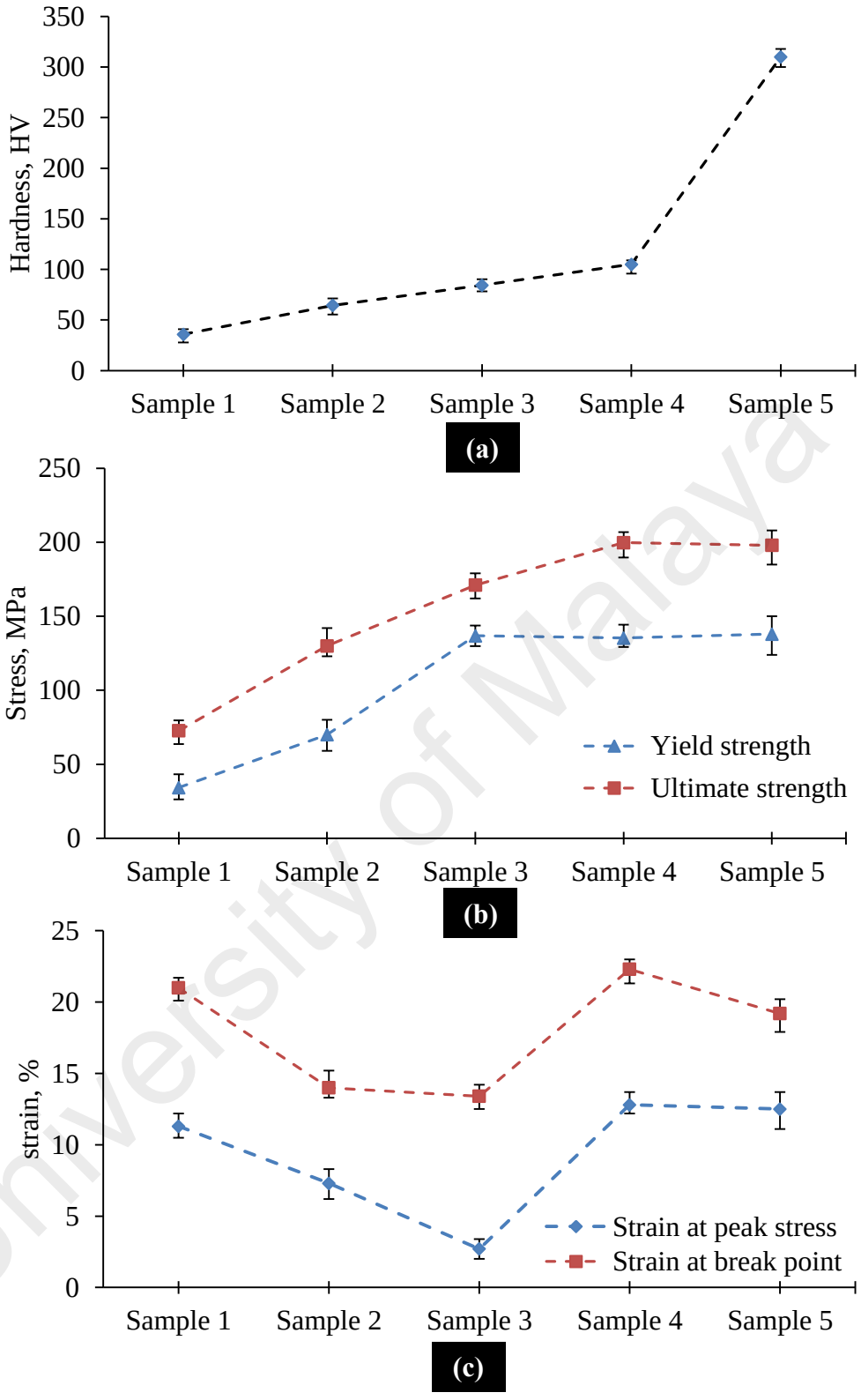

Figure 5.5: (a) Microhardness, (b) yield and ultimate strength and (c) strain at peak stress and break point for sample 1(as-received), sample 2 (heat treated), sample 3 (ECAE-treated), sample 4 (ECAE+HT treated) and sample 5 (ECAE+HT+HA)

As shown in Figure 5.5(a), the surface hardness of sample processed by ECAE (85 HV) is higher than sample 1 (34 HV) and sample 2 (65 HV). This improvement can be explained by the nature of ECAE method leading to ultrafine grains and accordingly higher density, which leads to higher surface hardness. Further enhancement in surface hardness was achieved in sample 4 with heat treatment. As a consequence of hard anodizing and formation of Al_2O_3 on substrate billet surface, the surface hardness of sample 5 significantly increased and reached 310 HV. The results of other research on micro hardness signified that the ECAE process yielded higher values than the original form in coarse grain state (Azushima et al., 2008; Horita & Langdon, 2005).

By studying Figure 5.5(b) it can be concluded that the ultimate strengths of samples processed by different techniques (HT, ECAE, ECAE+HT and ECAE+HT+HA) increased to values of 130, 171.1, 199.8 and 198 MPa respectively, while the ultimate strength of sample 1 was 72.7 MPa. Also results regarding strain (Figure 5.5(c)) signify recovery of strain at peak stress and break point as a consequence of post-ECAE heat treatment; however, hard anodizing slightly reduces the ductility of ECAE+HT treated samples.

5.2.3. Fretting fatigue life

Experiments were conducted to study the fretting fatigue life of the samples listed in Table 3.2. The experiments were performed for a stress ratio of R= -1, 50 Hz, constant contact stress of 100 MPa and working stress amplitudes of 30-150 MPa (except for samples 1 and 2).

Several empirical models were developed to predict fatigue crack growth and fatigue life (Nelson, 1977). In cases where lifetime is dominated by fatigue crack initiation, using the stress-life curve (S/N) is a common method. The relationship between the

stress amplitude (σ_a) and number of cycles to failure (N) values was determined by using fatigue data (Stanzl-Tschegg, 2014).

In this study, five type of samples (as summarized in Table 3.2) were examined under similar conditions and average value was used to obtain each data point for formation of the S/N curves.

Figure 5.6 illustrates the fatigue and fretting fatigue life of sample 1 (as-received). As shown in the figure, the fatigue and fretting fatigue lives of the original samples are almost the same at high bending stress (70 MPa), which is due to the high softness and flexibility of the materials. It means that before fretting could affect the fatigue life of the original sample, all samples failed because of their high deflection that caused them to distort in most cases. At low bending stress (30 MPa) a slight difference in plain fatigue and fretting fatigue lives are seen.

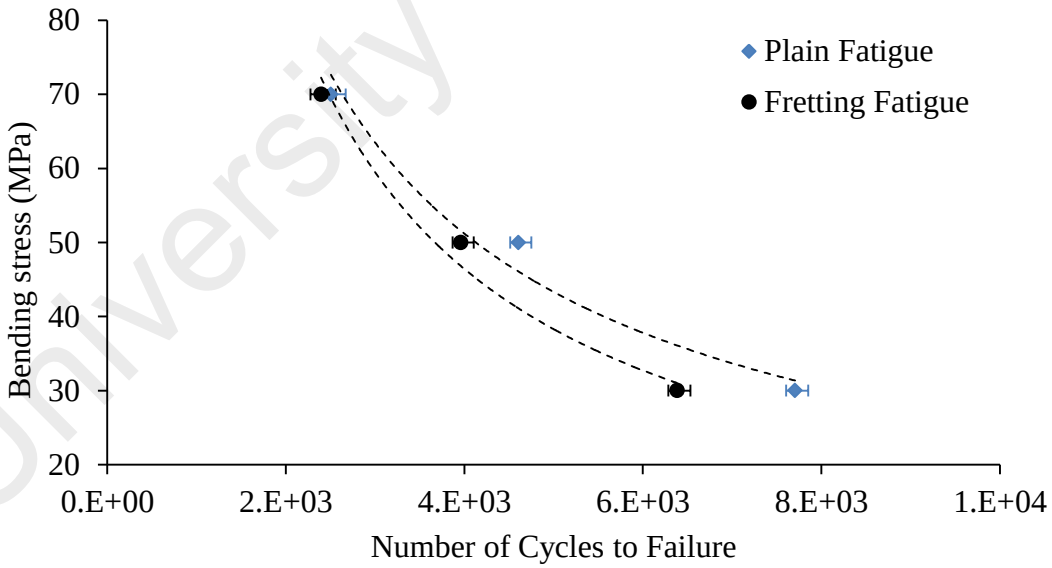

Figure 5.6: S/N curves of fatigue and fretting fatigue for sample 1 (as-received)

Figure 5.7 presents the S/N curve of plain fatigue and fretting fatigue lives of sample 3 (ECAE-treated). From the figure it can be understood that fretting has a negative effect on the fatigue life of ECAE-treated samples. By comparing Figure 5.6 and 5.7, it was found that ECAE treatment has a significant effect on enhancing the fatigue and fretting

fatigue lives of samples at low and high cyclic loads, which may be attributed to improvement in surface hardness and tensile strength of the samples after the ECAE processing.

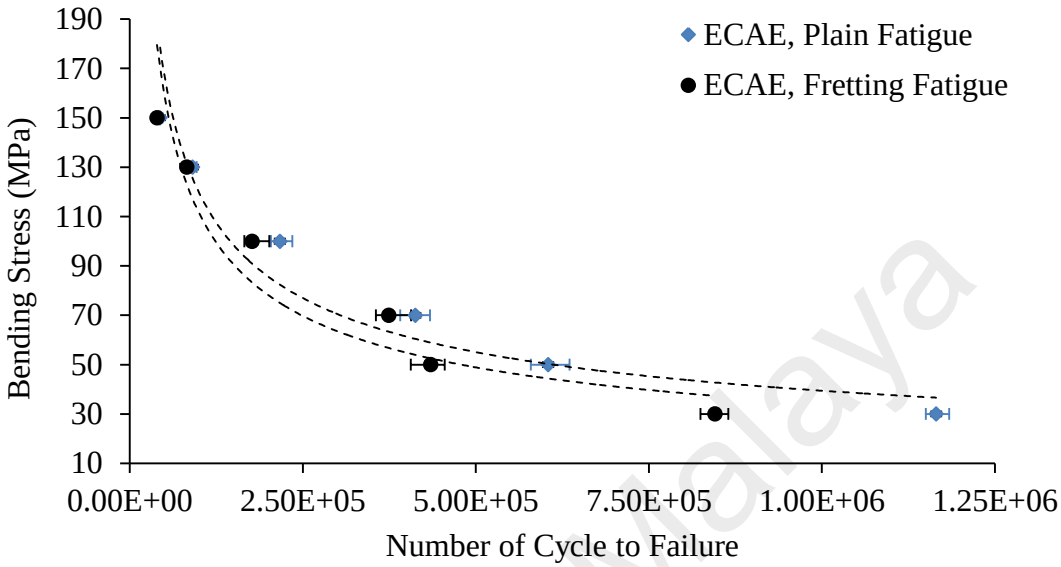

Figure 5.7: S/N curves of fatigue and fretting fatigue for sample 3 (ECAE-treated sample)

The fatigue and fretting fatigue lives of the heat-treated specimen (sample 2) are presented in Figure 5.8, which shows that T4 heat treatment has positive effect on increasing the fatigue and fretting fatigue life of the samples compared to original samples.

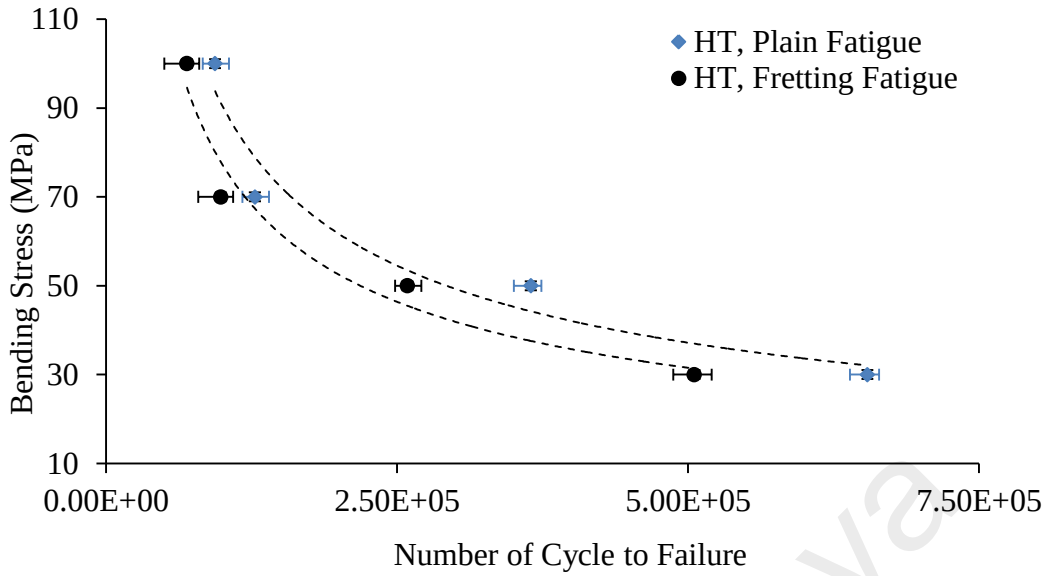

Figure 5.8: S/N curves of fatigue and call fretting fatigue for sample 2 (heat-treated sample)

Figure 5.9 manifests the S/N curve of the fatigue and fretting fatigue lives of sample 4 (double treatment including ECAE and HT processes). Figure 5.9 indicates that fretting still has a negative effect on the fatigue life of samples at low and high bending stresses. However, from a comparative study between Figure 5.6 through 5.9 it is apparent that the double treatment (ECAE + HT) could increase both the fatigue and fretting fatigue life of the samples. These improvements may be owing to the higher surface hardness and tensile strength of samples after the double treatment.

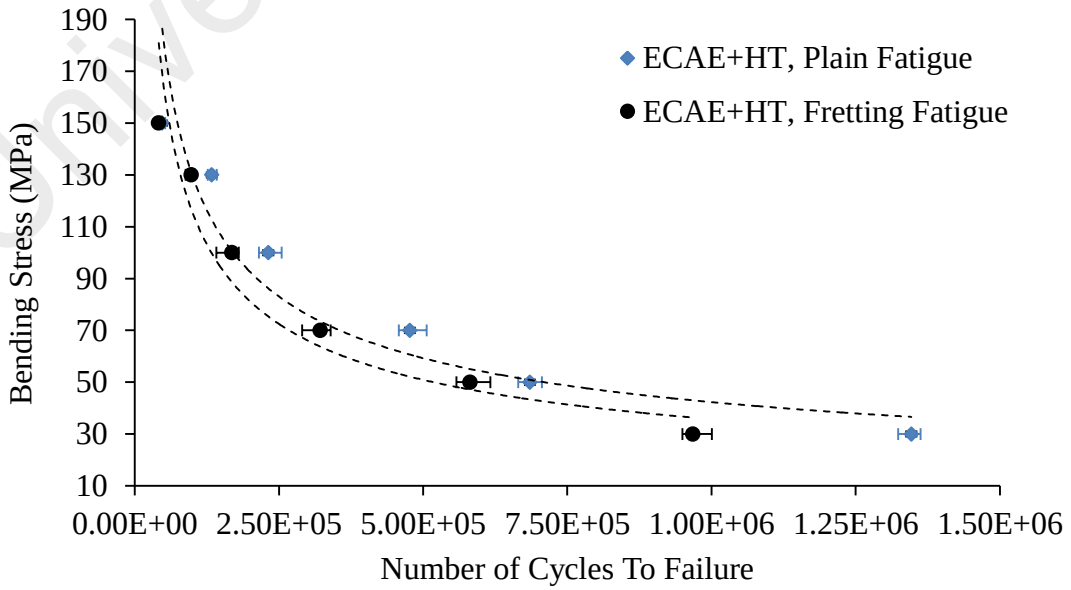

Figure 5.9: S/N curves of fatigue and fretting fatigue for sample 4 (ECAE and heat-treated sample)

The S/N curve of the fatigue and fretting fatigue of sample 5 (triple treatment comprising SPD, HT and HA coating) is depicted in Figure 5.10, which indicates that hard anodizing can improve the fretting fatigue life of samples (ECAE + HT-processed) slightly at low cycle fatigue, while at high cycle fatigue it has a reverse effect.

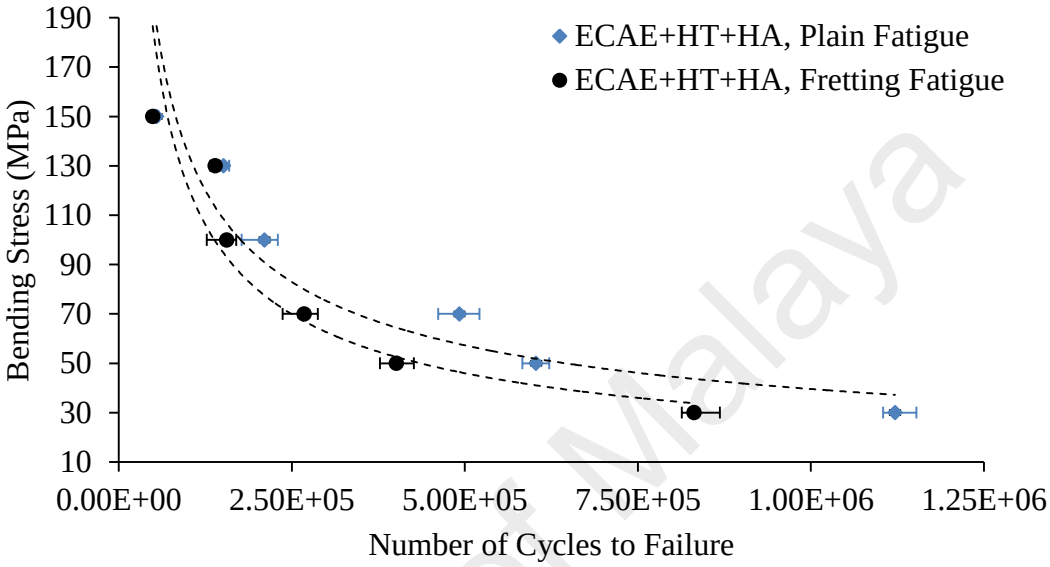

Figure 5.10: S/N curves of fatigue and fretting fatigue for sample 5 (ECAE, heat-treated and hard anodized sample)

Upon comparing Figure 5.7 through 5.10, it is shown that the double treatment has better effect on enhancing the fatigue and fretting fatigue life of specimens at both low and high bending stresses. An assessment of Figure 5.7 through 5.10 signifies that fretting has catastrophic effects on the fatigue life of samples in all cases owing to the stress concentration under the fretting pads, that causes crack initiation and propagation in the contact areas (pads and samples).

From a quantitative study between S/N curves it is concluded that the ECAE treatment enhances the plain fatigue and fretting fatigue lives of samples at high (30 MPa) and low (100 MPa) cyclic loads more than the HT technique by 78% and 67%, and 131.7% and 154.38% respectively. The results also display that the ECAE+HT technique significantly increases the fatigue and fretting fatigue lives of the samples compared to the ECAE method at high and low cycles by 15.56% and 8.33%, and 14.4% and 5.1%

respectively. Hard anodizing of AA6063 increased the fatigue and fretting fatigue lives of the ECAE+HT-processed samples at low cycle by 15.5% and 18.4% respectively; however, for high cycles the hard anodizing produced reverse results whereby the fatigue and fretting fatigue lives of the ECAE+HT-processed samples decreased by 16.7% and 30% respectively.

In the contact surface region where the frictional shear stress is localized, the possibility of fatigue crack initiation increases remarkably and initial crack propagation accelerates. Therefore, the reduction in crack nucleation life affected by concentrating of the local stress leads to diminished fatigue life by fretting fatigue damage. One of the major causes of acceleration of crack initiation is the wedge effect. This effect is a result of wear debris penetration into the microscopic initial fretting fatigue cracks, which significantly accelerates the crack growth. However, the effect is considered to decline if the cracks are completely filled with wear debris because this debris cannot penetrate into the cracks any further (Szolwinski & Farris, 1996).

In rotating-bending condition, formation of unwanted debris accelerate significantly in high cycle fatigue and fretting fatigue condition (Zalnezhad et al., 2013). For Samples 1-4 this debris consists of substrate material particles (AA6063) and fretting pad particles (AISI 4140), while for sample 5 coated later particles (Al_2O_3) are also produced in fatigue and fretting fatigue zones. According to Figure 5.5(a) hardness of Al_2O_3 is significantly higher than other existing particles. As a result of crack nucleation and subsequent wedge effect in high cycle fatigue, the sample subjected to hard anodizing (sample 5) demonstrate shorter fatigue life in high cycle, while in low cycle fatigue this layer suppresses the crack nucleation and pit formation. It is believed that at high cycle fatigue, ceramic debris with nano or micro size have enough time to be removed from the surface of coated material due to bending and cyclic loading. These hard and wedge shape particles may increase the stress concentration in the region

between the fretting pads and specimen leading to crack initiation and propagation toward substrate that result in earlier failure compared to other treated (HT+ECAE) samples.

It is obvious that cracks randomly initiate at points (or a point) which are located around the periphery of the workpiece in plain fatigue, while during fretting fatigue cracks inevitably initiate from the same location at a point adjacent to the leading edge of the fretting areas where induced bending and shear stresses reach maximum values compared with free surfaces (Estrin & Vinogradov, 2010). Cracks propagate from the contact areas between the fretting pads and sample resulting in the occurrence of a sample's final fracture cross section. Figure 5.11 shows the typical cross section of fractured samples ((ECAE+HT) and (ECAE+HT+HA)) at bending stress of 70 MPa, and 3.2×10^5 and 2.6×10^5 cycles respectively. The effects of fretting damage on the sample (contact area) are clear in these figures as a consequence of stress concentration under the fretting test pads.

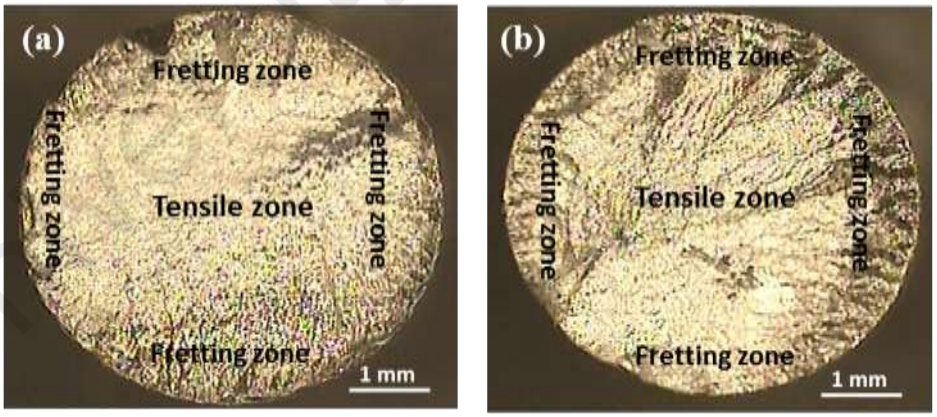

Figure 5.11: Typical microscopic view of the fractured samples' cross sections: (a) ECAE+HT and (b) ECAE+HT+HA under fretting fatigue

Figure 5.12(a-d) shows microscopic images of different types of fractured samples (ECAE, HT, ECAE+HT and ECAE+HT+HA) at bending stress of 50 MPa and 4.4×10^5, 2.5×10^5, 5.8×10^5 and 4.4×10^5 cycles respectively. It is clearly observed under the microscope that there are several cracks and pits in the cross sections of the

fractured samples. The cracks near the outer areas of the fractured samples were initiated and propagated owing to the stress concentration under the friction pads around the specimens. Figure 5.12(d) indicates that even after hard anodized coating (Al_2O_3) cracks could initiate and grow in the coating under the friction pads. Also, with additional cyclic load the cracks propagated toward the samples and led to earlier fracture compared to the HT and ECAE+ HT-processed samples.

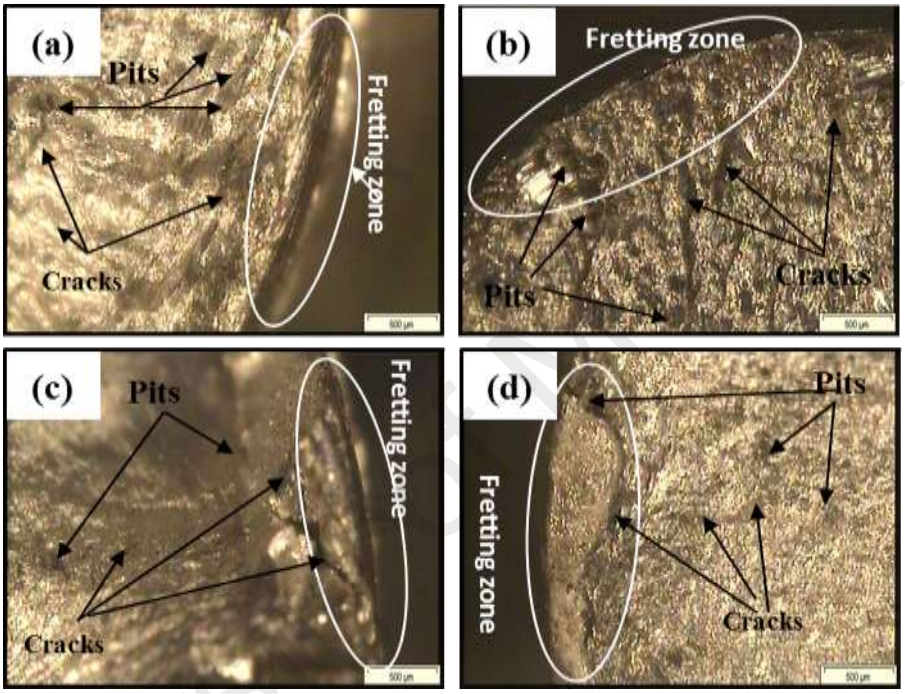

Figure 5.12: Microscopic images of fractured samples' cross sections: (a) ECAE, (b) HT, (c) ECAE+HT and (d) ECAE+HT+HA under fretting fatigue

For further investigation, scanning electron microscopy (SEM) images of fractured samples at different conditions were taken. Figure 5.13(a-d) present the cross-sectional views of fractured samples after ECAE (Figure 5.13(a)), heat treatment (Figure 5.13(b)), double treatment (Figure 5.13(c)) and triple treatment (Figure 5.13(d)) processes at 30 MPa bending stress and after 8.4×10^5, 5×10^5, 9.6×10^5 and 8.3×10^5 cycles respectively. It seems that after double treatment (sample 4) the effect of fretting on the AA 6063 surface decreased as the crack propagation under the fretting pads diminished in Figure 5.13(b) compared to Figure 5.13(a) due to higher surface hardness achieved after the ECAE and heat treatment processes.

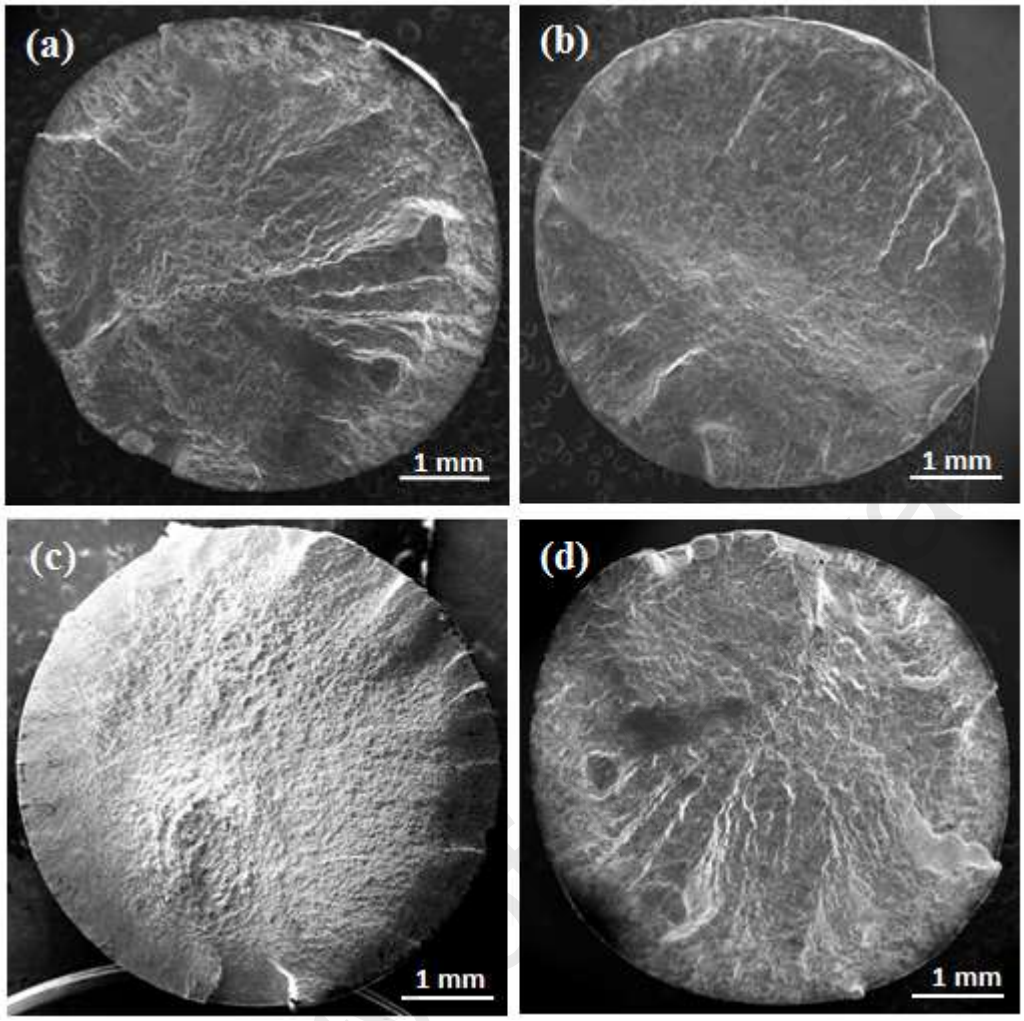

Figure 5.13: Fractures of samples after (a) ECAE (sample 3), (b) HT (sample 2), (c) ECAE+HT (sample 4), and (d) ECAE+HT+HA (sample 5) during the fretting fatigue test

Figure 5.14(a-d) illustrate the SEM images of fractures of hard anodizing (HA) coated samples under the fretting fatigue test at contact pressure of 100 MPa for: (a) bending stress of 130 MPa and 1.4×10^5 cycles, (b) 100 MPa and 1.6×10^5, (c) 70 MPa with 2.5×10^5 and (d) bending stress of 50 MPa with 4×10^5 cycles respectively.

Hard anodized coating enhanced the fretting fatigue life of samples for high bending stresses (130 MPa and 150 MPa), which was attributed to the generation of hard ceramic (alumina). Meanwhile, in lower stress regions the results were reversed on account of micro and nano crack generation and the brittleness of the coated area (Zalnezhad & Sarhan, 2014). Fatigue life decreases with increasing bending load. For HA coating samples, a reduction of 14% fretting fatigue strength was recorded at low

bending stress compared to the double treated (ECAE+HT) samples. The porous and brittle nature of the coating layer (alumina) which was formed on substrate (AA 6063) and tensile residual stress imposed onto the substrate during the hard anodizing process is attributed to the reduction of fretting fatigue life of anodic-coated parts. At 130 MPa bending stress, a small crack was noticed at the substrate and coating boundary. Cracks are generated due to interfacial shear stress between fretting pad and sample. Concentration of stress may have a stimulating consequence on formation of crack in coated surface. Crack may simply initiate at high cycle fatigue due to the brittleness of thin film coating. These cracks behave as a core for superficial cracks in the substrate material (AA6063), even though due to the numerous cracks nucleation in the interior coated layer fracture may occur (See Figure 5.14(d)). This phenomena and wedge effect can be potentially considered as reasons for reducing the fatigue and fretting fatigue life at high cycles (See Figure 5.14(d)).

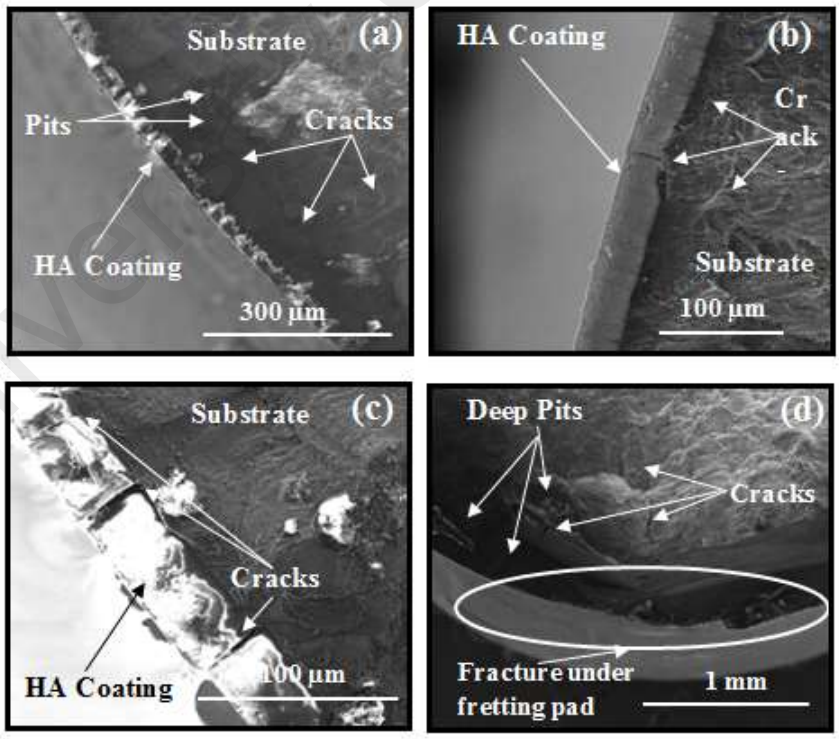

Figure 5.14: Fractured HA-coated specimens under the fretting fatigue test at contact pressure of 100 MPa for (a) bending stress of 130 MPa and 1.4×10^5 cycles, (b) bending stress of 100 MPa and 1.6×10^5 cycles, (c) bending stress of 70 MPa and 2.7×10^5 cycles, and (d) bending stress of 50 MPa and 4×10^5 cycles

5.3. ECAE treatment of tubular components

5.3.1. FE-simulation results

The FEA has been carried out in order to evaluate the possibility of ductile fracture by considering the evolution of stress triaxiality, EPS and equivalent stress. As well the deformation behavior of tube trough die and distribution of EPS as the grain refinement indicator were analyzed.

5.3.1.1. Evolution of equivalent plastic strain

In order to ensure grain refinement during ECAE of tubular AA 6061-O, the strain value accumulated in the workpiece is estimated using Equation (20), for the die illustrated in Figure 4.2. According to the die angles (ψ = 22° and φ = 120°) and considering one pass of ECAE, equation (2-20) estimated the EPS to be 0.63. This value was a reasonably large strain that could effectively refine the grains of tubular components via more straightforward processes compared with other common techniques such as TCAP (Faraji et al., 2011), TCP (Farshidi et al., 2014), HPTT (Tóth et al., 2009), TCEC (Babaei & Mashhadi, 2014), and ASB (Mohebbi & Akbarzadeh, 2010).

As the effects of friction and strain inhomogeneity were not considered in equation (2-20), the distribution of EPS was calculated numerically through FEA. Figure 5.15 illustrates the distribution of EPS throughout the tube after completing the ECAE process, clearly showing that the proposed method is capable of exerting an acceptably high amount of EPS to the workpiece. The accumulated EPS was approximately 0.7 at the upper surface section of the tube, which was in contact with the corner angle, whereas this value reduced down to nearly 0.57 at the lower surface of the tube (the region that was in contact with the channel angle). Accordingly, the value of EPS calculated based on the analytical solution (equation (2-20)) revealed an approximate

value of 0.63, which could roughly be considered as the average FEA outcome value mentioned above.

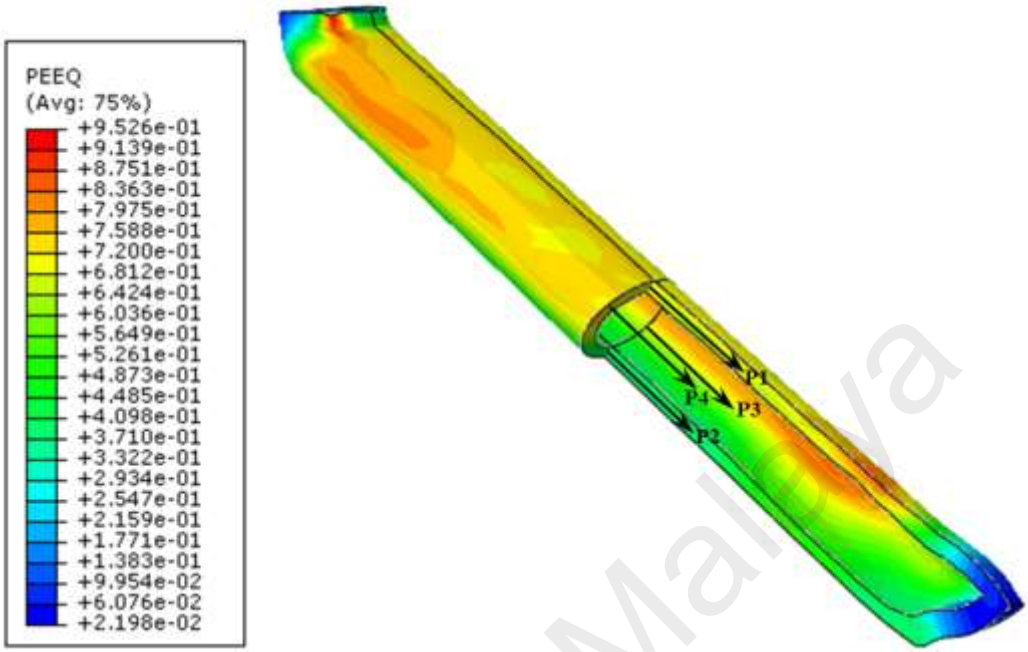

Figure 5.15: Distribution of the equivalent plastic strain (EPS) through workpiece at the end of the ECAE process

In order to quantify the homogeneity of EPS in the tube after ECAE, EPS was analyzed at the middle of the tube thickness along four different longitudinal paths (directions: P1, P2, P3, and P4) as depicted in Figure 5.15, with the results illustrated in Figure 5.16. From this figure, the homogeneity of EPS was evident for each path. However, specifically considering each direction, moderate inhomogeneity in EPS was apparent along direction P2, exhibiting a relatively low value of ~0.57, while directions P3 and P4 exhibited higher values of ~ 0.8.

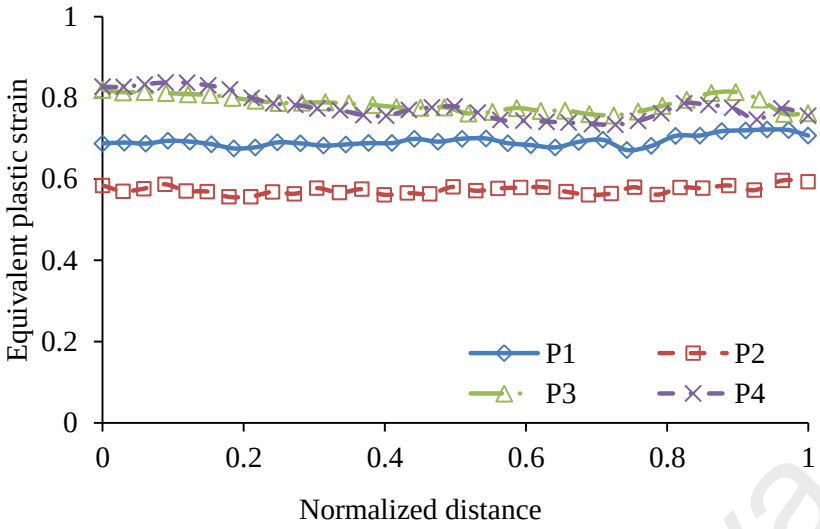

Figure 5.16: Distribution of the effective plastic strain (EPS) in the longitudinal direction along paths P1-P4

Microstructure homogeneity and hardness uniformity were proportional to the homogeneity of EPS, which was imposed within the workpiece via ECAE (Xu et al., 2007). The C_i values according to equation (2-21) in the longitudinal direction of the tube for all four paths (P1, P2, P3, and P4) were approximately 5%. However, the value of C_i for the entire tube was almost 30%, indicating higher homogeneity compared to other methods such as HPTT (Tóth et al., 2009).

5.3.1.2. Hydrostatic stress and thickness distribution analysis

FEA results in Figure 5.17 revealed that the hydrostatic pressure over the internal surface of the tube varied during pressing. With this regard, the hydrostatic pressure distribution at the inner surface of the tube along path A-A' at a punch stroke of 3.5 mm (stage one), 35 mm (stage two), and 70 mm (stage three) was measured and summarized in Figure 5.17. The hydrostatic pressure imposed on the workpiece at the onset of dead zone formation when the punch stroke was 3.5 mm (stage one) consistently reached a value of ~60 MPa, signifying that the hydraulic oil was under pressure.

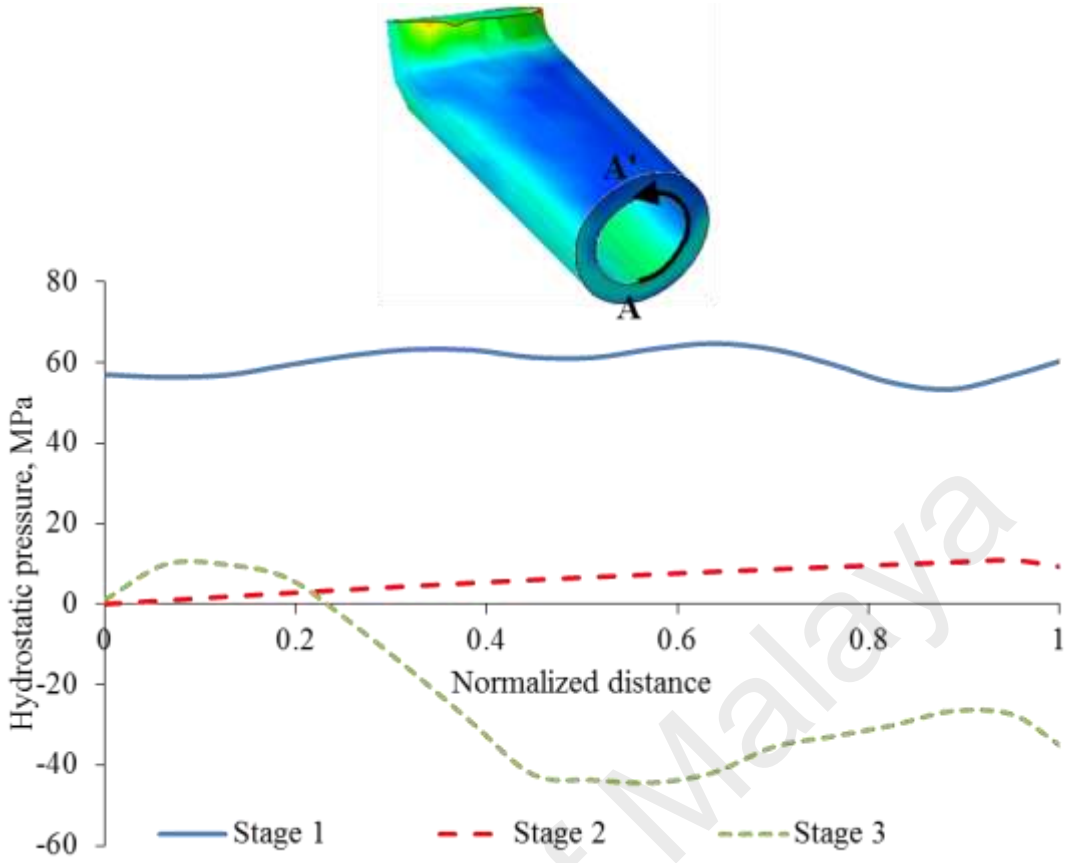

Figure 5.17: Variation in hydrostatic pressure along path A-A' at stage one (punch stroke of 3.5 mm), stage two (punch stroke of 35 mm), and stage three (punch stroke of 70 mm)

At a punch stroke of 35 mm (stage two), the hydrostatic pressure decreased significantly and reached zero at the bottom internal surface of the tube (point A). However, the hydrostatic pressure increased slightly across the internal surface along the path A-A', reaching a value of ~10 MPa at the upper internal surface of the tube (point A'). Finally, it was observed with a punch stroke of 70 mm (stage three), that the hydrostatic pressure was positive at the lower internal tube surface adjacent to the die corner angle (point A). However, by moving towards point A', the hydrostatic pressure exhibited negative values at the internal tube surface. This variation in hydrostatic pressure indicated that the oil pressure varied during ECAE and affected the tube geometry.

In order to further investigate the effect of oil pressure on geometry, variations in the tube wall thickness were measured. Figure 5.18 demonstrates the thickness distributions

along the P1, P2, P3, and P4 directions (Figure 5.15). The thickest section was observed around the upper part of the tube along the P1 direction. However, by moving towards the bottom section of the tube, the thickness decreased along the P2 direction. This result could be attributed to a non-uniform distribution of hydrostatic pressure along the inner surface of the tube (Figure 5.17). To explain in detail, the upper section of the tube along path P1 experienced a negative hydrostatic pressure during ECAE, leading to an accumulation of material within this region. On the contrary, the bottom section of the tube continuously experienced a positive hydrostatic pressure as the punch reached higher strokes, leading to tube thinning along the P2 direction. Numerical measurements indicated a variation in uniform thickness along the P3 and P4 directions with a 1.5 mm minimum wall thickness difference between the as-received and ECAE treated tubes for both cases.

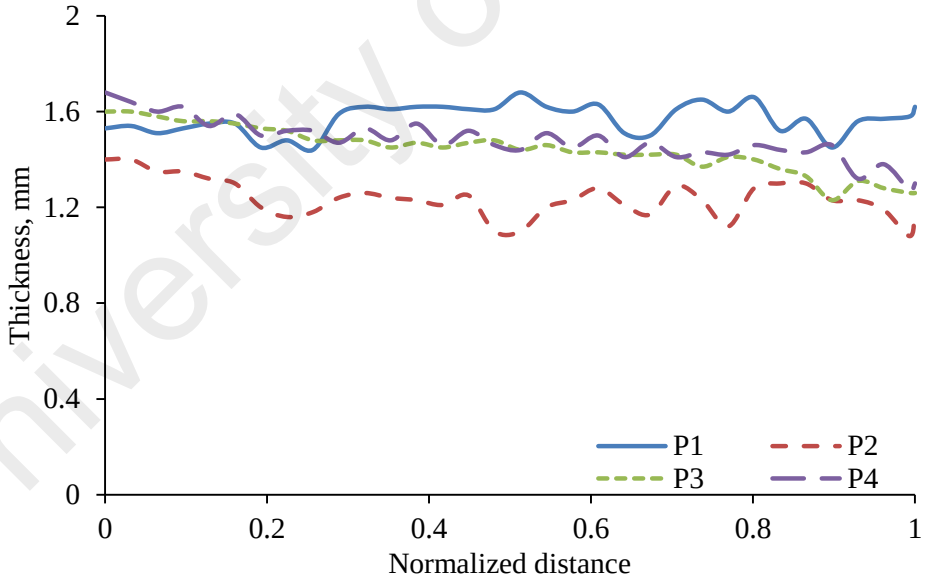

Figure 5.18: Numerical thickness distributions along the longitudinal direction for paths P1-P4

Figure 5.19 presents the overall view of the ECAE-treated tubular workpiece in addition to cross-sectional views for three different sections. Variations in wall thickness and diameter of the ECAE-treated tubes were measured and summarized in Table 5.1. As the results showed, the tube diameters (D_1 and D_2) remained constant without exhibiting

ovality after ECAE. Furthermore, thickness measurements in the horizontal direction (t_1 and t_2) signified an insignificant reduction in tube wall thickness. However, a thickening of the tube wall thickness was observed in the upper section of the tube (t_3), reaching up to 0.15 mm in section C-C'. The lower sectional tube measurements were indicative of a thinning phenomenon resulting from an excessive plastic upflow of material, exhibiting a ~0.2 mm reduction in wall thickness (t_4). These variations in tube thickness which were in accordance with the FEA outputs (Figure 5.18) explained the observation of a slight degree of tube ovality and eccentricity.

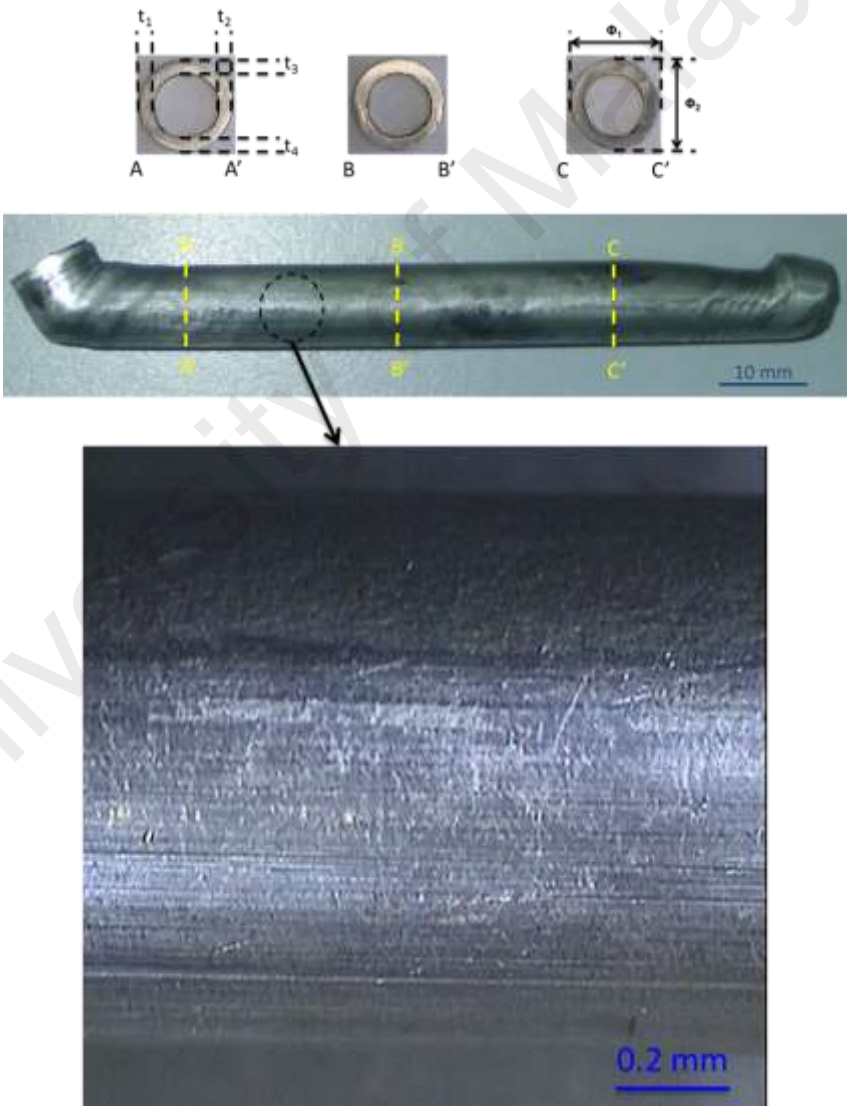

Figure 5.19: An overall view of the ECAE-treated tubular workpiece in addition to cross-sectional views of the three different sections and surface magnified view

Table 5.1: Dimensions (in mm) of the sections shown in Figure 5.19

		t_1	t_2	t_3	t_4	D_1	D_2
Experimental	A-A'	1.46	1.43	1.55	1.35	10.03	10.09
	B-B'	1.49	1.49	1.54	1.44	10.16	10.05
	C-C'	1.59	1.57	1.65	1.30	10.15	10.02
Numerical	A-A'	1.62	1.6	1.6	1.43	9.78	9.91
	B-B'	1.58	1.55	1.65	1.32	9.88	9.72
	C-C'	1.54	1.54	1.63	1.25	9.31	9.56

5.3.1.3. Plastic instability

The onset of plastic instability ($d\sigma/d\varepsilon = \sigma$) in tubular AA6061 was studied in order to characterize the probability of tube fracture during the ECAE process. Machining errors due to precision limitations, excessive friction between the tube and channel die, structural inhomogeneity of materials, and unfit sealing of the tube and screw may result in the leakage of hydraulic oil, which could lead to the initiation of cracks, crack propagation, and eventually failure. Figure 5.20 shows some examples of successful and failed tubular workpieces.

Figure 5.20: (a) Successful and (b) failed ECAE-treated tubes

Comparison of EPS versus stress triaxiality according to equation (4-8) is used in order to predict the possibility of ductile fracture. EPS and stress triaxiality (η) values were

plotted with respect to punch displacement, as illustrated in Figure 5.21. Accordingly, tube failure occurred if the stress triaxiality value exceeded the fracture strain ($\bar{\varepsilon}_f$) during the punch stroke.

As evident from Figure 5.21, tube stress triaxiality (η) increased during the onset of the process due to static friction conditions and the formation of a dead zone reaching a maximum value of almost 0.11 at a punch displacement of 12 mm, with a relative EPS of ~0.12. However, the value of EPS was considerably less than expected based on the uniaxial tension fracture criterion ($n = 0.2 > \bar{\varepsilon}$). At a punch displacement of 18 mm, the stress triaxiality value decreased down to zero, and became negative as the process continued, providing a safe condition during the ECAE process.

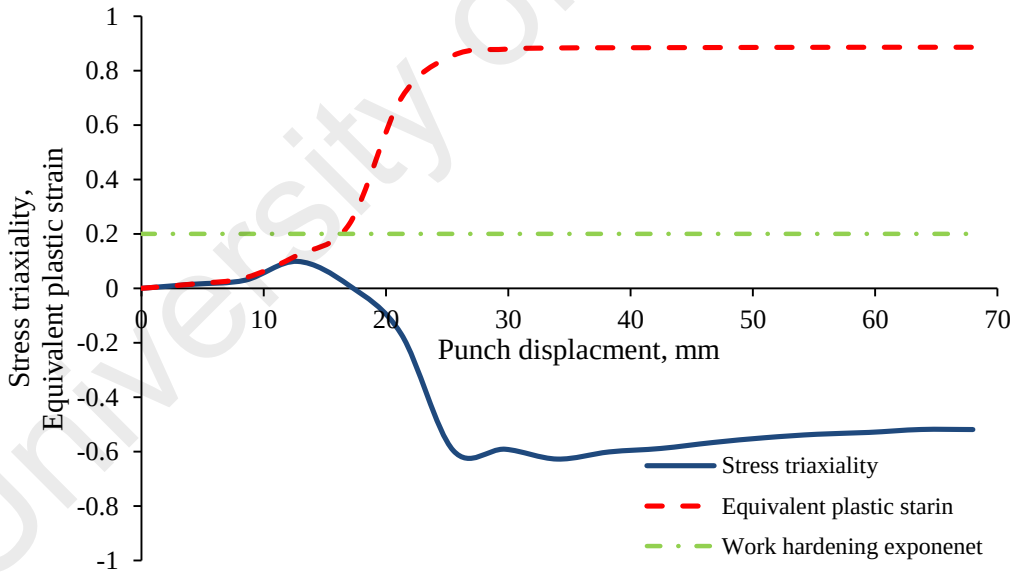

Figure 5.21: Calculated equivalent plastic strain (EPS) and stress triaxiality versus punch displacement at the point of crack initiation as predicted from FEA-simulation

5.3.2. Microstructure analysis

The microstructure and grain size distribution of various samples are illustrated in Figure 5.22. The microstructure of the as-received AA 6061-O (Sample 1) with deformation free grains as a result of annealing and an average grain size of 75.8 µm

can be seen in Figure 5.22(a). The coarse grains were homogeneously distributed in the extrusion direction (ED) and normal direction (ND) with relatively equiaxed structures. Moreover, from an analysis of grain size in Figure 5.22(b), the existence of a few grains with a diameter of 240 μm and some finer grains (20 μm in diameter) were apparent. However, the majority of the grains appeared to be in the size range of 40 μm to 120 μm.

Figure 5.22(c) shows the microstructure evolution of the tubular workpiece after a single ECAE pass. As seen in Figure 5.22, the sample microstructure was remarkably different from the as-received workpiece due to the appearance of fine grains resembling a lamellar (or irregularly bent lamellar) morphology which were elongated in the shear direction, indicating that the imposed plastic strain led to a significant grain refinement in the AA 6061 structure after one cycle. Image processing results obtained from the ECAE-treated sample (Figure 5.22(d)) revealed a mean grain diameter of 29.65 μm with the majority of grains being in the size range of 20 μm to 45 μm, showing a significant grain size reduction of 60% compared to the as-received workpiece.

Furthermore, the microstructure of the workpiece following double-treatment (ECAE + heat treatment) can be seen in Figure 5.22(e). As a result of the heat treatment (T6) following ECAE, an overall increase in the mean grain diameter was observed and accompanied by a morphological conversion from elongated to equiaxed shapes, which could be attributed to in situ recovery processes (Pouraliakbar et al., 2014). Moreover, the T6 heat treatment process resulted in the formation of homogeneous microstructures in the double-treated workpiece with an average grain size of 39.35 μm (Figure 5.22(f)). The T6 heat treatment was a three stage process and included the dissolution of soluble phases via annealing at 520 °C for 1 hour, the development of supersaturated microstructures via quenching immediately after annealing, and the precipitation of

solute atoms as a result of artificial age hardening (heating for 7 hours at 170 °C). The first stage of the T6 process provided a possibility for the formation of mixed grains with various sizes (small sized grains in particular) and yielding recrystallized microstructures with newly formed grain boundaries. As a result of quenching (stage 2 in the T6 process), small-sized nucleated grains were surrounded by coarse grains which could contribute to the formation of bimodal microstructures. Due to this particular microstructure, the final material was able to simultaneously exhibit specific mechanical properties such as high ductility and strength (Tellkamp et al., 2001; Wang et al., 2002).

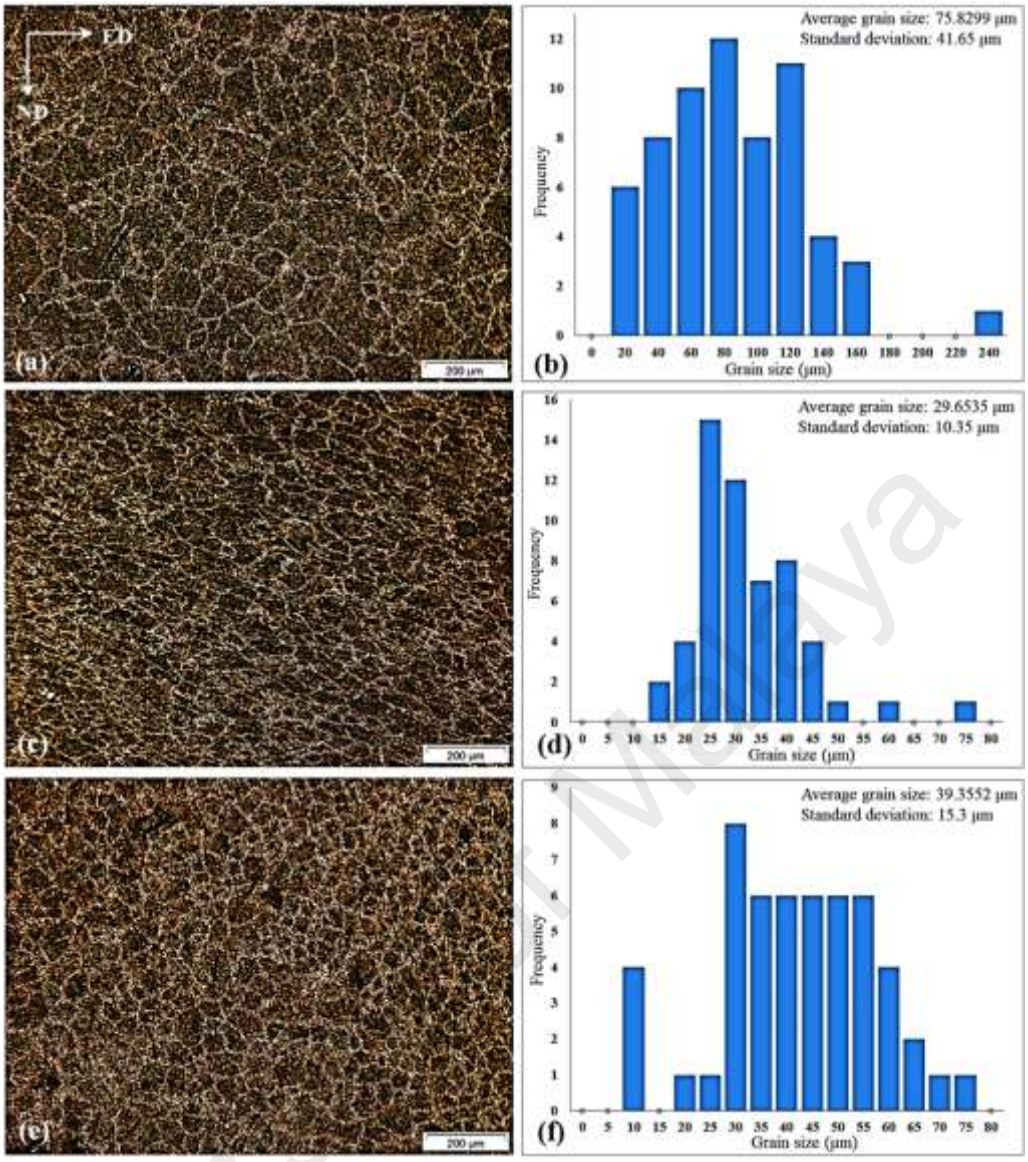

Figure 5.22: Optical micrographs and grain size distributions obtained from quantitative image analysis for (a, b) Sample 1 (as received), (c, d) Sample 2 (ECAE-treated), and (e, f) Sample 3 (double-treated)

5.3.3. Mechanical properties

5.3.3.1. Torsion test

Shear stress-strain curves resulting from the torsion test can be seen in Figure 5.23. In the ECAE process, grains were refined due to extreme EPS imposed on the tube. Newly-formed fine grains with small sizes increased the grain boundary density, which could serve as an impeding factor to effectively resist the propagation of dislocations, causing a remarkable improvement in the strength of the workpiece considering the

Hall-Petch equation (Dunstan & Bushby, 2014). As seen in Figure 5.23, the yield shear strength and ultimate shear strength of the ECAE-treated workpiece improved considerably by factors of ~2.5 and ~1.4, respectively, in comparison with the as-received workpiece. In the case of the double-treated workpiece, further progress was observed with regard to the yield shear strength and ultimate shear strength by factors of ~1.1 and ~1.3 compared to the ECAE-treated workpiece, respectively. On the other hand, research findings related to ductility after the SPD process were rather contradictory. Some researchers observed an enhanced ductility after SPD due to a combination of UFG effects and the formation of high-angle grain boundaries (Valiev et al., 2002). However, another study showed that the SPD process reduced ductility due to a strong localization of strain (Estrin & Vinogradov, 2010). The torsion test results in the current study indicated that the ECAE process imparted a detrimental effect on ductility (ultimate twist at rupture) compared to the as-received workpiece. The results also showed that heat treatment after ECAE eliminated the negative effect of ECAE processing on ductility. A notable improvement in the ductility of ECAE-treated AA 6061-O could be obtained by performing a post heat treatment process.

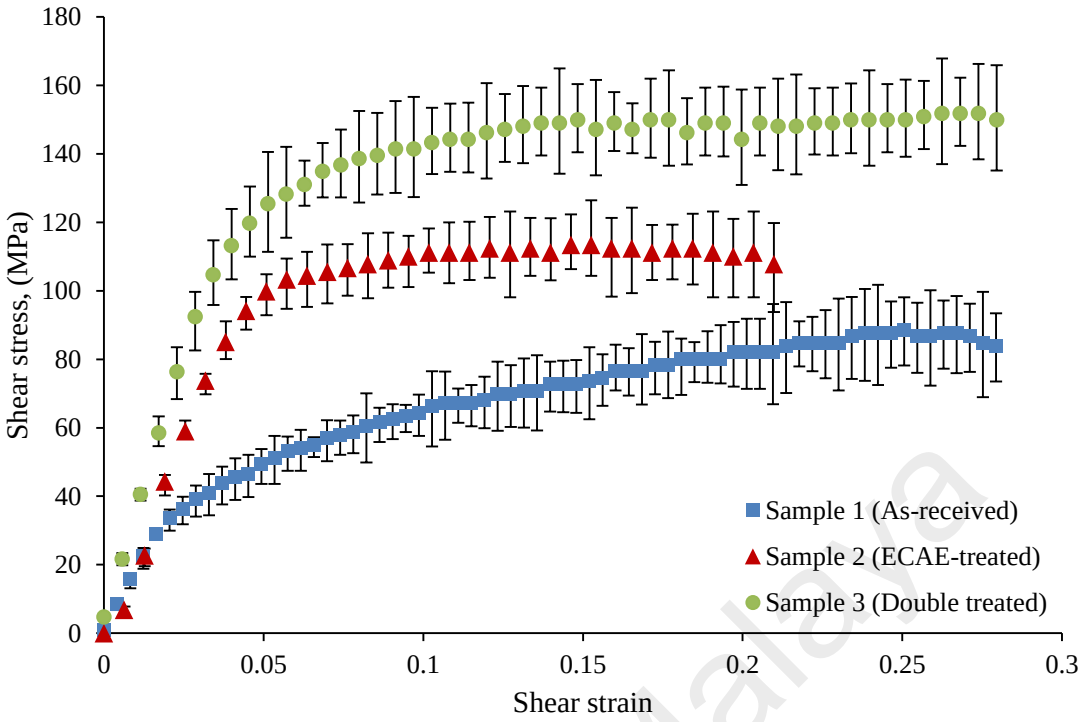

Figure 5.23: Shear stress-strain curves at room temperature for the as-received, ECAE-treated, and double-treated (ECAE + heat treated) workpieces after one ECAE pass

Visual examination of the failed samples at low and high magnifications was performed to assess the material ductility and morphology of the fractured surfaces. According to the results, the fractured sections could be classified into three categories: cross sections with ductile fractures, cross sections with brittle fractures, and fractured regions characterized by thin tube-wall buckling. To explain in detail, ductile fractures occurred due to a maximum exertion of shear stress (τ_{max}) at a plane perpendicular to the longitudinal axis (tube axis), whereas brittle fractures occurred due to a maximum exertion of tensile stress ($\sigma_1 = \tau_{max}$) at a plane with a 45° offset from the longitudinal axis, typically resulting in fractured sections with helicoid morphologies. The third failure mode observed after torsional testing was buckling, which occurred in the thin walls of tubular components due to membrane shear stress (Schmidt & Winterstetter, 2004).

The failed workpieces after torsional testing can be seen in Figure 5.24. Failure in the as-received workpiece occurred due to premature buckling prior to crack formation. It

was deduced that premature buckling occurred due to the simultaneous effect of high ductility and low yield strength. At high magnification, rough surfaces with an array of successive dimples and voids were visible, characteristic of ductile fractures (Figure 5.24(a)). Similar failure modes have been reported in prior research studies in the case of tubular components made from aluminum and steel (Winterstetter & Schmidt, 1999). However, the failed section of the ECAE-treated tube (Figure 5.24(b)) provided evidence for a reduction in material ductility compared to the as-received workpiece with a 45^{o} inclined fracture plane. SEM micrographs confirmed the same morphology at the micro scale by revealing features such as scaled slabs, river patterns, striations, and cracks. The failed sections of the double-treated workpiece (Figure 5.24(c)) represented a mixed failure mode by showing traces of both ductile and brittle fracture. In this workpiece, the onset of crack nucleation occurred within highly distorted zones as a result of strain localization imposed by tube buckling. Correspondingly, under high magnification, the simultaneous emergence of ductile and brittle fractures became apparent.

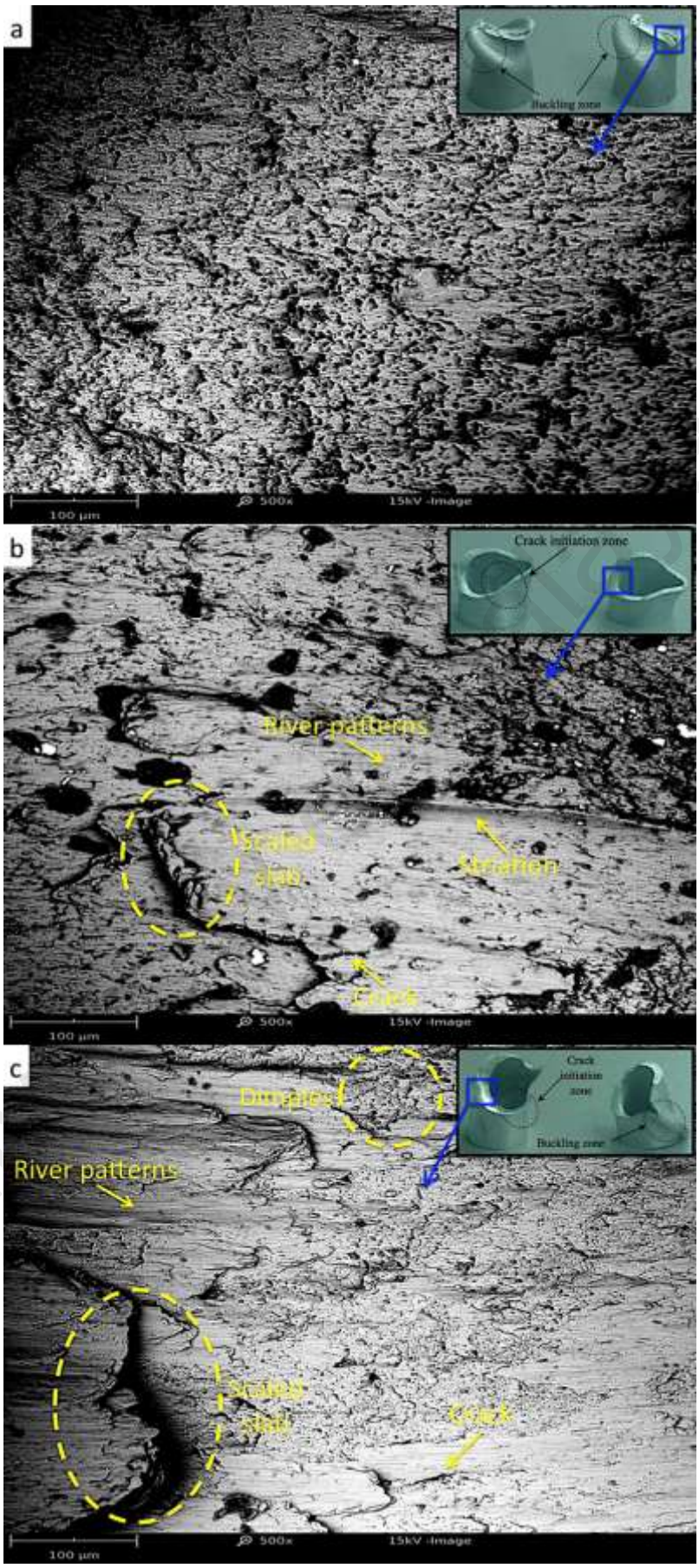

Figure 5.24: Overview and magnified micrographs of failed samples for the (a) as-received, (b) ECAE-treated, and (c) double-treated (ECAE + heat treated) workpieces

5.3.3.2. Hardness

Figure 5.25(a-c) reveal the micro hardness indentation examples for the as-received, ECAE-treated, and double-treated sample workpieces, respectively. It was evident that the size of the indentation left on the as-received workpiece was significantly larger than the indentation left on the ECAE-treated and double-treated workpieces. However, a comparison between Figure 5.25(b) and Figure 5.25(c) revealed a slight decrease in the indentation size as a result of heat treating after the ECAE process.

Hardness as a function of material strength and ductility was associated with grain size according to the Hall-Petch equation (Dunstan & Bushby, 2014). Based on the results reported in the literature (Malow & Koch, 1998), distortion of the indentation outline, characterized by material pile-up around the indentation, could be used as a basis for comparison between the average grain size of a workpiece.

Figure 5.25(a) shows the Vickers indentation outline for the as-received sample. In this case, considerable material pile-up and ridging formed around the indentation boundary. Barreling effects as a result of these phenomena were observed for this workpiece, which could be associated with the coarse grain structure of the as-received material.

It could be clearly seen from Figure 5.25(b) that the barreling effect disappeared from the ECAE-treated workpiece due to grain refinement. This phenomenon confirmed the decrease in material ductility following ECAE processing as well.

In the case of the double-treated workpiece, due to the T6 heat treatment process (recrystallization and evolution of equiaxed structures) resulting in a slight ductile recovery of the ECAE-treated workpiece, traces of the barreling effect could be observed around the indentations as seen in Figure 5.25(c).

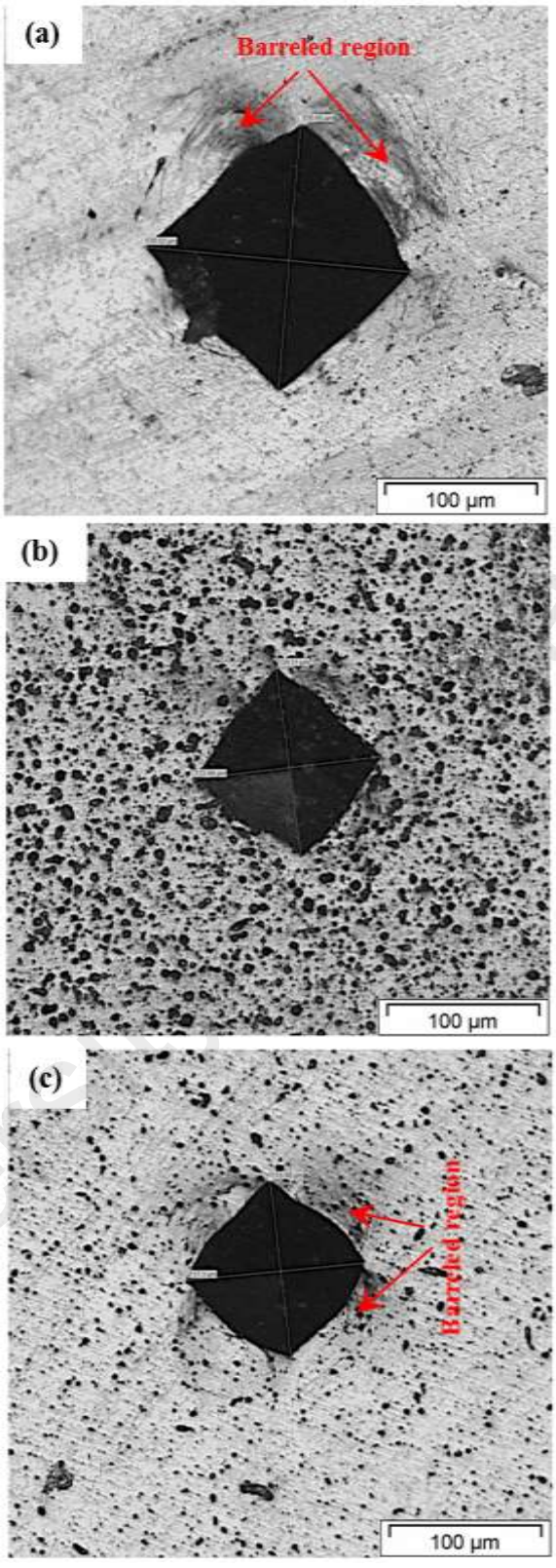

Figure 5.25: Optical images of indentations left on (a) as-received, (b) ECAE-treated, and (c) double-treated (ECAE and heat-treated) workpieces

Due to moderate microstructural in-homogeneities represented by the standard deviation of the grain size analysis (Figure 5.22), slight variations in hardness values were

observed at different points of the various samples according to their radial position. From Figure 5.26, inconsistent variations in hardness values without a specific trend were evident in the case of the as-received workpiece, which was in accordance with the extended range of the grain size analysis standard deviation reported in Figure 5.22(b). Although the hardness values exhibited a slight increasing trend toward the exterior sides in the case of the ECAE-treated and double-treated workpieces, all values were within a reasonably narrow range, indicating a significant structural homogeneity enhancement after ECAE and heat treating.

From the average of the hardness values, it was evident that the mean hardness of the as-received AA6061-O (60 HV) sample improved by a factor of ~2.1 after the ECAE-treatment process (128 HV). The heat treated samples after ECAE processing (133 HV) revealed further improvements with regard to the mean hardness value by a factor of ~1.04 compared to the workpieces treated only by ECAE.

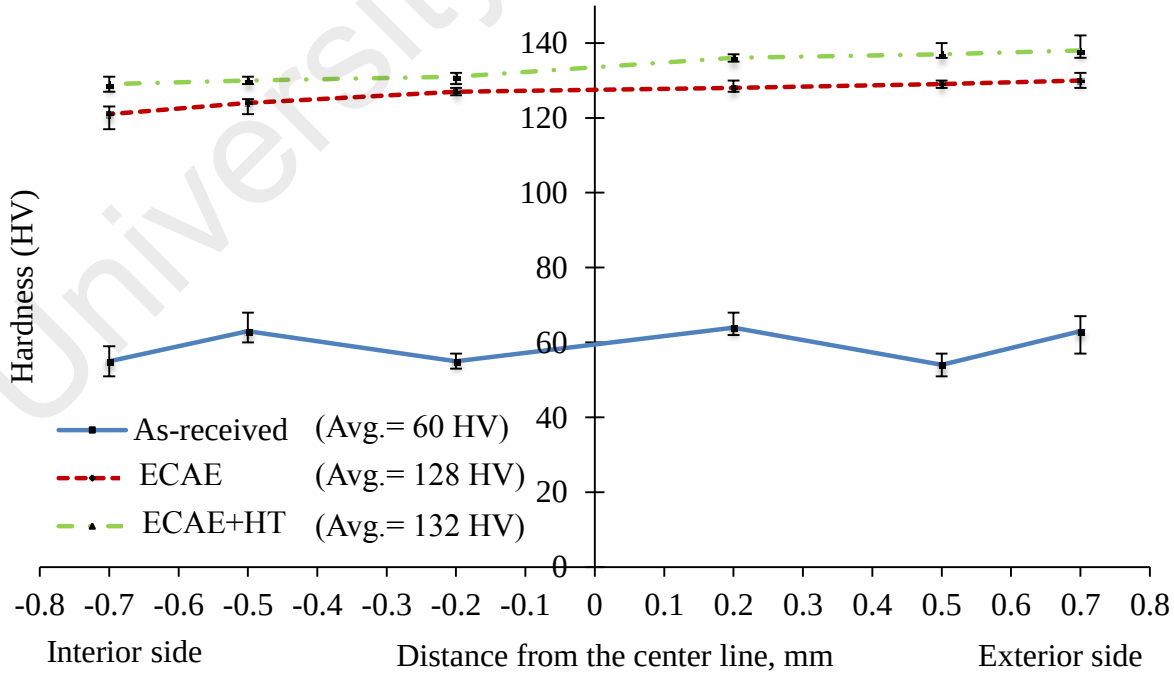

Figure 5.26: Micro hardness values along the tube wall thickness for the as-received, ECAE-treated, and double-treated (ECAE+HT) samples

5.4. Dissimilar joining of AA6061-O and Mild steel using ECAE

5.4.1. FE-simulation results

The distribution of EPS as one of the FEA outputs was used to evaluate the SPD process capability to produce components with ultra-fine grain structures. In this regard, ECAE can refine workpiece grains more effectively if higher amounts of accumulated EPS are imposed (Li et al., 2004).

Figure 5.27 shows the EPS distribution throughout the entire workpiece (Figure 5.27(a)), aluminum alloy sheath (Figure 5.27(b)), interlayer (Figure 5.27(c)) and steel core (Figure 5.27(d)) when the ECAE joining analysis was performed under the FEA conditions. The FEA output showed that the equivalent stress (von-Mises stress) reaches the highest value while the workpiece passes through the die's abrupt angle. This value for aluminum sheath, interlayer and steel core is 124, 92.7 and 330 MPa, respectively. The contour plots in Figure 5.27 signify that this joining method imposes high amount of accumulated EPS after only one pressing cycle. The equation (2-20) estimated EPS of ~1.03. This inconsistency between the EPS values from FEA and the analytical equation is originated from the different mechanical properties and geometries of the components, friction effect and strain in-homogeneity.

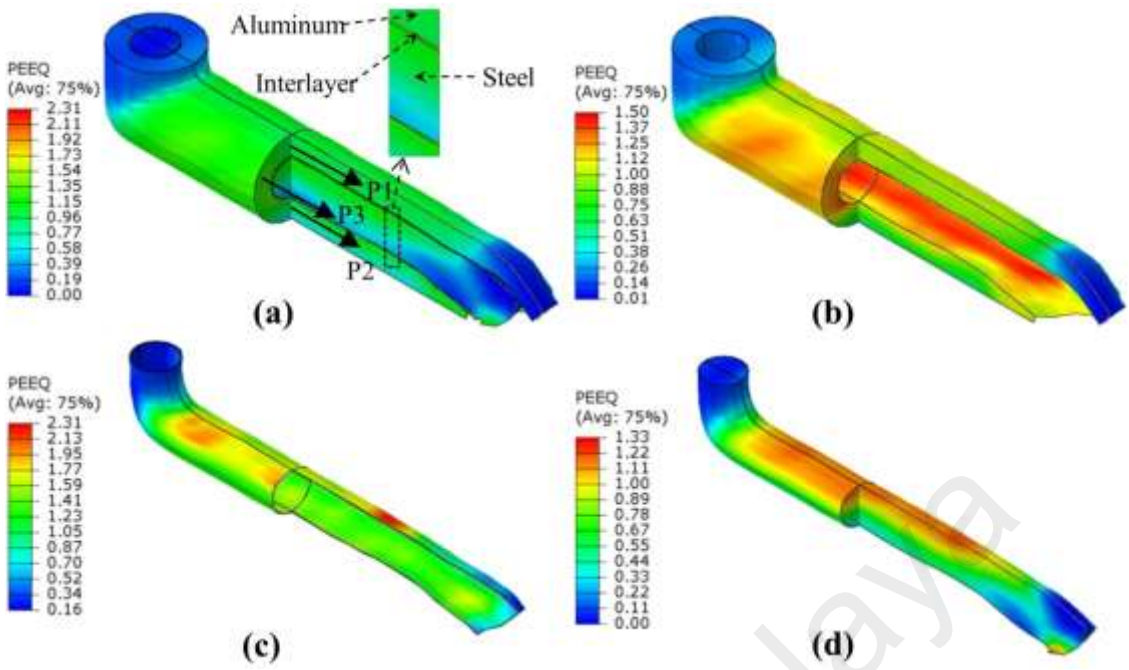

Figure 5.27: Distribution of equivalent plastic strain (EPS) during the ECAE joining for (a) final workpiece, (b) aluminum sheath, (c) interlayer and (d) steel core

In order to quantify the strain homogeneity for each component individually following the ECAE joining process, the EPS was analyzed in three longitudinal directions, namely the areas in contact with the die's corner angle (P1), channel angle (P2) and die's middle section (P3) (Figure 5.27(a)).

Figure 5.28 shows the distribution of accumulated EPS along the longitudinal directions for various constituent components of the final workpiece. According to this figure, moderate inhomogeneity over the aluminum sheath and the EPS reached a maximum value along the P3 direction, whereas the amount of EPS was almost equal for the other two directions (P2 and P3). In the case of the interlayer, the amount of accumulated EPS was higher than aluminum sheath and steel core for all three directions. This notably high EPS value can be attributed to the significant pressure imposed on the interlayer by the aluminum sheath and steel core during the ECAE joining process in addition to the low interlayer foil thickness. The accumulation of such a considerable amount of EPS plays a significant role in workpiece grain refinement, which is a potential factor in improving the bonding strength between the steel core and aluminum sheath. On the

contrary, the least amount of EPS was imposed on the steel core during joining compared with the other two components.

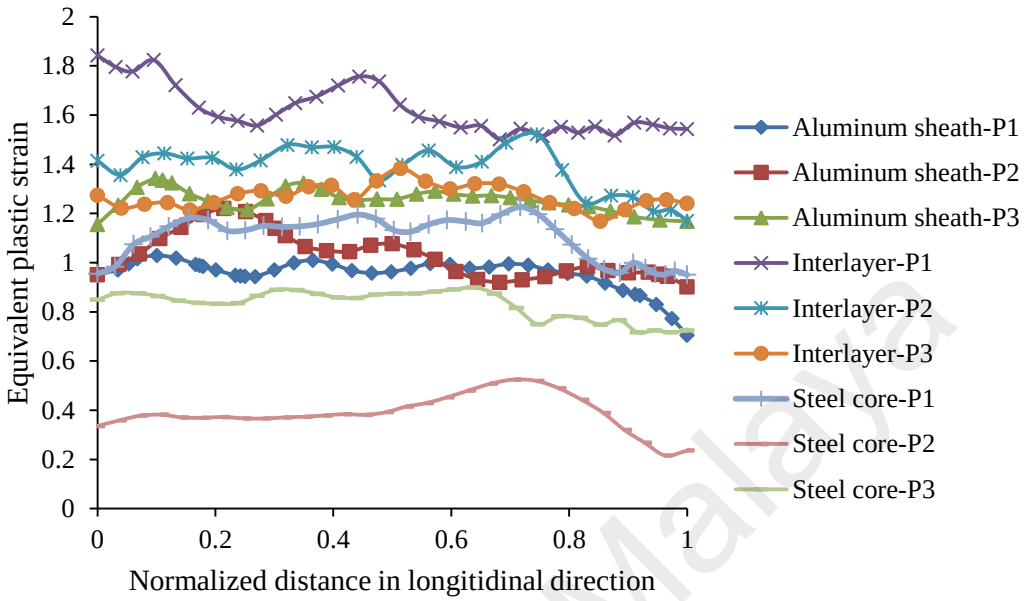

Figure 5.28: Distribution of EPS in the longitudinal direction of the aluminum sheath, interlayer and steel core

It is well-established that microstructural homogeneity plays an important role in joining with some degree of diffusion. Moreover, microstructural homogeneity and hardness uniformity are proportional to EPS homogeneity, which is imposed on the workpiece during the SPD process (Xu et al., 2007).

To investigate the degree of homogeneity, a path along the workpiece diameter was considered to analyze the distribution of EPS after ECAE joining and microhardness ratio (h/h_0) after ECAE joining and annealing process. The microhardness ratio was calculated by dividing the hardness value after the ECAE joining and post-ECAE annealing to initial hardness values. The initial values of hardness for aluminum sheath, interlayer and steel core measured as 60, 110 and 210 HV. As can be seen from Figure 5.29, the EPS for aluminum sheath reaches to its maximum value at the region which is in contact with interlayer. Accordingly, the hardness ratio also confirms this observed trend in EPS. Higher amount of accumulated EPS in aluminum inner sheath can

improve the joint strength; however it imposes inhomogeneity in final product. In case of interlayer, the EPS shows higher values compared with aluminum alloy and steel components. Moreover, the hardness ratio for interlayer represents the maximum homogeneity amongst the joint components. This can be related to significantly lower thickness of interlayer compared with the other two components. Contrary, the minimum accumulation of EPS was observed for steel core which is in good accordance with results reported by Bowen et al. (Bowen et al., 2000). Furthermore, the capability of annealing process in reducing the joint components' inhomogeneity is evident in Figure 5.29 as indicated by the hardness ratio trend.

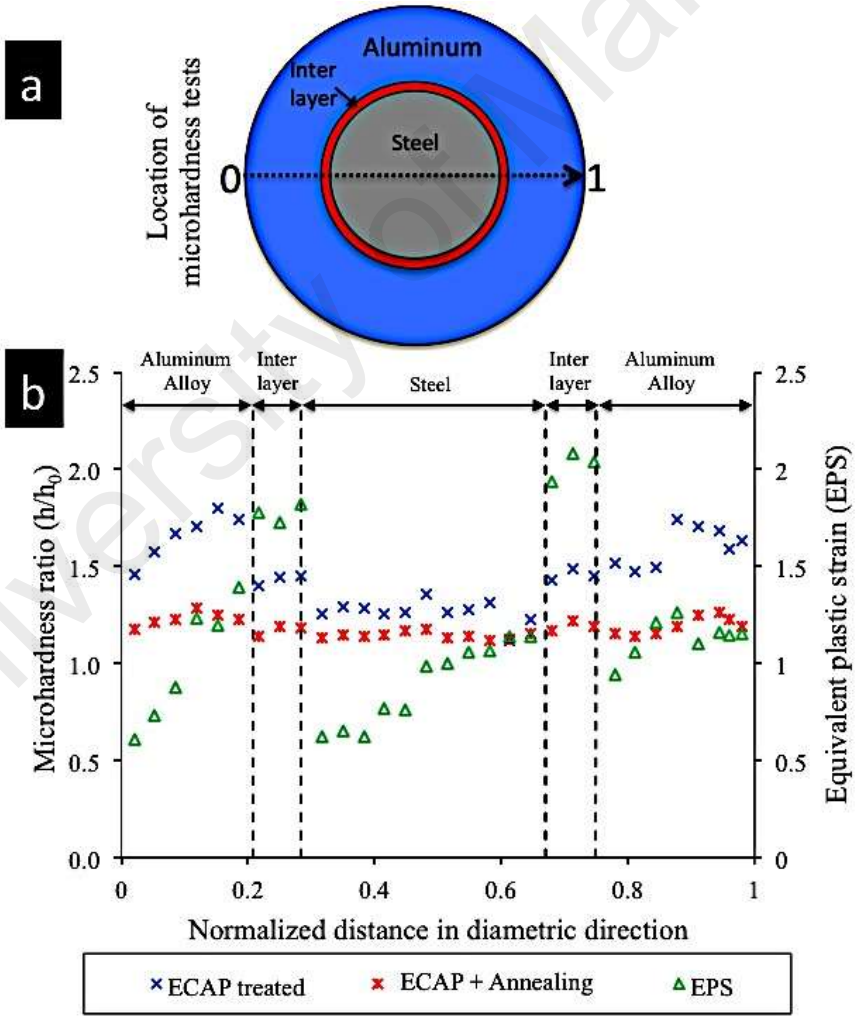

Figure 5.29: (a) Schematic view of indentations' location along the diametric direction across the workpiece surface and (b) the microhardness ratio for ECAE-treated and double treated workpieces, and EPS distribution for ECAE-treated workpiece

5.4.2. ECAE joining final component

The overall and cross sectional views of the workpiece produced through ECAE joining are depicted in Figure 5.30. The visual features of the final product demonstrate the soundness of the joint with no serious macro-scale defects.

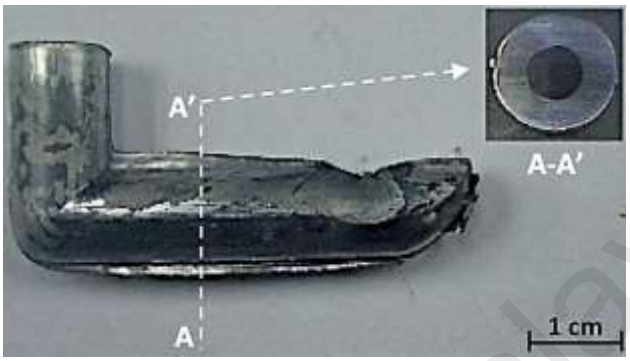

Figure 5.30: Overall and cross sectional views of the workpiece after ECAE joining

5.4.3. Microstructural evolution

It is well-established that the main function of all SPD processes is to refine the material's microstructure through reducing the mean grain size. In this regard, the microstructure of the materials prior to and after ECAE joining was observed with an optical microscope.

To investigate the degree of grain refinement after ECAE joining, image processing software (Image J 1.47v, Wayne Rasband National Institute of Health, USA) was utilized to measure the mean grain size of the as-received components and the joined workpieces following the ECAE process.

Figure 5.31(a) represents the microstructure of as-received AA 6061-O (sheath), which contains coarse, deformation-free grains as a result of annealing with average grain size of approximately 73.21 μm. Evidently, the coarse grains are distributed homogeneously in the extrusion direction (ED) and normal direction (ND) with relatively equiaxed structure. However, as seen in Figure 5.31(b), the microstructure of aluminum sheath after ECAE joining differs from the as-received workpiece owing to the appearance of

finer grains with average size of 41.68 µm. This microstructure resemble lamellar (or irregularly bent lamellar) morphology and are elongated in the shear direction. This observation is in good accordance with literature (Wei et al., 2011) which shows that the ECAE is effective even after only one cycle.

Correspondingly, the steel core's microstructure prior to ECAE joining represents shear bands that are distributed homogeneously in all directions (Figure 5.31(c)). However, as a result of ECAE joining, the dislocation density increased, which led to the formation of finer equiaxed grains with continuous boundaries and mean size of 16.46 µm (Figure 5.31(d)). By comparing the extent of grain refinement after joining, it can be concluded that the ECAE joining process was more effective on the aluminum sheath, which showed nearly 40% reductions in mean grain size. This outcome is in good accordance with the EPS distribution calculated by FEA as explained earlier.

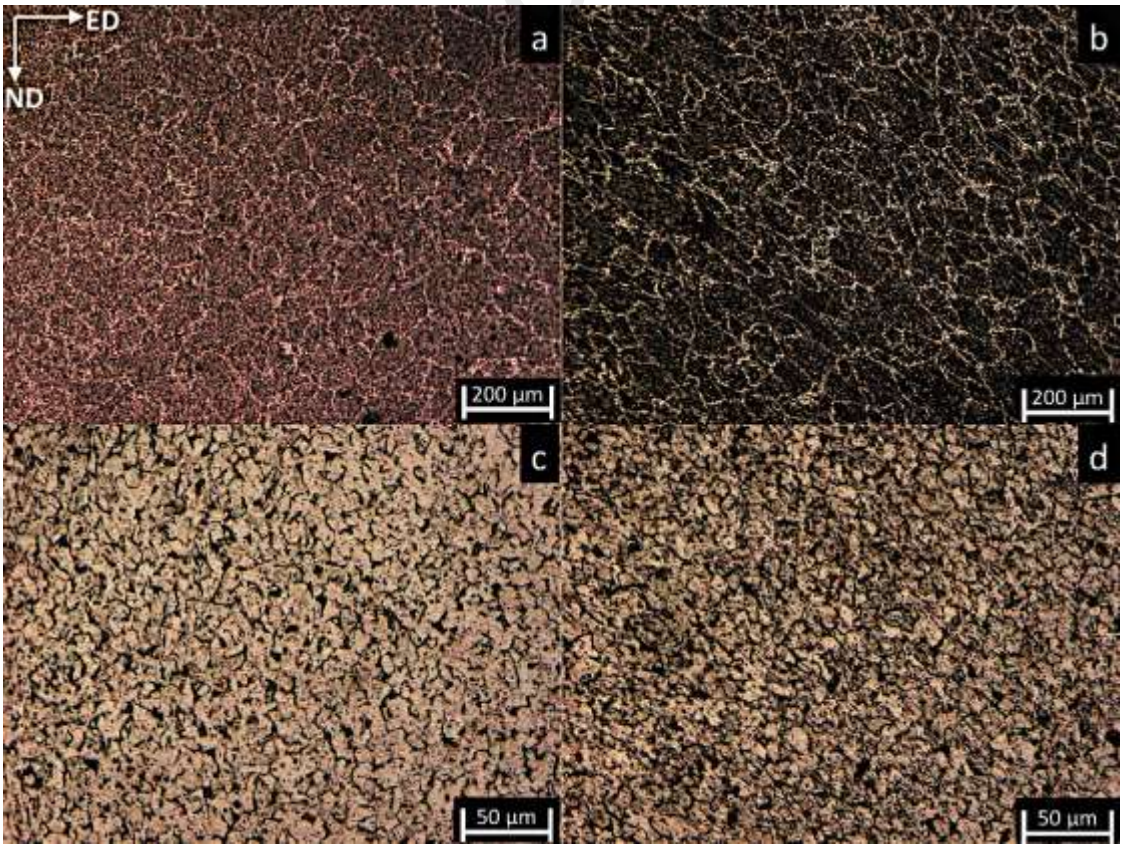

Figure 5.31: Aluminum alloy microstructure (a) before ECAE, (b) after ECAE, and steel (c) before ECAE and (d) after ECAE

It is well known that the SPD-treated materials are susceptible to intergranular fracture due to the strain localization and stress concentration in grain boundaries. The possibility of this type of fracture increases when materials with ultra-fine microstructure are subjected to high strain rate at elevated temperature (Csontos & Starke, 2005; Farkas et al., 2002). The observation of intergranular cracks for ECAE treated aluminum alloy during the tensile test at strain of ~ 8 and strain rate of 10^{-1} s^{-1} when the temperature is 637 K was reported (Lee et al., 1999). Moreover, it is reported that aluminum alloys with Mg content of higher than 3% are more sensitive to intergranular corrosion (Zander et al., 2015). However, the low amount of magnesium content in the aluminum alloy used in the current study (~0.4%), the risk of stress corrosion decreases upon temperature rise. Occurrence of intergranular fracture was reported in steels with high amount of Ni, Cr and Mo (Lima & Sankaré, 2014) specifically when the ratio of operating temperature to melting temperature exceeds 0.25 according to fracture map (Riedel, 2014). The effect of annealing treatment on intergranular fracture of nanocrystalline α-iron was studied and the results showed that, annealing treatment reduces dislocation emission sources and subsequently improves material ductility through strengthening the grain boundaries' resistance to intergranular failure (Tong et al., 2015). Due to small amount of alloying elements such as Cr and Ni in the steel and Mg in aluminum used in the current study, and considering the effect of post-ECAE annealing, the possibility of intergranular fracture can decrease.

5.4.4. Characterization of joint interfaces

Figure 5.32(a) and (b) illustrate typical backscattered electron images of the joints' interfaces bonded without an interlayer and annealed at 220 and 520 °C for 60 min, respectively. From Figure 5.32(a), it is clear that the interface between AA 6061 and SAE 1018 is quite straight with some jagged irregularities and lacks any interfacial reaction layer. A similar observation was reported in another research on roll-bonded

steel and aluminum alloy, whereby no change was noted at the joint's interface at post-ECAE annealing temperature of less than 400 °C (Lee et al., 2007). Moreover, the absence of any discontinuity during the transition from the aluminum side towards the steel section is a remarkable characteristic of this joint. Despite the flawless interface, a long, horizontal crack (shown with a white arrow) is visible above the joint's interface.

On the contrary, in case of a joint annealed at 520 °C (Figure 5.32(b)), a thin diffusion layer with thickness ranging from 1-4 μm was revealed between the two mating materials. The formation of such intermediate layer was predictable considering the effect of annealing at higher temperatures, which facilitate the migration of atoms from one interface to the other (Oosterkamp et al., 2004).

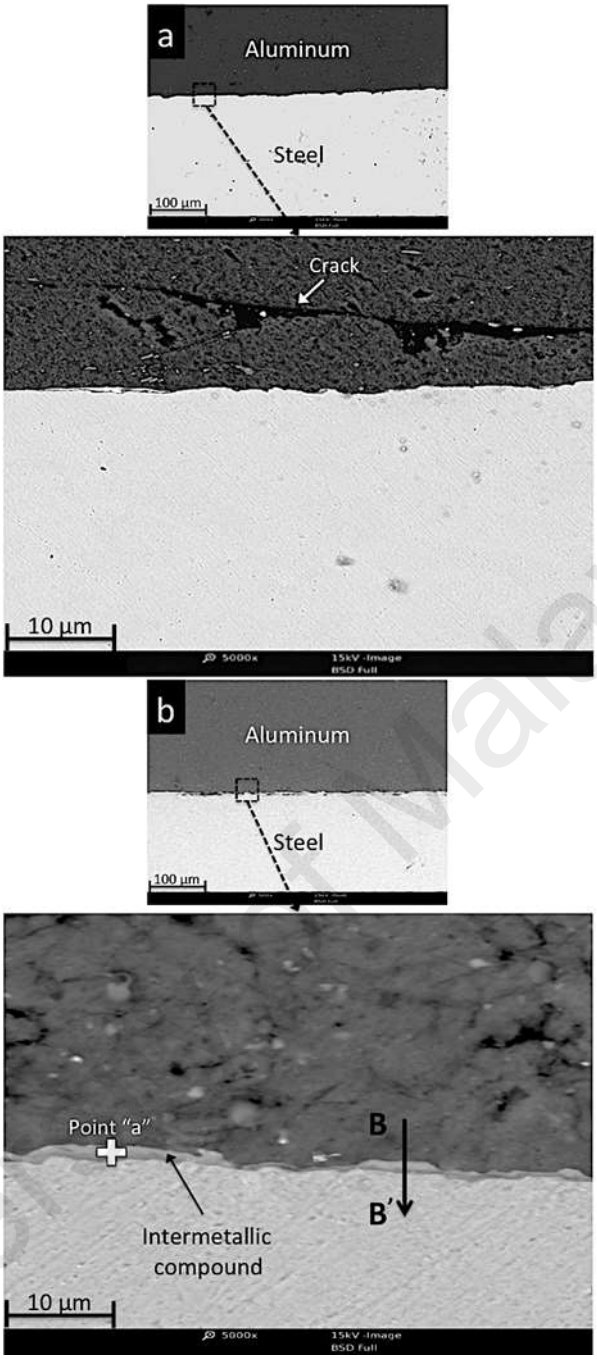

Figure 5.32: Scanning electron micrographs of ECAE joint interfaces without an interlayer after annealing at (a) 220^0C and (b) 520^0C

Figure 5.33(a) demonstrates the distribution of chemical elements detected across the bond's workpiece interface, which was annealed at 520^0C. By comparing the percentage of detected elements at the interface (Figure 5.33(b)) with the Al-Fe binary phase diagram, the intermetallic compound layer was mainly identified as Al-rich $FeAl_3$. However, it is difficult to assume this intermediate layer consists of merely a single intermetallic phase. Therefore, for the purpose of in-depth investigation, the XRD

experiment was carried out at the workpiece cross section, verifying not only the existence of $FeAl_3$ but also the formation of another Al-rich intermetallic phase with the stoichiometry of Fe_4Al_{13} (Figure 5.34).

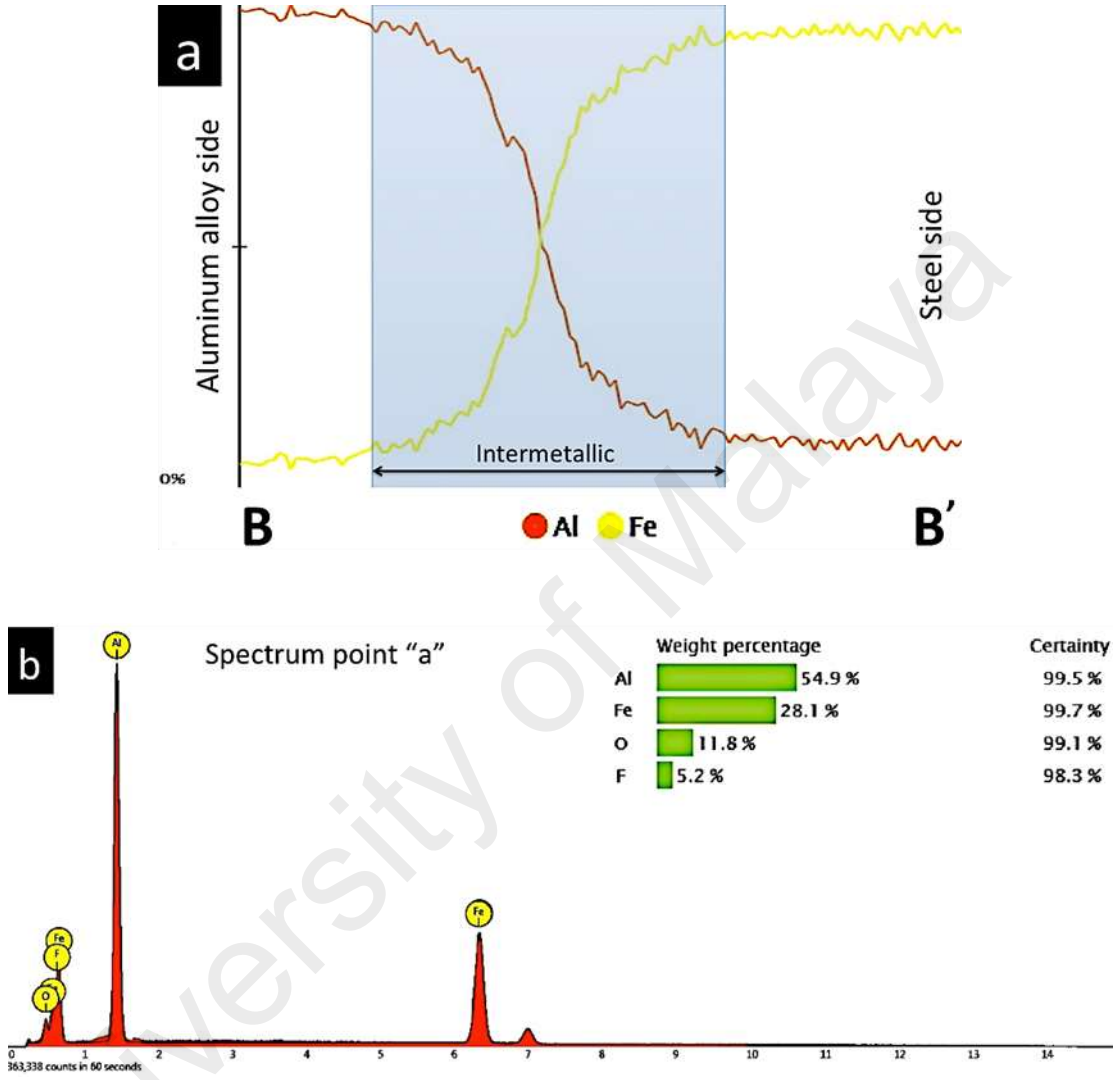

Figure 5.33: Elemental analysis of the ECAE joint interface without an interlayer after annealing at 520°C showing (a) the distribution of chemical elements across the joint's interface and (b) the composition percentage of the interface

Although Al-rich intermetallics are known for their inherent brittleness and low toughness, a visual investigation of the intermetallic layer formed between the mating materials annealed at 520 °C did not reveal any defects like internal cracks and/or segregation caused by thermal expansion coefficient mismatch in adjacent materials upon cooling. The lack of defects at the interface of this joint can be attributed mainly to the intermetallic layer thickness, which hardly reaches 4 μm even in the thickest part.

Therefore, it is much below the critical threshold of 10 μm mentioned by other researchers as a requirement for mechanically sound joints between steel and aluminum (Zhang et al., 2007).

In addition to Fe and Al, an insignificant percentage of oxygen was detected at the interface, which could have originated from remnants of thin oxide layers that formed naturally on the mating materials' surfaces. XRD analysis shows that these oxide compounds consist of various Fe_xO_y phases; however, the Fe_3O_4 phase has the highest diffraction intensity.

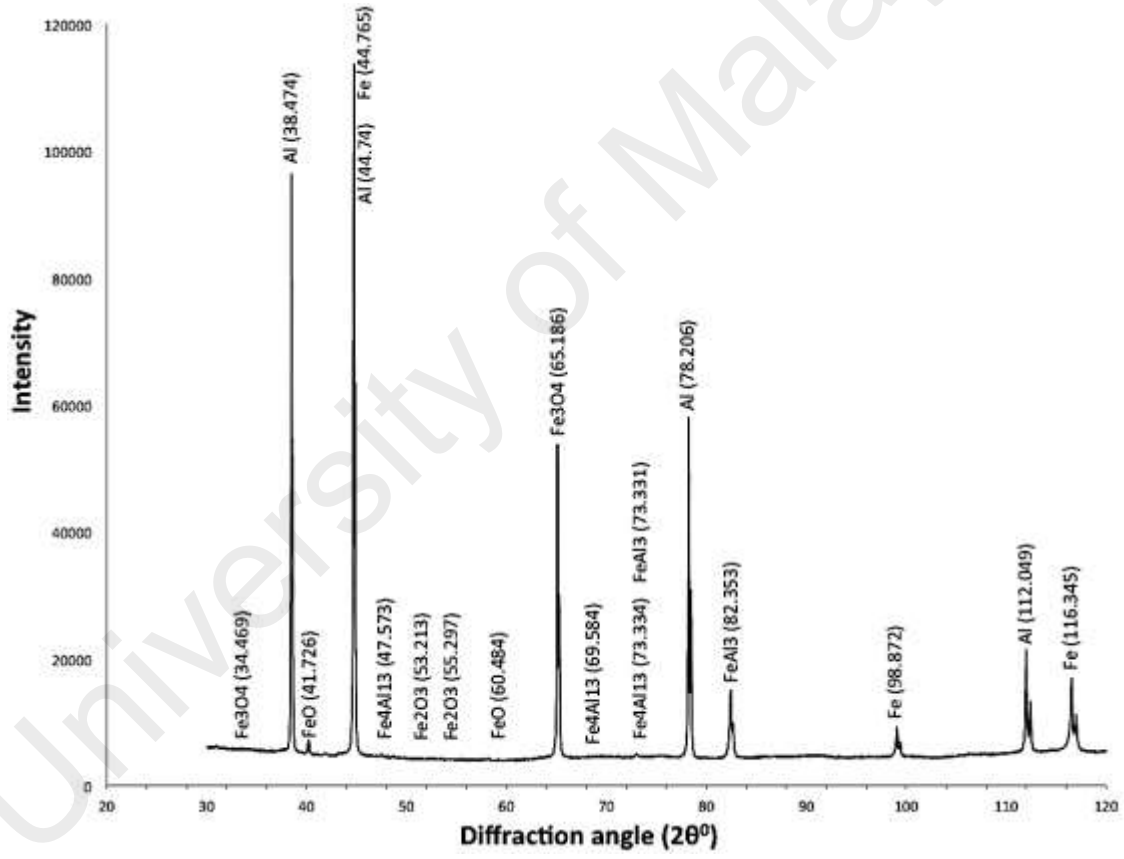

Figure 5.34: X-ray diffraction pattern obtained from the joint's interface of a workpiece without an interlayer after annealing at 520 °C

Figure 5.35 illustrates micrographs of the joints' transition zones in ECAE joints with an interlayer after annealing at 220 °C and 520 °C. In case of the joint annealed at 220 °C (Figure 5.35(a)), no distinguishable diffusion zone with additional contrast effect is observed at either of the interlayers' interfaces with the base materials. However, an

extrusion of the interlayer's fragment into the aluminum alloy sheath owing to considerable shear force exerted during ECAE is obvious at the aluminum alloy-interlayer interface and resembles a mechanical interlocking mechanism. This mechanism was found out as potential factor which can enhance the joints' bond strength significantly. Likewise, the sealed pores network observed at the steel-interlayer interface characterizes the occurrence of severe plastic deformation. The formation of interfacial pores is believed to be a consequence of surface asperities collapsing and formation of oxide particles when the mating materials were subject to severe plastic deformation while the workpiece was passing through the die's abrupt angle which results in particle entrapment at the interface (Sabetghadam et al., 2010). For this reason the interface of the steel-interlayer is completely planar, since these entrapped oxide particles can pin the grain boundaries which may cause degradation of the mechanical properties at the interface.

On the contrary, several reaction products are observed on both sides of the interlayer interface of the joint annealed at 520 ºC (Figure 5.35(b)). Notwithstanding the several pores observed in the workpiece annealed at 220 ºC, the steel-interlayer interface of the workpiece annealed at 520 ºC features a fine wavy line that lacks any major interfacial defects. Moreover, a visual investigation of the aluminum alloy-interlayer interface reveals a corrugated morphology with dominant migration of interlayer species into the highly deformed aluminum alloy. This observation is supported by the fact that in bimetallic plastic deformation bonded joints aided by diffusion, wherein the melting point and strength of one mating material are higher than the other, deformation occurs primarily on the softer material’s surface regardless of the counterpart’s configuration (Chen et al., 2007).

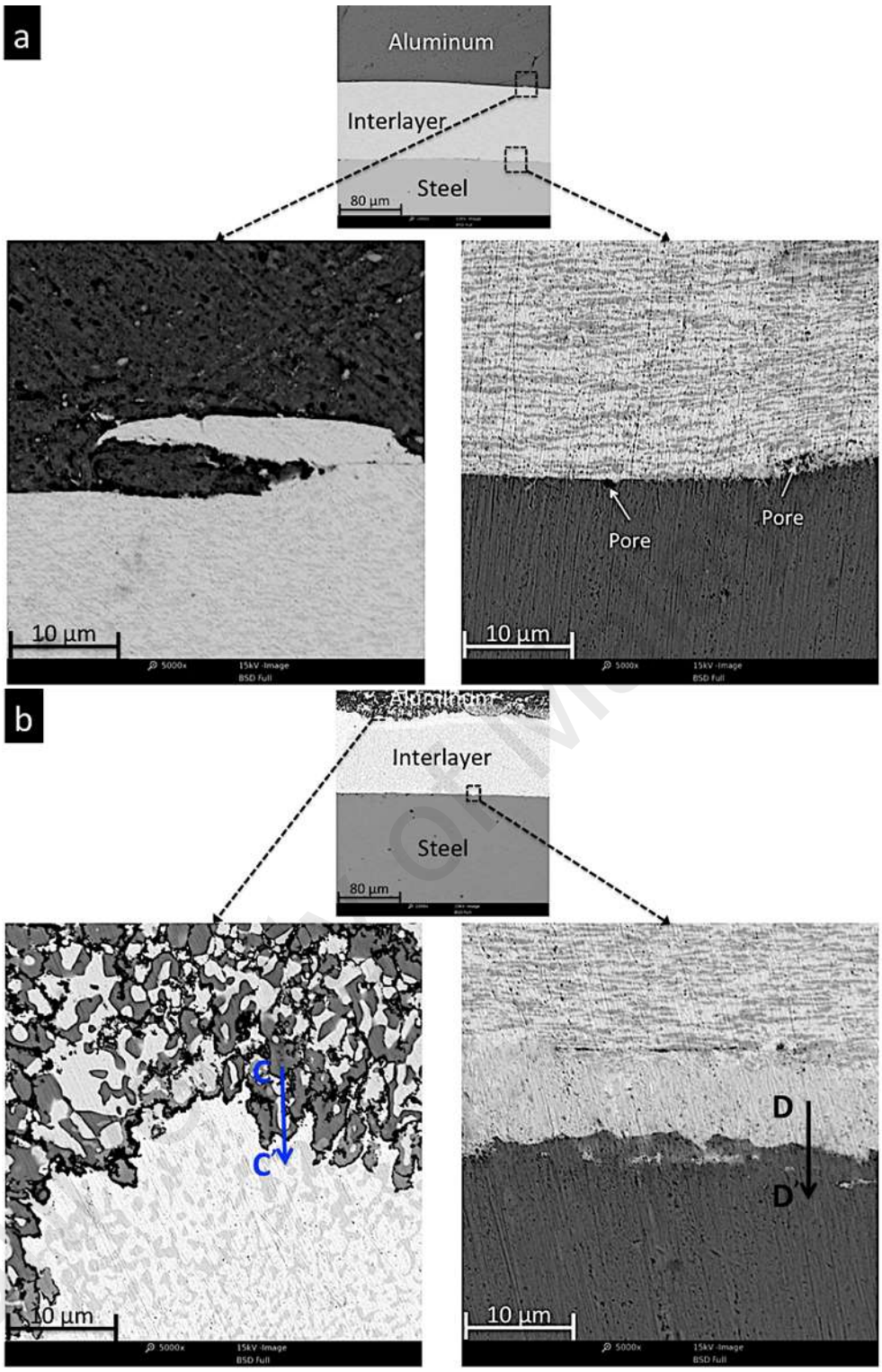

Figure 5.35: Scanning electron micrographs of ECAE joint interfaces with an interlayer after annealing at (a) 220 ºC and (b) 520 ºC

In order to realize the extent of material intermixture at the interface, the interdiffusion of Ag, Cu, Sn and Al was demonstrated through EDX line scanning for the joint annealed at 520 ºC and is shown in the concentration profiles across the C-C' and D-D' lines in Figure 5.36. According to Figure 5.36(a), the penetration curves of the chemical

species along the aluminum alloy-interlayer demonstrate a variable trend with successive fluctuations rather than a gradual and smooth transition. This indicates that joining at the aluminum alloy-interlayer interface took place not only through the metallurgical diffusion mechanism, but also through mechanical bonding. However, the penetration curves of the elements in the steel-interlayer interface (Figure 5.36(b)) signify a rather smooth and gradual transition of the chemical elements, implying the dominance of metallurgical bonding at this interface. As shown in Figure 5.36, all interlayer constituents indicate a decreasing trend upon transition from the interlayer to the adjacent materials; however, copper exhibits a decreasing trend after an abrupt growth at the interface, indicating the significant accumulation of copper.

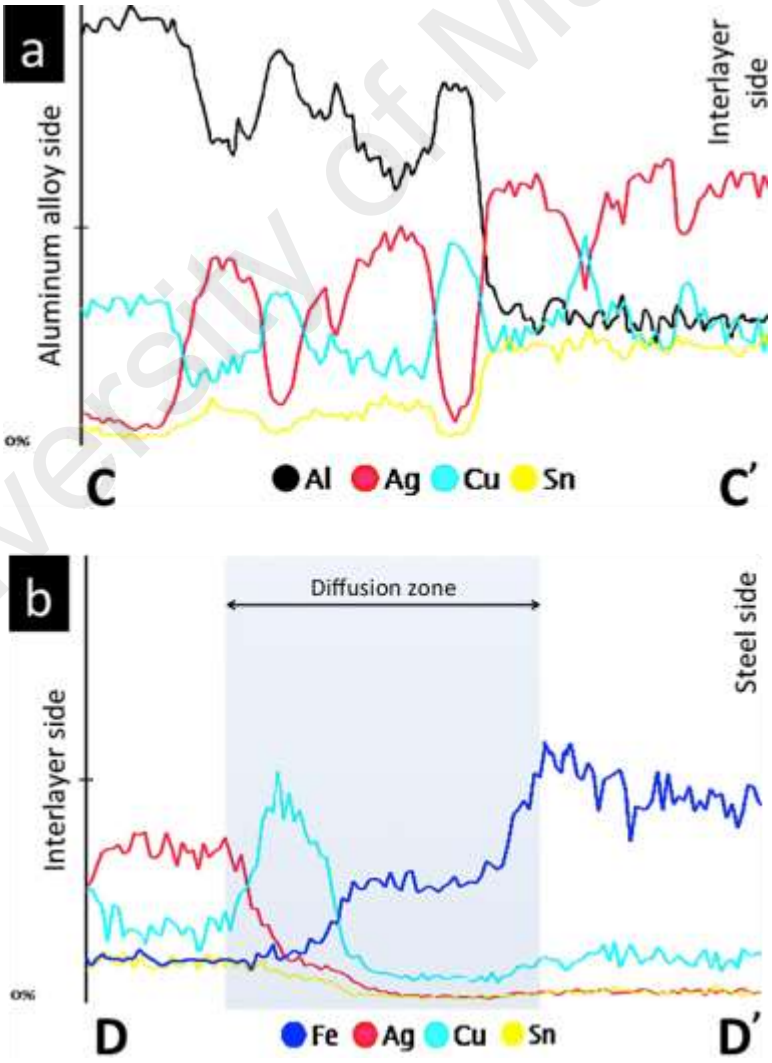

Figure 5.36: Elemental analysis of the ECAE joint's interlayer interface after annealing at 520 ºC: (a) Aluminum alloy-interlayer interface, (b) Steel-interlayer interface

As seen in Figure 5.37 and as further clarification for the EDX line scan analyses, the XRD results represent the abundance of intermetallics with Cu content. This is essentially an indication of considerable copper consumption at the interfaces. Amongst these intermetallics, Cu_6Sn_5 was detected at substantial intensity together with AlCu and these are known to function much like diffusion barriers (Ghosh et al., 2009; Li et al., 2012). Therefore, they can decrease the migration of other chemical species to the aluminum alloy and steel.

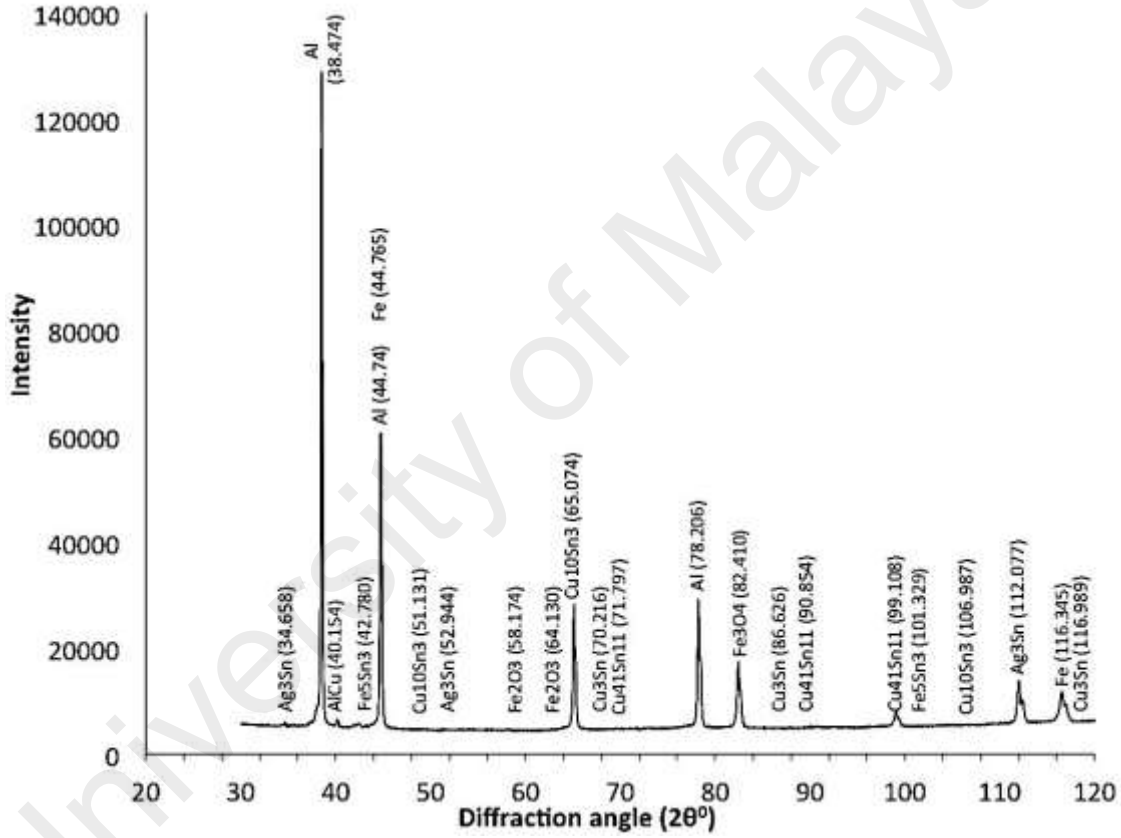

Figure 5.37: X-ray diffraction pattern obtained from the joint's interfaces in case of the workpiece with an interlayer after annealing at 520 ºC

5.4.5. Joint shear strength

The shear strengths of workpiece joints that did not undergo annealing as well as those subjected to annealing treatment at various temperatures after ECAE are presented in Figure 5.38.

It is clear from the shear test results that both post-ECAE heat treatment through annealing at various temperatures and interlayer application improved joint strength. Moreover, regardless of annealing temperature, the workpieces with an interlayer demonstrated higher shear strength values compared with those joined without an interlayer.

In general, the results do not suggest any significant enhancement in shear strength up to 320 °C annealing temperature for both joining setups. However, upon transition from 320 to 420 °C, considerable improvement of about 37% and 60% is observable for both joining setups, with and without an interlayer respectively. Based on these observations, it is implied that the energy barrier obstructing the initiation of interdiffusion between the mating materials can be overcome predominantly at temperatures ranging from 320 to 420 °C. Besides, with a further rise in annealing temperature up to 520 °C in the joining setup without an interlayer, and although the width of the intermetallics increased (Figure 5.32(b)), no embrittlement with detrimental consequences on shear strength were observed. Rather, the very thin interfacial intermetallic layer consolidated the coalescence of mating aluminum alloy and steel, which led to attaining a shear strength value of 27 MPa.

Correspondingly, in the case of workpieces with an interlayer, the results qualify the effective usage of an AgCuSn interlayer. Although the higher annealing temperatures may degrade the joint's strength owing to the formation of thicker interfacial reaction species, the increasing diffusion mass transfer at higher annealing temperatures resulted in a stronger atomic bond of up to 32 MPa at 520 °C compared with lower temperatures. Besides that, the less frequent formation of the defects such as micro-cracks and pores as well as the occurrence of mechanical interlocking mechanism at aluminum alloy-interlayer interfaces played major role in improving the bond strength of the joints in presence of interlayer. The existence of mechanical interlocking mechanism is fortified

by corrugated morphology observed at aluminum alloy-interlayer interfaces which inhibits the relative movement of components when subjected to shearing. Accordingly, the better integrity observed at the steel-interlayer interfaces which was confirmed by a smooth transition of the chemical elements upon scanning from steel to interlayer (shown by EDX line analysis in Figure 5.36), is the other cause for enhanced bond strength. The interlayer also restricted the formation of brittle Fe-Al intermetallics such as: $FeAl_3$ and Fe_4Al_{13} which was detected through XRD only in sample without interlayer (Figure 5.34). Therefore, usage of interlayer eliminated the possibility of Fe-Al intermetallics-related cracks nucleation and propagation which led to higher bond strength.

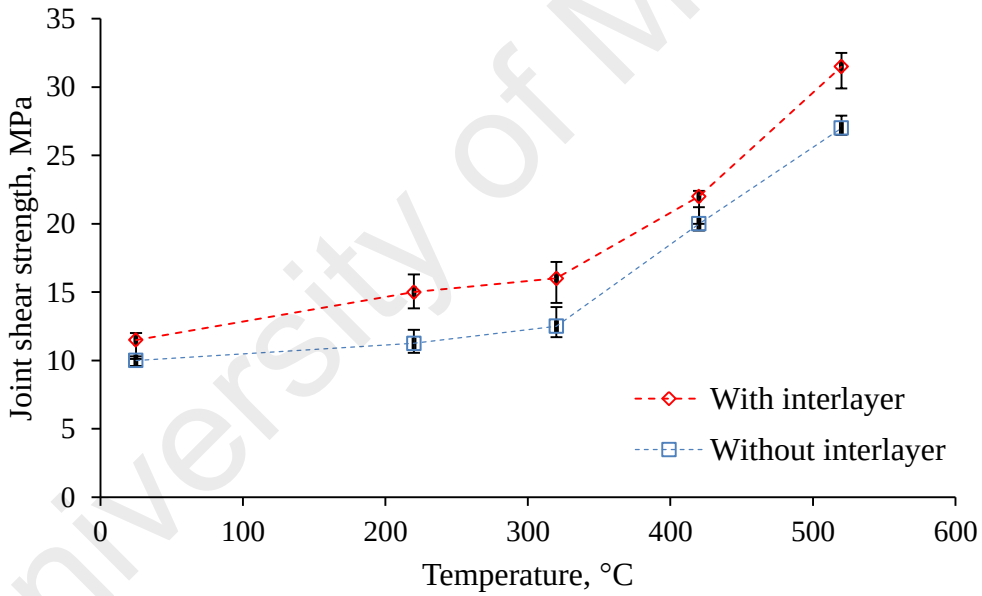

Figure 5.38: Tested workpiece shear strength dependence on temperature

5.4.6. Nano-indentation

In order to correlate the metallurgical analyses and microscopic observations to the mechanical properties, nanoindentation tests were performed across the joints' interfaces. The typical load-displacement (*p*-*h*) curves of the ECAE joints' interfaces annealed at 520 °C are shown in Figure 5.39. Evidently, none of the curves exhibit any significant discontinuity during loading or unloading in the form of pop-in or pop-out events. This essentially indicates the absence of abrupt plastic flow in the tested regions,

which confirms the lack of any phase transformation or crack formation (Fischer-Cripps, 2000) during the nanoindentation experiments.

From Figure 5.39, it is apparent that applying a constant 6000 μN normal load resulted in significantly higher displacement for the aluminum alloy sheath and steel core compared with the intermetallic layer. For this reason, the hardness values measured on aluminum alloy (1.03 GPa) and steel (2.58 GPa) are remarkably lower than the intermetallic layer (6.28 GPa). This observation verifies the results obtained earlier from the chemical and crystallographic analyses (Figure 5.33 and Figure 5.34) that demonstrate the existence of brittle Al-rich $FeAl_3$ and Fe_4Al_{13} intermetallics. Note that the value of intermetallic hardness in the current study exhibits promising conformity with the range suggested by other researchers (Frutos et al., 2013).

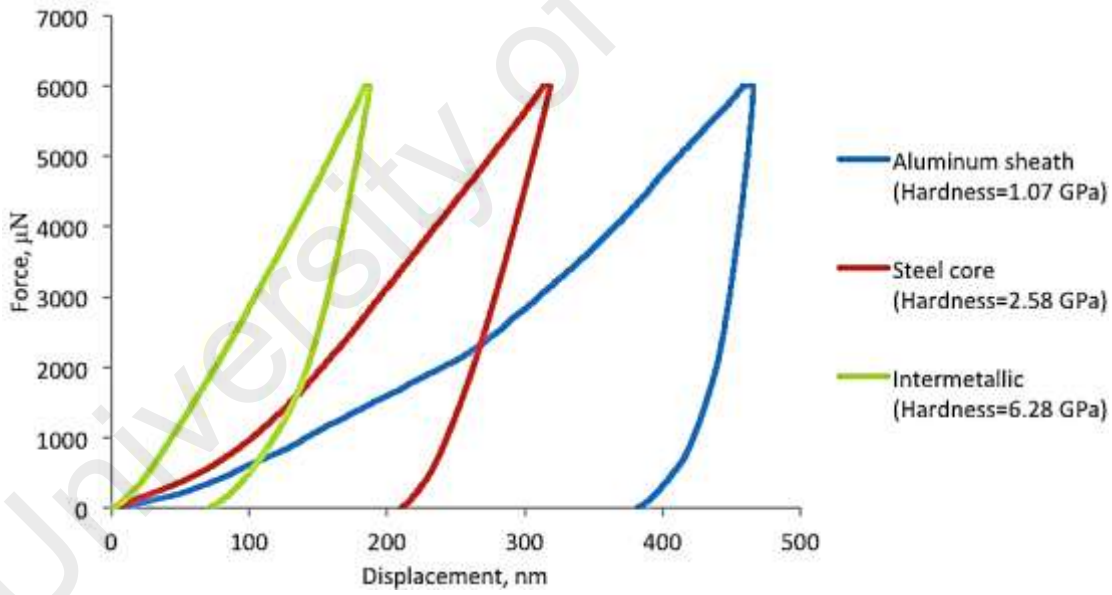

Figure 5.39: Load-displacement responses of various regions across the joint interface for the workpiece annealed at 520°C

Furthermore, according to Figure 5.40, the interlayer-aluminum alloy and interlayer-steel interfaces have hardness values of 3.82 and 2.6 GPa, respectively. However, these values are significantly lower compared with the Fe-Al intermetallic layer that formed in the case of a typical joining configuration without an interlayer. This smaller

difference in hardness values between base materials and interfaces may justify the higher shear strength outcomes achieved in the joints with an interlayer (Figure 5.38). The increase in hardness at the interlayer interfaces with the base materials can be primarily attributed to the effect of severe plastic deformation. Moreover, the intermetallic-induced hardness increase due to the formation of diffusion couples Al-Cu, Cu-Sn, Fe-Sn may be another reason for the higher interface hardness values in the joints with an interlayer.

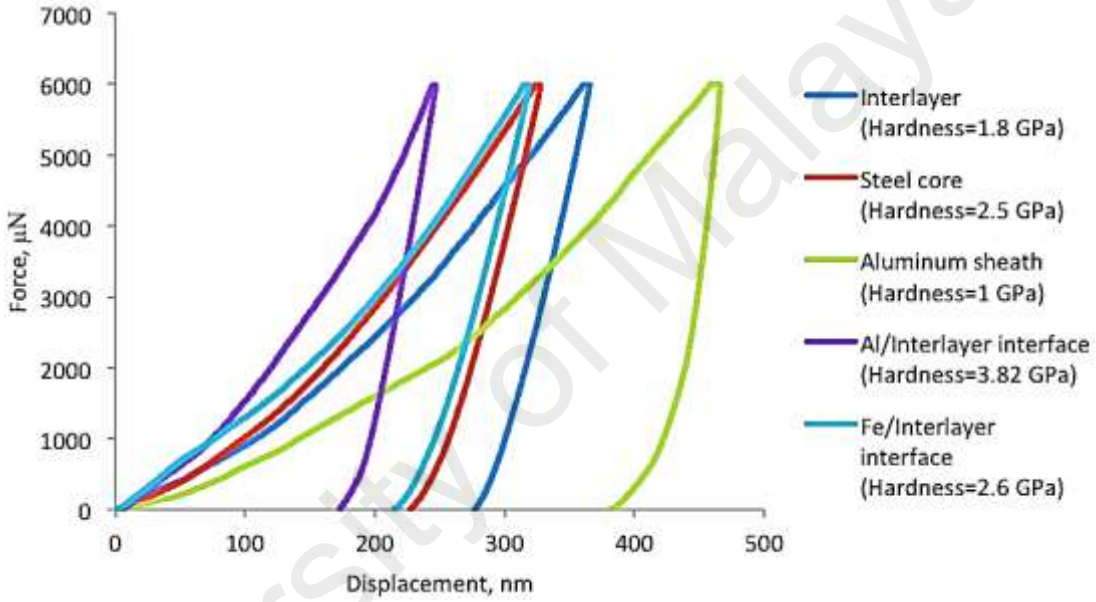

Figure 5.40: Load-displacement responses of various regions across the joint interfaces for the workpiece with interlayer annealed at 520°C

5.4.7. Fractographic analysis of fractured sections

The failure locations after the shear strength tests in addition to the typical (500×) and magnified (2500×) fractographs of fractured sections in workpieces with the highest shear strengths (32 MPa and 27 MPa with interlayer and without interlayer, respectively) are illustrated in Figure 5.41(a) and 5.41(b). In general, joint failure did not occur in the bulk of the base materials mainly due to the thick wall of AA 6061 sheath (2.5 mm) in addition to the significant shear strength of SAE 1018 bulk, which caused the failure to be localized at the joints' interfaces.

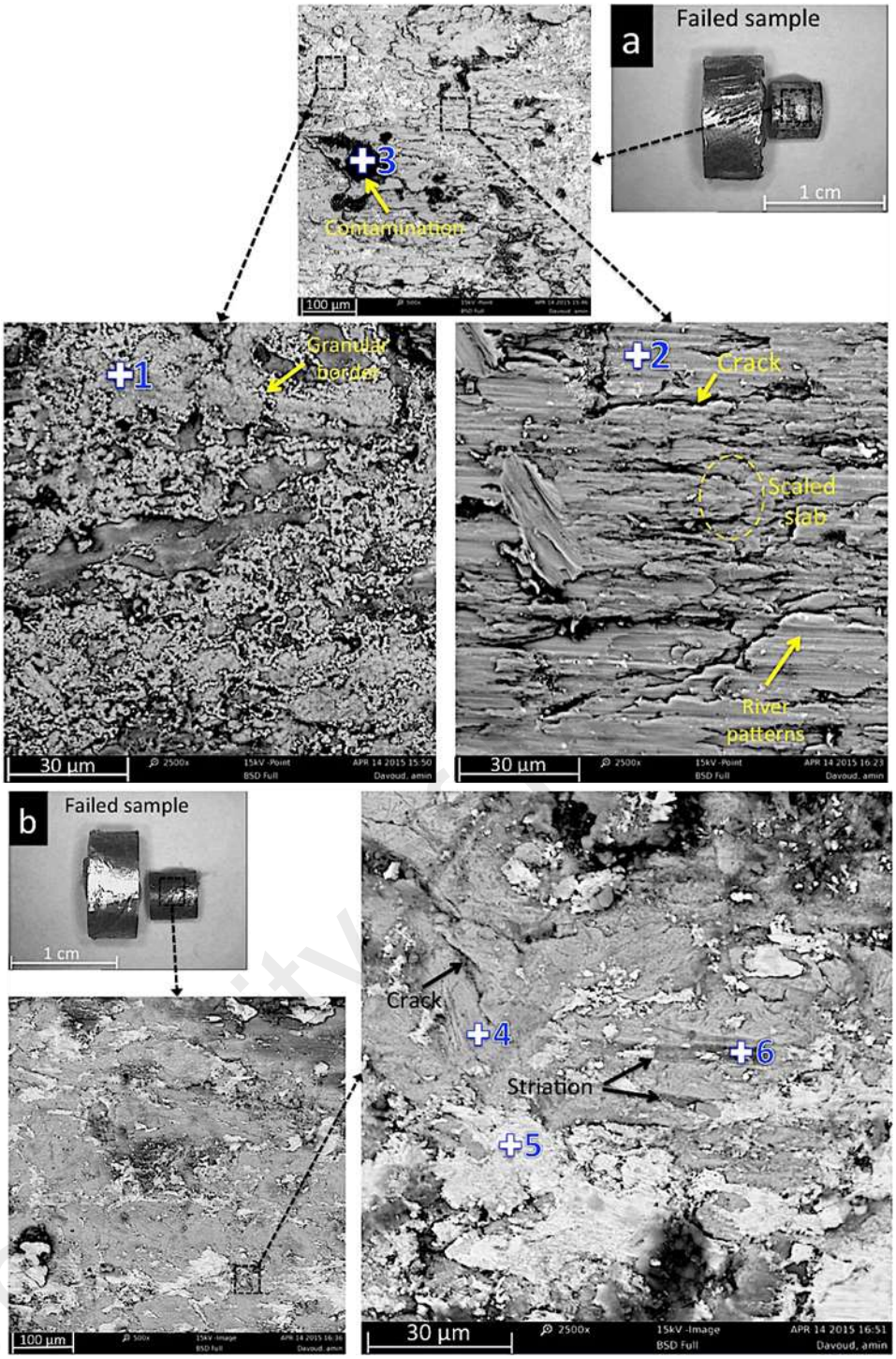

Figure 5.41: Fractographs of failed workpieces annealed at 520^0C for (a) joint without interlayer and (b) joint with interlayer

The fractograph of the workpiece without an interlayer shown in Figure 5.41(a) consists of three distinct zones: dispersed bright, grey and black zones. The bright areas (point 1) possess morphology similar to a group of islands, surrounded by jagged granular borders. According to the composition analysis (Figure 5.42), these areas rich in oxygen may be oxides of iron and aluminum. Besides, the grey region (point 2) exhibits a rather

different morphology, with scaled slabs aligned in a similar direction and traces of parallel river patterns aligned in the same direction as the force applied during shear testing. The elemental analysis shows the composition of Al (88.3%) and Fe (8.6%), suggesting the existence of brittle Al-rich intermetallics in this grey region. The black areas (point 3) dispersed across the fractured section are assumed to be contaminations. From the features observed in the bright and grey zones, it is evident that fracturing of the joint without an interlayer was driven mainly by brittleness.

Furthermore, the fractograph of the workpiece joined with an AgCuSn interlayer (Figure 5.41(b)) is characterized by cracks, sharp edges and striation. Nonetheless, these features are observed less frequently than the fractured section of the workpiece without an interlayer. These features reduce the possibility of brittle fracture as a major failure mode in the case of a workpiece with an interlayer. Figure 5.42 represents the EDX analysis disclosing the presence of 4 distinct areas in terms of composition, namely an area rich in iron (point 4), aluminum (point 5), interlayer components (point 6) and black zones identified as contaminated regions. This dispersion of elements in various proportions across the fractured section indicates that the fracture propagated through various mating material layers.

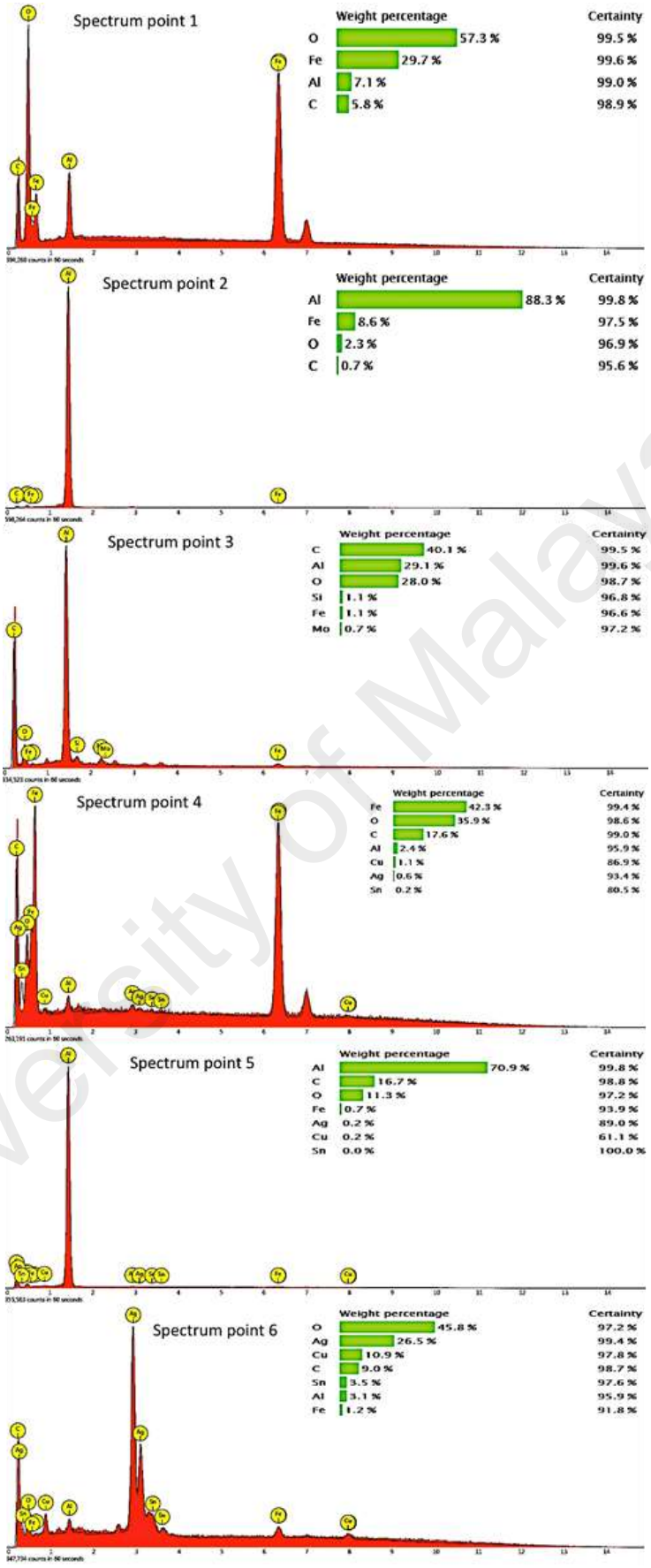

Figure 5.42: Elemental analysis of failed workpieces annealed at 520 ºC.

In order to precisely identify the phases responsible for joint failure, XRD analyses were carried out on the steel section of the failed joints and the results are shown in Figure 5.43. Conforming to the EDX analyses mentioned above (Figure 5.42), the failure section of the workpiece without an interlayer represents an Al-rich $FeAl_3$ intermetallic phase in addition to various types of Fe_xO_y oxide compounds (Figure 5.43(a)). Correspondingly, the XRD pattern of the fractured section of the workpiece with an AgCuSn interlayer (Figure 5.43(b)) demonstrates various diffusion couples of Al-Cu, Cu-Sn and Fe-Sn in addition to a Fe_3O_4 oxide compound.

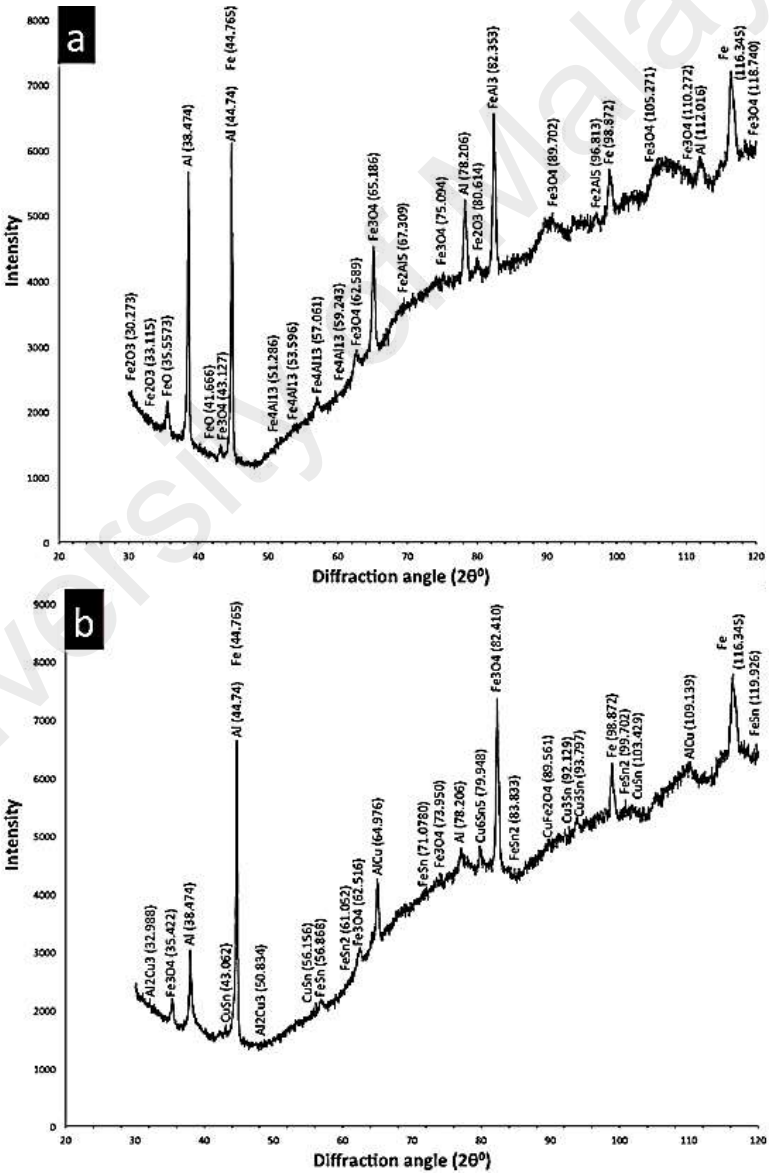

Figure 5.43: X-ray diffraction patterns of the failed joints in workpieces (a) without an interlayer and (b) with an interlayer

CHAPTER SIX: CONCLUSIONS AND SUGGESTIONS FOR FUTURE WORKS

6.1. Conclusions

In this work, the influence of different treatments including heat treatment and hard anodizing on the mechanical properties (surface hardness, tensile strength, fatigue and fretting fatigue) of AA 6063 was subjected to equal channel angular extrusion (ECAE) were studied. Furthermore, ECAE was developed in order to impose SPD on tubular AA 6061 as well as to join dissimilar metals including tubular AA 6061 and bar-shaped mild steel SAE 1018. The main findings of this research have been summarized as follow:

a) Mechanical properties of ECAE-treated AA 6063-O:

The FE-simulation results indicated that, the developed die set is capable of imposing equivalent plastic strain (EPS) of ~ 0.98 to workpiece; however, the distribution of EPS is not uniform over the workpiece cross section. Experimental results indicated that, the surface hardness of workpiece processed by HT, ECAE, ECAE+HT and ECAE+HT+HA were improved and reached values of 65, 85, 105 and 310 HV respectively, while the surface hardness of as-received one measured as 34 HV. Moreover, the ultimate strengths of workpieces processed by different techniques (HT, ECAE, ECAE+HT and ECAE+HT+HA) increased to values of 130, 171.1, 199.8 and 198 MPa respectively, while the ultimate strength of as-received workpiece was 72.7 MPa. Furthermore, the empirical fatigue and fretting fatigue test results indicated that the ECAE treatment had a positive effect on enhancing the workpieces' plain and fretting fatigue lives at high- and low-cyclic loads compared with the HT technique by 78 and 67 %, and 131 and 154 %, respectively. The results also signify that the ECAE+HT technique significantly increased the fatigue and fretting fatigue lives of the workpieces compared to the ECAE method at high and low cycles by 15.56% and

8.33%, and 14.4% and 5.1% respectively. Also, hard anodizing of AA 6063 remarkably increased the fatigue and fretting fatigue lives of ECAE+HT-processed workpieces at low cycle by 15.5% and 18.4% respectively; however, for high cycles hard anodizing produced opposite results and the fatigue and fretting fatigue lives of ECAE+HT-processed workpieces decreased by 16.7% and 30%, respectively.

b) ECAE treatment of tubular components:

The FEA outputs indicated that, designed die (channel angle (φ) of 120° and a corner angle (ψ) of 22°) set is capable of imposing EPS of ~ 0.63 to the workpiece. Also, plastic instability analysis demonstrated the validity of the proposed SPD process of tubes through ECAE since the triaxiality index never exceeded EPS and exhibited negative values as soon as shearing occurred. Experimental results indicated that, the yield shear stress, ultimate shear strength, and hardness of tubular AA 6061 increased significantly for the ECAE-treated tubes by factors of ~2.5, ~1.4, and ~2.1, respectively, compared with the as-received material due to a 60% reduction in the mean grain size. However, a decrease in ductility was observed for the ECAE-treated samples compared to the as-received workpiece. Moreover, heat treating (T6) performed after the ECAE process successfully recovered the ductility of the ECAE-treated workpieces. Moreover, the double treatment exhibited a notably positive influence on the mechanical properties including the yield shear stress and yield ultimate strength.

c) Dissimilar joining of tubular AA 6061 and bar-shaped Mild steel SAE 1018:

The FE-simulation results showed significant accumulation of EPS in all joined components with the maximum amount imposed on the AgCuSn interlayer as a result of one-pass pressing. Accordingly, the strain inhomogeneity index (C_i) indicated maximum microstructural uniformity in case of an interlayer followed by aluminum alloy. The visual investigation of joints' interfaces in workpieces without an interlayer annealed at 520 °C demonstrated the formation of a thin intermetallic compound layer.

Elemental and crystallographic analyses confirmed this layer contained Al-rich $FeAl_3$ and Fe_4Al_{13} phases. The existence of such layer between aluminum alloy and steel was further confirmed by nanoindentation experiments. Although there was no evidence of interfacial discontinuity or defects at this interface, this layer appeared to be a potential site for crack nucleation and propagation upon being subjected to stress. Compared with the joining configuration with no interlayer, the workpiece interfaces with an interlayer annealed at 520 °C did not reveal any distinguishable interfacial reaction layer. However, the interlayer interfaces with base materials displayed a corrugated morphology with dominant migration of interlayer species on the aluminum alloy side in addition to a wavy line interface with the steel side. The chemical analysis proved the formation of various reaction phases, including diffusion couples of Al-Cu, Cu-Sn and Fe-Sn. Furthermore, the shear test results validated the capability of the ECAE process to join aluminum alloy and steel and produce joints with 10 MPa shear strength. Further improvements in shear strength were observed as a result of annealing both joining configurations, which reached 27 MPa and 32 MPa at 520 °C annealing temperature for workpieces without and with an interlayer, respectively. Moreover, the chemical analyses of the fracture profiles indicate the detrimental effect of Fe-Al intermetallics in the absence of an interlayer.

6.2. Suggestions for future work

Different aspects of the current work have the potential to be continued, modified, and/or more investigated in the future work. The current method of fatigue and fretting fatigue evaluation of ECAE treated AA 6063 can be extended for further pressing passes, different method of post-ECAE coating process and different post-heat treatment procedures. Furthermore influence of strain inhomogeneity depend on different pressing route may use to evaluate fatigue endurance. Regarding the SPD processing of tubular components this process can be further generalized by considering

the influence of back pressure, subsequent pressing passes and different tube thickness. In addition, this method can be developed for plastic joining of tubular components. Further investigations can be conducted to extend the plastic joining process for various combinations of various materials by implementing different types of interlayers. Moreover the influence of back pressure, subsequent pressing passes and heat treatment may use as the effective factors to improve the joint quality.

REFERENCES

Abaqus 6.11 user documentation. (2011). Dassault systèmes simulia corp.

Alkorta, J., & Sevillano, J. G. (2003). A comparison of FEM and upper-bound type analysis of equal-channel angular pressing (ECAP). *Journal of Materials Processing Technology*, 141(3), 313-318.

Almaraz, G. M. D., Ambriz, J. L. Á., & Calderón, E. C. (2012). Fatigue endurance and crack propagation under rotating bending fatigue tests on aluminum alloy AISI 6063-T5 with controlled corrosion attack. *Engineering Fracture Mechanics*, 93, 119–131.

Altan, B. (2006). *Severe plastic deformation: toward bulk production of nanostructured materials*: Nova Publishers.

Ardell, A. J. (1985). Precipitation hardening. *Metallurgical Transactions A*, 16(12), 2131-2165.

Arsene, S., & Bai, J. (1998). A new approach to measuring transverse properties of structural tubing by a ring test : Experimental investigation. *Journal of Testing and Evaluation*, 26, 26-30.

ASM. (2010). *Fatigue Failures*: ASM International.

Azushima, A., & Aoki, K. (2002). Properties of ultrafine-grained steel by repeated shear deformation of side extrusion process. *Materials Science and Engineering: A*, 337(1), 45-49.

Azushima, A., Kopp, R., Korhonen, A., Yang, D., Micari, F., Lahoti, G., Groche, P., Yanagimoto, J., Tsuji, N., & Rosochowski, A. (2008). Severe plastic deformation (SPD) processes for metals. *CIRP Annals-Manufacturing Technology*, 57(2), 716-735.

Babaei, A., & Mashhadi, M. M. (2014). Tubular pure copper grain refining by tube cyclic extrusion–compression (TCEC) as a severe plastic deformation technique. *Progress in Natural Science: Materials International*, 24(6), 623-630.

Babaei, A., Mashhadi, M. M., & Jafarzadeh, H. (2014). Tube cyclic expansion-extrusion (TCEE) as a novel severe plastic deformation method for cylindrical tubes. *Journal of Materials Science*, 49(8), 3158-3165.

Balasundar, I., & Raghu, T. (2010). Effect of friction model in numerical analysis of equal channel angular pressing process. *Materials & Design*, 31(1), 449-457.

Banabic, D. (2000). *Formability of metallic materials: plastic anisotropy, formability testing, forming limits*: Springer Science & Business Media.

Bao, Y., & Wierzbicki, T. (2004). On fracture locus in the equivalent strain and stress triaxiality space. *International Journal of Mechanical Sciences*, 46(1), 81-98.

Basavaraj, V. P., Chakkingal, U., & Kumar, T. S. P. (2009). Study of channel angle influence on material flow and strain inhomogeneity in equal channel angular pressing using 3D finite element simulation. *journal of materials processing technology*, 209, 89–95.

Benjamin, J. S. (1970). Dispersion strengthened superalloys by mechanical alloying. *Metallurgical transactions*, 1(10), 2943-2951.

Berbon, P. B., Furukawa, M., Horita, Z., Nemoto, M., & Langdon, T. G. (1999). Influence of pressing speed on microstructural development in equal-channel angular pressing. *Metallurgical and Materials Transactions A*, 30(8), 1989-1997.

Bhanumurthy, K., Fotedar, R. K., Joyson, D., Kale, G. B., Pappachan, A. L., Grover, A. K., & Krishnan, J. (2006). Development of tubular transition joints of aluminium/stainless steel by deformation diffusion bonding. *Materials Science and Technology*, 22(3), 321-330.

Bishop, J., & Hill, R. (1951). XLVI. A theory of the plastic distortion of a polycrystalline aggregate under combined stresses. *The London, Edinburgh, and Dublin Philosophical Magazine and Journal of Science*, 42(327), 414-427.

Blanchard, P., Colombie, C., Pellerin, V., Fayeulle, S., & Vincent, L. (1991). Material effects in fretting wear: application to iron, titanium, and aluminum alloys. *Metallurgical and Materials Transactions A*, 22(7), 1535-1544.

Bouchama, L., Azzouz, N., Boukmouche, N., Chopart, J. P., Daltin, A. L., & Bouznit, Y. (2013). Enhancing aluminum corrosion resistance by two-step anodizing process. *Surface and Coatings Technology*, 235, 676–684.

Bowen, J. R., Gholinia, A., Roberts, S. M., & Prangnell, P. B. (2000). Analysis of the billet deformation behaviour in equal channel angular extrusion. *Materials Science and Engineering: A*, 287(1), 87–99.

Casati, R., Bonollo, F., Dellasega, D., Fabrizi, A., Timelli, G., Tuissi, A., & Vedani, M. (2014). Ex situ Al–Al2O3 ultrafine grained nanocomposites produced via powder metallurgy. *Journal of Alloys and Compounds*, 615(1), S386–S388.

Cavaliere, P., & Cabibbo, M. (2008). Effect of Sc and Zr additions on the microstructure and fatigue properties of AA6106 produced by equal-channel-angular-pressing. *Materials characterization*, 59(3), 197-203.

Chakkingal, U., Suriadi, A. B., & Thomson, P. (1998). Microstructure development during equal channel angular drawing of Al at room temperature. *Scripta Materialia*, 39(6), 677-684.

Chandrupatla, T. R., Belegundu, A. D., Ramesh, T., & Ray, C. (1997). *Introduction to finite elements in engineering*: Prentice Hall Upper Saddle River.

Chen, C., & Kobayashi, S. (1978). Rigid plastic finite element analysis of ring compression. *Applications of Numerical Methods to Forming Processes*, 163-174.

Chen, S., Ke, F., Zhou, M., & Bai, Y. (2007). Atomistic investigation of the effects of temperature and surface roughness on diffusion bonding between Cu and Al. *Acta Materialia*, 55(9).

Chung, C., Kim, J., Kim, H., & Kim, W. (2002). Improvement of high-cycle fatigue life in a 6061 Al alloy produced by equal channel angular pressing. *Materials Science and Engineering: A*, 337(1), 39-44.

Csontos, A. A., & Starke, E. A. (2005). The effect of inhomogeneous plastic deformation on the ductility and fracture behavior of age hardenable aluminum alloys. *International Journal of Plasticity*, 21(6), 1097-1118.

Daniel, I. M., Ishai, O., Daniel, I. M., & Daniel, I. (1994). *Engineering mechanics of composite materials* (Vol. 3): Oxford university press New York.

Dharmendra, C., Rao, K. P., Wilden, J., & Reich, S. (2011). Study on laser welding–brazing of zinc coated steel to aluminum alloy with a zinc based filler. *Materials Science and Engineering: A*, 528(3), 1497–1503.

Dieter, G. E., & Bacon, D. (1986). *Mechanical metallurgy* (Vol. 3): McGraw-Hill New York.

Djavanroodi, F., Zolfaghari, A., Ebrahimi, M., & Nikbin, K. (2013). Equal channel angular pressing of tubular samples. *Acta Metallurgica Sinica (English Letters)*, 26(5), 574-580.

Dumoulin, S., Roven, H., Werenskiold, J., & Valberg, H. (2005). Finite element modeling of equal channel angular pressing: Effect of material properties, friction and die geometry. *Materials Science and Engineering: A*, 410, 248-251.

Dunstan, D. J., & Bushby, A. J. (2014). Grain size dependence of the strength of metals: The Hall–Petch effect does not scale as the inverse square root of grain size. *International Journal of Plasticity*, 53, 56–65.

E8/E8M–11. (2011). Standard test methods for tensile testing of metallic materials. *ASTM International, West Conshohocken, PA*.

E143-13. (2013). Standard test method for shear modulus at room temperature. *ASTM International, West Conshohocken, PA*.

E384-11e1. (2011). Standard Test Method for Knoop and Vickers Hardness of Materials. *ASTM International, West Conshohocken, PA*.

Eivani, A. R., & Taheri, A. K. (2007). A new method for producing bimetallic rods. *Materials Letters*, 61(19-20), 4110–4113.

Estrin, Y., & Vinogradov, A. (2010). Fatigue behaviour of light alloys with ultrafine grain structure produced by severe plastic deformation: An overview. *International Journal of Fatigue*, 32, 898-907.

Estrin, Y., & Vinogradov, A. (2013). Extreme grain refinement by severe plastic deformation: a wealth of challenging science. *Acta Materialia*, 61(3), 782-817.

Faraji, G., Mashhadi, M. M., & Kimb, H. S. (2011). Tubular channel angular pressing (TCAP) as a novel severe plastic deformation method for cylindrical tubes. *Materials Letters*, 65(19-20), 3009-3012.

Farkas, D., Van Swygenhoven, H., & Derlet, P. (2002). Intergranular fracture in nanocrystalline metals. *Physical Review B*, 66(6), 060101.

Farshidi, M. H., Kazeminezhad, M., & Miyamotob, H. (2014). Microstructrual evolution of aluminum 6061 alloy through tube channel pressing. *Materials Science and Engineering: A*, 615, 139-147.

Fischer-Cripps, A. C. (2000). *Factors Affecting Nanoindentation Test Data*: Springer New York.

Frutos, E., Morris, D. G., & Muñoz-Morris, M. A. (2013). Evaluation of elastic modulus and hardness of Fe-Al base intermetallics by nano-indentation techniques. *Intermetallics*, (38), 1-3.

Ghosh, M., Kar, A., Das, S. K., & Ray, A. K. (2009). Aging Characteristics of Sn-Ag Eutectic Solder Alloy with the Addition of Cu, In, and Mn. *Metallurgical and Materials Transactions A*, 40(10), 2369-2376.

Gleiter, H. (1989). Nanocrystalline materials. *Progress in Materials Science*, 33(4), 223–315.

Han, E., Liu, X., & Chen, R. (2010). Preparation method of laminated composite materials of different alloys: Google Patents.

Hancock, J. W., & Mackenzie, A. C. (1976). On the mechanisms of ductile failure in high-strength steels subjected to multi-axial stress-states. *Journal of the Mechanics and Physics of Solids*, 24(2), 147-160.

Hause, S. C., & Maltby, W. S. (1998). *Western civilization: a history of European society* (Vol. 3): Wadsworth Publishing Company.

Heinz, A., Haszler, A., Keidel, C., Moldenhauer, S., Benedictus, R., & Miller, W. S. (2000). Recent development in aluminium alloys for aerospace applications. *Materials Science and Engineering: A*, 280(1), 102-107.

Heredia, S., Fouvry, S., Berthel, B., & Greco, E. (2014). Introduction of a ‘‘principal stress–weight function’’ approach to predict the crack nucleation risk under fretting fatigue using FEM modelling. *International Journal of Fatigue*, 61, 191-201.

Hirsch, J., & Al-Samman, T. (2013). Superior light metals by texture engineering: optimized aluminum and magnesium alloys for automotive applications. *Acta Materialia*, 61(3), 818-843.

Höppel, H., Kautz, M., Xu, C., Murashkin, M., Langdon, T., Valiev, R., & Mughrabi, H. (2006). An overview: fatigue behaviour of ultrafine-grained metals and alloys. *International Journal of Fatigue*, 28(9), 1001-1010.

Horita, Z., & Langdon, T. G. (2005). Microstructures and microhardness of an aluminum alloy and pure copper after processing by high-pressure torsion. *Material science and engineering A*, 410–411, 422–425.

Jafarlou, D., Hassan, M., Mardi, N. A., & Zalnezhad, E. (2014). Influence of temper rolling on tensile property of low carbon steel sheets by application of Hill 48 anisotropic yield criterion. *Procedia Engineering*, 81, 1222 – 1227

Joun, M. S., Moon, H. G., Choi, I. S., Lee, M. C., & Jun, B. Y. (2009). Effects of friction laws on metal forming processes. *Tribology International*, 42(2), 311-319.

Kim, H. S. (2001). Prediction of Temperature Rise in Equal Channel Angular Pressing. *Materials Transactions*, 42(3), 536-538.

Kim, H. S., Hong, S. I., & Seo, M. H. (2001). Effects of strain hardenability and strain-rate sensitivity on the plastic flow and deformation homogeneity during equal channel angular pressing. *Journal of Materials Research*, 16(03), 856-864.

Kim, H. S., Seo, M. H., & Hong, S. I. (2000). On the die corner gap formation in equal channel angular pressing. *Materials Science and Engineering: A*, 291(1), 86-90.

Kitamura, K., Hirota, K., Ukai, Y., Matsunaga, K., & Osakada, K. (2012). Cold joining of rotor shaft with flange by using plastic deformation. *CIRP Annals-Manufacturing Technology*, 61, 275–278.

Kobayashi, S., Oh, S.-I., & Altan, T. (1989). *Metal Forming and the Finite-Element Method*: Oxford University Press.

Langdon, T. G., Furukawa, M., Nemoto, M., & Horita, Z. (2000). Using equal-channel angular pressing for refining grain size. *JOM*, 52(4), 30-33.

Lapovok, R., Estrin, Y., Popov, M. V., & Langdon, T. G. (2008). Enhanced Superplasticity in a Magnesium Alloy Processed by Equal Channel Angular Pressing with a Back Pressure. *Advanced Engineering Materials*, 10(5), 429-433.

Lapovok, R., Thomson, P., Cottam, R., & Estrin, Y. (2005). Processing routes leading to superplastic behaviour of magnesium alloy ZK60. *Materials Science and Engineering: A*, 410, 390-393.

Lee, J. C., Seok, H. K., Han, J.-H., & Chung, Y.-H. (2001). Controlling the textures of the metal strips via the continuous confined strip shearing(C2S2) process. *Materials Research Bulletin*, 36(5-6), 997–1004.

Lee, J. E., Bae, D. H., Chung, W. S., Kim, K. H., Lee, J. H., & Cho, Y. R. (2007). Effects of annealing on the mechanical and interface properties of stainless steel/aluminum/copper clad-metal sheets. *Journal of Materials Processing Technology*, 187-188(546–549).

Lee, S., Berbon, P. B., Furukawa, M., Horita, Z., Nemoto, M., Tsenev, N. K., Valiev, R. Z., & Langdon, T. G. (1999). Developing superplastic properties in an aluminum alloy through severe plastic deformation. *Materials Science and Engineering: A*, 272(1), 63–72.

Li, J. F., Agyakwa, P. A., & Johnson, C. M. (2012). Effect of trace Al on growth rates of intermetallic compound layers between Sn-based solders and Cu substrate. *Journal of Alloys and Compounds*, 545, 70–79.

Li, S., Bourke, M., Beyerlein, I., Alexander, D., & Clausen, B. (2004). Finite element analysis of the plastic deformation zone and working load in equal channel angular extrusion. *Materials Science and Engineering: A*, 382(1), 217-236.

Lima, M. S. F. d., & Sankaré, S. (2014). Microstructure and mechanical behavior of laser additive manufactured AISI 316 stainless steel stringers. *Materials & Design*, 55, 526–532.

Liu, X., Chen, R., & Han, E. (2009). Preliminary investigations on the Mg–Al–Zn/Al laminated composite fabricated by equal channel angular extrusion. *Journal of Materials Processing Technology*, 209(10), 4675-4681.

Luo, P., McDonald, D. T., Xu, W., Palanisamy, S., Dargusch, M. S., & Xia, K. (2012). A modified Hall–Petch relationship in ultrafine-grained titanium recycled from chips by equal channel angular pressing. *Scripta Materialia*, 66(10), 785–788.

Malow, T. R., & Koch, C. C. (1998). Mechanical properties, ductility, and grain size of nanocrystalline iron produced by mechanical attrition. *Metallurgical and Materials Transactions A*, 29(9), 2285-2295.

Matsumoto, R., Hanami, S., Ogura, A., Yoshimura, H., & Osakada, K. (2008). New plastic joining method using indentation of cold bar to hot forged part. *CIRP Annals - Manufacturing Technology*, 57(1), 279-282.

May, J., Dinkel, M., Amberger, D., Höppel, H., & Göken, M. (2007). Mechanical properties, dislocation density and grain structure of ultrafine-grained aluminum and aluminum-magnesium alloys. *Metallurgical and Materials Transactions A*, 38(9), 1941-1945.

Mehrer, H. (2007). *Diffusion in Solids: Fundamentals, Methods, Materials, Diffusion-Controlled Processes*: Springer Science & Business Media.

Miller, W. S., Zhuang, L., Bottema, J., Wittebrood, A. J., Smet, P. D., Haszler, A., & Vieregge, A. (2000). Recent development in aluminium alloys for the automotive industry. *Materials Science and Engineering: A*, 280, 37-49.

Mohebbi, M. S., & Akbarzadeh, A. (2010). Accumulative spin-bonding (ASB) as a novel SPD process for fabrication of nanostructured tubes. *Materials Science and Engineering: A*, 528(1), 180-188.

Mori, K.-i., Bay, N., Fratini, L., Micari, F., & Tekkaya, A. E. (2013). Joining by plastic deformation. *CIRP Annals - Manufacturing Technology*, 62, 673-694.

Mott, N. F., & Nabarro, F. R. N. (1940). An attempt to estimate the degree of precipitation hardening, with a simple model. *Proceedings of the Physical Society*, 52(1), 86.

Nagasekhar, A. V., Chakkingal, U., & Venugopal, P. (2006). Candidature of equal channel angular pressing for processing of tubular commercial purity-titanium. *Journal of Materials Processing Technology*, 173, 53-60.

Nagasekhar, A. V., & Tick-Hon, Y. (2004). Optimal tool angles for equal channel angular extrusion of strain hardening materials by finite element analysis. *Computational Materials Science*, 30, 489-495.

Nelson, D. V. (1977). Review of fatigue-crack-growth prediction methods. *Experimental Mechanics*, 17(2), 41-49.

Neu, R. (2011). Progress in standardization of fretting fatigue terminology and testing. *Tribology International*, 44(11), 1371-1377.

Oosterkamp, A., Oosterkamp, L. D., & Nordeide, A. (2004). Kissing bond'phenomena in solid-state welds of aluminum alloys. *Welding Journal-New York* 83(8), 225-S.

Ozturk, F., Sisman, A., Toros, S., Kilic, S., & Picu, R. C. (2010). Influence of aging treatment on mechanical properties of 6061 aluminum alloy. *Materials & Design*, 31(2), 972–975.

Patlan, V., Vinogradov, A., Higashi, K., & Kitagawa, K. (2001). Overview of fatigue properties of fine grain 5056 Al-Mg alloy processed by equal-channel angular pressing. *Material science and engineering A*, 300, 171-182.

Pearson, W. B. (2013). *A Handbook of Lattice Spacings and Structures of Metals and Alloys: International Series of Monographs on Metal Physics and Physical Metallurgy* (Vol. 4): Elsevier.

Pei, Q. X., Hu, B. H., Lu, C., & Wang, Y. Y. (2003). A finite element study of the temperature rise during equal channel angular pressing. *Scripta Materialia*, 49(4), 303-308.

Pouraliakbar, H., Firooz, S., Jandaghi, M. R., Khalaj, G., & Amirafshar, A. (2014). Combined effect of heat treatment and rolling on pre-strained and SPDed aluminum sheet. *Materials Science and Engineering: A*, 612, 371-379.

Prangnell, P., Harris, C., & Roberts, S. (1997). Finite element modelling of equal channel angular extrusion. *Scripta Materialia*, 37(7), 983-989.

Rajasekaran, B., Raman, S. G. S., Joshi, S. V., & Sundararajan, G. (2008). Influence of detonation gun sprayed alumina coating on AA 6063 samples under cyclic loading with and without fretting. *Tribology International*, 41, 315–322.

Rao, S. S. (2004). *The Finite Element Method in Engineering* (Fourth Edition ed.): Elsevier Science & Technology Books.

Riedel, H. (2014). *Fracture at high temperatures*: Springer.

Rosochowski, A., & Olejnik, L. (2002). Numerical and physical modelling of plastic deformation in 2-turn equal channel angular extrusion. *Journal of Materials Processing Technology*, 125, 309-316.

Roven, H. J., Nesboe, H., Werenskiold, J. C., & Seibert, T. (2005). Mechanical properties of aluminium alloys processed by SPD: Comparison of different alloy systems and possible product areas. *Materials Science and Engineering: A*, 410, 426-429.

Sabetghadam, H., Hanzaki, A. Z., & Araee, A. (2010). Diffusion bonding of 410 stainless steel to copper using a nickel interlayer. *Materials Characterization*, 61(6), 626–634.

Saito, Y., Utsunomiya, H., Suzuki, H., & Sakai, T. (2000). Improvement in the r-value of aluminum strip by a continuous shear deformation process. *Scripta Materialia*, 42(12), 1139-1144.

Saito, Y., Utsunomiya, H., Tsuji, N., & Sakai, T. (1999). Novel ultra-high straining process for bulk materials development of the accumulative roll-bonding (ARB) process. *Acta Materialia*, 47(2), 579-583.

Schmidt, H., & Winterstetter, T. A. (2004). Cylindrical shells under torsional and transverse shear. *Buckling of thin metal shells*, 207.

Segal, V. M. (1999). Equal channel angular extrusion: from macromechanics to structure formation. *Materials Science and Engineering A*, 271(1-2), 322-333.

Sevillano, J. G., Van Houtte, P., & Aernoudt, E. (1980). Large strain work hardening and textures. *Progress in Materials Science*, 25(2), 69-134.

Skrotzki, W., Scheerbaum, N., Oertel, C.-G., Brokmeier, H.-G., Suwas, S., & Toth, L. (2007). Recrystallization of high-purity aluminium during equal channel angular pressing. *Acta Materialia*, 55(7), 2211-2218.

Smallman, R. E. (2013). *Modern physical metallurgy*: Elsevier.

Stanzl-Tschegg, S. (2014). Very high cycle fatigue measuring techniques. *International Journal of Fatigue*, 60, 2-17.

Suo, T., Li, Y., Guo, Y., & Liu, Y. (2006). The simulation of deformation distribution during ECAP using 3D finite element method. *Materials Science and Engineering: A*, 432(1), 269-274.

Suzuki, T., Takeuchi, S., & Yoshinaga, H. (2013). *Dislocation dynamics and plasticity* (Vol. 12): Springer Science & Business Media.

Szolwinski, M. P., & Farris, T. N. (1996). Mechanics of fretting fatigue crack formation. *Wear*, 198(1-2), 93-107.

Taban, E., Gould, J., & Lippold, J. (2010). Dissimilar friction welding of 6061-T6 aluminum and AISI 1018 steel: Properties and microstructural characterization. *Materials & Design*, 31(5), 2305–2311.

Taylor, G. I. (1934). The mechanism of plastic deformation of crystals. Part I. Theoretical. *Proceedings of the Royal Society of London. Series A, Containing Papers of a Mathematical and Physical Character*, 362-387.

Tellkamp, V. L., Lavernia, E. J., & Melmed, A. (2001). Mechanical behavior and microstructure of a thermally stable bulk nanostructured Al alloy. *Metallurgical and Materials Transactions A*, 32(9), 2335-2343.

Tong, X., Zhang, H., & Li, D. Y. (2015). Effect of Annealing Treatment on Mechanical Properties of Nanocrystalline α-iron: an Atomistic Study. *Sci. Rep.*, 5.

Tóth, L. S., Arzaghi, M., Fundenberger, J. J., Beausir, B., Bouaziz, O., & Arruffat-Massion, R. (2009). Severe plastic deformation of metals by high-pressure tube twisting. *Scripta Materialia*, 60(3), 175–177.

Totten, Westbrook, G. E., Shah, S. R., & J., R. (2003). *Fuels and Lubricants Handbook - Technology, Properties, Performance, and Testing: (MNL 37WCD)*: ASTM International.

Tsuji, N., Saito, Y., Lee, S.-H., & Minamino, Y. (2003). ARB (Accumulative Roll-Bonding) and other new Techniques to Produce Bulk Ultrafine Grained Material. *Advanced Engineering Materials* 5(5), 338–344.

Valiev, R. (2004). Nanostructuring of metals by severe plastic deformation for advanced properties. *Nature Materials*, 3(8), 511-516.

Valiev, R., Estrin, Y., Horita, Z., Langdon, T., Zehetbauer, M., & Zhu, Y. (2015). Fundamentals of superior properties in bulk nanoSPD materials. *Materials Research Letters*, (ahead-of-print), 1-21.

Valiev, R. Z., Alexandrov, I. V., Zhu, Y. T., & Lowe, T. C. (2002). Paradox of strength and ductility in metals processed by severe plastic deformation. *Journal of Materials Research*, 17(1), 5-8.

Valiev, R. Z., Estrin, Y., Horita, Z., Langdon, T. G., Zechetbauer, M. J., & Zhu, Y. T. (2006). Producing bulk ultrafine-grained materials by severe plastic deformation. *JOM*, 58(4), 33-39.

Valiev, R. Z., Islamgaliev, R. K., & Alexandrov, I. V. (2000). Bulk nanostructured materials from severe plastic deformation. *Progress in Materials Science*, 45, 103-189.

Valiev, R. Z., Krasilnikov, N. A., & Tsenev, N. K. (1991). Plastic deformation of alloys with submicron-grained structure. *Material science and engineering A*, 137, 35–40.

Valiev, R. Z., & Langdon, T. G. (2006). Principles of equal-channel angular pressing as a processing tool for grain refinement. *Progress in Materials Science*, 51(7), 881-981.

Valiev, R. Z., Zehetbauer, M. J., Estrin, Y., Höppel, H. W., Ivanisenko, Y., Hahn, H., Wilde, G., Roven, H. J., Sauvage, X., & Langdon, T. G. (2007). The Innovation Potential of Bulk Nanostructured Materials. *Advanced Engineering Materials*, 9, 527-533.

Vinogradov, A., Washikita, A., Kitagawa, K., & Kopylov, V. I. (2003). Fatigue life of fine-grain Al-Mg-Sc alloys produced by equal-channel angular pressing. *Materials Science and Engineering: A*, 349, 318-326.

Wagoner, R. H., & Chenot, J.-L. (1996). *Fundamentals of Metal Forming*. New York: John Wiley & Sons Inc.

Wang, K., Tao, N. R., Liu, G., Lu, J., & Lu, K. (2006). Plastic strain-induced grain refinement at the nanometer scale in copper. *Acta Materialia*, 54(19), 5281–5291.

Wang, Y., Chen, M., Zhou, F., & Ma, E. (2002). High tensile ductility in a nanostructured metal. *Nature*, 419(6910), 912-915.

Wei, K. X., Wei, W., Wang, F., Du, Q. B., Alexandrov, I. V., & Hu, J. (2011). Microstructure, mechanical properties and electrical conductivity of industrial Cu–0.5%Cr alloy processed by severe plastic deformation. *Materials Science and Engineering: A*, 528(3), 1478–1484.

Wei, W., Nagasekhar, A. V., Chen, G., Tick-Hon, Y., & Wei, K. X. (2006). Origin of inhomogenous behavior during equal channel angular pressing. *Scripta Materialia*, 54, 1865–1869.

Wiese, S., & Wolter, K. J. (2007). Creep of thermally aged SnAgCu-solder joints. *Microelectronics Reliability*, 47(2-3), 223–232.

Winterstetter, T. A., & Schmidt, H. (1999). Beulversuche an längsnahtgeschweißten stählernen KZS im elastisch-plastischen Bereich unter Axialdruck, Innendruck und Torsionsschub (pp. 82): Dept. of Civil Eng., University of Essen.

Wu, A., Song, Z., Nakata, K., Liao, J., & Zhou, L. (2015). Interface and properties of the friction stir welded joints of titanium alloy Ti6Al4V with aluminum alloy 6061. *Materials & Design*, 71, 85-92.

Xia, Q., Xiao, G., Long, H., Cheng, X., & Yang, B. (2014). A study of manufacturing tubes with nano/ultrafine grain structure by stagger spinning. *Materials & Design*, 59, 516-523.

Xu, C., Horita, Z., & Langdon, T. G. (2007). The evolution of homogeneity in processing by high-pressure torsion. *Acta Materialia*, 55(1), 203-212.

Yan, S., Hong, Z., Watanabe, T., & Jingguo, T. (2010). CW/PW dual-beam YAG laser welding of steel/aluminum alloy sheets. *Optics and Lasers in Engineering*, 48(7-8), 732–736.

Yang, D., Xiong, J., Hodgson, P., & Wen, C. e. (2009). Influence of deformation-induced heating on the bond strength of rolled metal multilayers. *Materials Letters*, 63, 2300-2302.

Yang, Y.-L., & Lee, S. (2003). Finite element analysis of strain conditions after equal channel angular extrusion. *Journal of Materials Processing Technology*, 140(1), 583-587.

Yapici, G. G., Karaman, I., Luo, Z. P., & Rack, H. (2003). Microstructure and mechanical properties of severely deformed powder processed Ti–6Al–4V using equal channel angular extrusion. *Scripta Materialia*, 49(10), 1021–1027.

Zalnezhad, E., & Sarhan, A. A. D. (2014). A fuzzy logic predictive model for better surface roughness of Ti–TiN coating on AL7075-T6 alloy for longer fretting fatigue life. *Measurement*, 49, 256–265.

Zalnezhad, E., Sarhan, A. A. D., & Hamdi, M. (2013). Investigating the fretting fatigue life of thin film titanium nitride coated aerospace Al7075-T6 alloy. *Materials Science and Engineering: A*, 559, 436–446.

Zander, D., Schnatterer, C., Altenbach, C., & Chaineux, V. (2015). Microstructural impact on intergranular corrosion and the mechanical properties of industrial drawn 6056 aluminum wires. *Materials & Design*, 83, 49-59.

Zhang, H. T., Feng, J. C., He, P., & Hackl, H. (2007). Interfacial microstructure and mechanical properties of aluminium–zinc-coated steel joints made by a modified metal inert gas welding–brazing process. *Materials Characterization*, 58(7), 588–592.

Zhang, Q., Jin, K., & Mu, D. (2014). Tube/tube joining technology by using rotary swaging forming method. *Journal of Materials Processing Technology* 214(10), 2085–2094.

Zhao, Y., Zhu, Y., Liao, X., Horita, Z., & Langdon, T. (2006). Tailoring stacking fault energy for high ductility and high strength in ultrafine grained Cu and its alloy. *Applied physics letters*, 89(12), 121906.

LIST OF PUBLICATIONS

Jafarlou, D.M. , Zalnezhad, E., Hamouda, A., Faraji, G., Mardi, N., & Hassan Mohamed, M. (2015). Evaluation of the Mechanical Properties of AA 6063 Processed by Severe Plastic Deformation. *Metallurgical and Materials Transactions A*, 1-13.

Jafarlou, D.M. , Zalnezhad, E., Ezazi, M., Mardi, N., & Hassan, M. (2015). The application of equal channel angular pressing to join dissimilar metals, aluminium alloy and steel, using an Ag–Cu–Sn interlayer. *Materials & Design*, 87, 553-566.

Jafarlou, D. M. , Zalnezhad, E., Hassan, M. A., Ezazi, M. A., Mardi, N. A., Hamouda, A. M. S., Hamdi, M., & Yoon, G. H. (2016). Severe plastic deformation of tubular AA 6061 via equal channel angular pressing. *Materials & Design*, 90, 1124-1135.